Characterizing the mechanical behavior of single and polycrystalline silicon carbide using nanoindentation.

A Dissertation Presented for the

Doctor of Philosophy

Degree

The University of Tennessee, Knoxville

Amit Datye

December 2014

DEDICATION

This work is dedicated to my family: grandparents, parents, and sister. I have received nothing but support from them my entire life. This would not be possible without the love and sacrifice of my parents.

ACKNOWLEDGEMENTS

A large number of people in my graduate school career have contributed and helped me achieve my goals.

G. M. Pharr: Thank you for giving me the opportunity to work under your guidance. I have learnt so much from you.

K. Johanns, E. G. Herbert and P. Sudharshan Phani: Thank you for helping me in my research and for the useful discussions.

H.T.Lin: Thank you for your support in my research and guidance in personal life.

I.Perez: I learnt so much from you working under your guidance for the ONR project.

Kuang-Hsi Wu: For always being there for me, with sound advice and insights.

Y. F. Gao, C. Mchargue and M. Madhukar for serving on my committee, teaching, and the helpful discussions on modeling and fracture mechanics.

The University of Tennessee faculty and staff, especially Carla Lawrence.

E. P. George, Shirley Waters and other staff at Oak Ridge National Laboratory.

Fellow graduate students at the University of Tennessee.

Financial support for this work was provided by the National Science Foundation under grant number CMMI 0926798.

ABSTRACT

This research aims at enhancing the fundamental understanding of mechanisms controlling the deformation and fracture of silicon carbide based ceramics (single- and poly-crystal). The role of microstructure and material properties on the energy absorption capability of SiC is studied. This research helps to improve the ability to quantitatively predict the initiation and propagation of fracture and the interaction between fracture and plasticity, which provides a step towards a mechanistic understanding of deformation and failure properties of ceramic single crystals and polycrystals. The validity of the indentation-cracking method for toughness measurement is examined using nanoindentation tests with different indenters (spherical, pyramidal). Pyramidal indenters with various centerline to face angles are used to produce a wide range of effective strains in the single and polycrystalline SiC. Crystal plasticity constitutive laws can be calibrated using below threshold indentation loads. Above threshold loads are used to construct a parametric map that delineates the dependence of the ratio of crack size and contact radius on indenter geometry, applied load, toughness, and hardness, thus providing important guidelines for the toughness measurement method. By examining the behavior of several SiC materials during nanoindentation experiments using spherical and pyramidal indenters, it is possible to make predictions about methods to improve the ductility and fracture toughness of SiC to optimize its energy absorption. The applicability of the area under the irreversible part of the indentation load displacement curve (energy dissipated during loading) to predict the performance of SiC under contact loading is examined.

TABLE OF CONTENTS

LIST OF TABLES

LIST OF FIGURES

LIST OF VARIABLES

Important Variables (in order of appearance)	***Symbol***
Hardness	H
Elastic Modulus	E
Fracture Toughness	K_{IC}
Poisson's Ratio	N
Displacement into surface	H
Stiffness	S
Applied Load on the Indenter	P
Reduced Modulus	E^*, E_r
Indenter Modulus	E_i
Indenter Poisson's Ratio	ν_i
Material Modulus	E_m
Material Poisson's Ratio	ν_m
Contact area	A_c
Contact depth	h_c
Radius of a sphere	R
Maximum displacement into surface	h_{max}
Maximum Applied load on the Indenter	P_{max}
Indenter shape factor	ε
Dimensionless parameter for non-axisymmetric indenters	β
Effective cone angle for a pyramid	α
Semi-angle for a pyramid (centerline to face angle)	θ
Shear modulus	G
Mean pressure	p_m
Theoretical shear stress	τ_{th}
Maximum shear stress (Tresca criterion)	τ_T
Maximum shear stress	τ_{max}
Cleavage strength (maximum tensile stress)	σ_{th}
Surface energy	γ
Modulus of fused Silica	E_{FS}
Holloman fit variable	K
Holloman fit variable (work hardening exponent)	n
Yield Strength	Y

CHAPTER 1. Introduction

1.1 Silicon carbide

The possibility of bonding silicon to carbon was suggested in 1824 by Jöns Jakob Berzelius. The compound silicon carbide (SiC) got more attention in 1890's when Eugene G. Acheson established a commercial process for the abrasives industry. Henri Moissan in 1905 established the existence of Silicon carbide in nature by analyzing the Diablo Canyon iron meteorite. Since then, SiC has been extensively researched due to its unique physical and chemical properties. SiC is the only compound of silicon (Si) and carbon (C) which exists in nature in the solid state at room temperature and pressure. SiC crystallizes in over 200 polytypes [1, 2] with different Si-C stacking sequences. Figure 1 below shows the stacking sequences of the most common SiC polytypes [3]. The most common polytypes are the 3C (Cubic) or β and 6H (Hexagonal) or α Silicon carbide [4]. Most polytypes have similar mechanical and thermal properties but different electrical and optical properties. Several researchers [5-9] have used Brillouin scattering experiments to find the single crystal elastic constants of SiC-6H (C_{11} = 501 ± 4 GPa, C_{33} = 553 ± 4 GPa, C_{44} = 163 ± 4 GPa, C_{12} = 111 ± 5 GPa, and C_{13} = 52 ± 9 GPa). Some physical properties of most common polytypes of SiC are shown in Table 1. Silicon carbide has high hardness, good flexural strength, good high temperature strength, low density, and is relatively less expensive compared to many other high hardness materials. SiC, due to covalent bonding, has among the highest known elastic modulus (~450 GPa) and has shear yield strength of about one tenth of the shear modulus [10].

Table 1: Properties of common SiC polytypes [11].

	3C(β)	4H	6H(α)
Space Group	T2d-F43m	C46v-P63mc	C46v-P63mc
Pearson Symbol	cF8	hP8	hP12
Lattice Constants A° (a, c)	4.3596	3.0730;10.053	3.0730;15.11
Density (gm/cm^3)	3.21	3.21	3.21
Bulk Modulus (GPa)	250	220	220

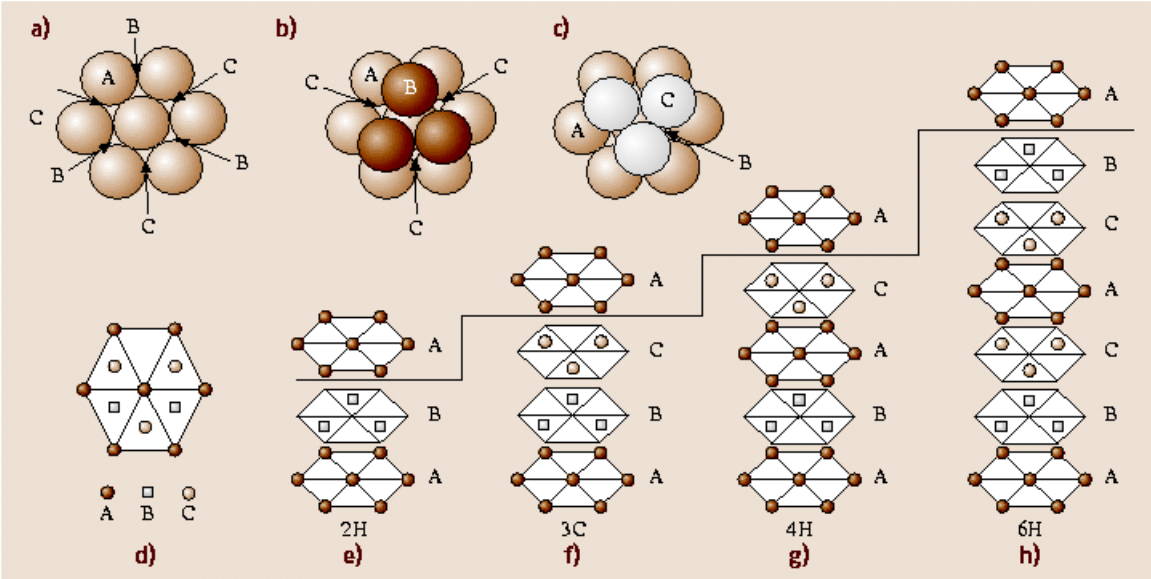

Figure 1: Stacking sequences in most common SiC polytypes [3].

SiC has superior creep behavior and wear resistance [12, 13] which make it an ideal material for use in wear resistant coatings in a variety of automotive components like pistons, valve heads, bearings etc and in micro-electromechanical systems. The physical (wide bandgap, high thermal conductivity and high electric field strength) and chemical properties of SiC-6H

polytype make it an ideal material for high temperature, high frequency, high power devices, including radar and microwave applications under extreme conditions [14]. SiC as a material for structural applications has received tremendous interest starting in the 1980's with the US Department of Energy efforts to develop ceramics for high temperature, high stress applications like gas turbine engines to increase their efficiency and life span. SiC has also received a lot of interest from the US Department of Defense due to its hardness, density and mechanical properties. SiC is used in coatings in military jet engines, heat exchangers in gas turbines for tanks and ships, composite armor and as the ceramic plates in bulletproof vests. Ceramics have an inherent brittleness and are very sensitive to flaws. Since structural applications of SiC involve mechanical loading and contact, an understanding of the mechanical anisotropy of SiC is needed. The performance of polycrystalline SiC in applications that involve high loading and contact depend on mechanisms that redistribute loads, reduce stress concentrations and dissipate elastic strain energy. Table 2 below shows the properties of some commercial polycrystalline SiC materials that will be studied in this research.

Table 2: Basic properties of commercial polycrystalline SiC.

Material	**Source**	**Av. Grain Size (μm)**	**Density g/cm^3**	**E (GPa)**	**Poisson's Ratio**	**K_{IC} (MPa. m$^{1/2}$)***
SiC-N	BAE Systems	3-5	3.212	453.7	0.171	2.75
SiC-HPN	BAE Systems	3-5	3.192	443.1	0.155	3.17
SiC-RN	BAE Systems	1.5-3	3.185	431.5	0.154	2.84
* Kic data listed is from various sources measured by different methods and should not be used for comparison in absolute magnitude ** Data is from various sources that include ultrasonic and mechanical testing.						

1.2 Nanoindentation

Nanoindentation, i.e probing mechanical properties at the nanometer scale has emerged as an important technique during the last decade for characterizing mechanical properties and behavior at small length scales. Although initial application of nanoindentation was for thin films [15-19] and small length scale properties [20, 21], recently, nanoindentation has been used as a characterization tool for high and low temperature testing [22], high strain rate testing [23], dynamic testing for storage and loss moduli [24], creep testing [25, 26] and testing properties in a variety of environments (liquids etc.) [27]. Nanoindentation systems, which represent the current state of the art for hardness testing machines, are effectively non-destructive. Due to the ability to analyze small specimens, considerable research is being done into further extending the capabilities of nanoindentation systems. Nanoindentation systems are now being used to investigate materials under dynamic conditions (scratch, creep, in-situ, etc.) which opens up the possibility to obtain new and unique information about materials. Nanoindentation is also being used to analyze new materials like nanocomposites to obtain more information about interface bonding. This is difficult to do with traditional testing methods.

1.3 Structure of Thesis

Chapter II gives an overview of instrumented indentation. Various concepts and the different methods of analysis are discussed. This chapter also reviews the current state of the art and the previous research done using spherical and pyramidal indenters. A detailed discussion of the various expressions used to calculate the hardness (H) and modulus (E) of a material using nanoindentation is presented in this section.

Chapter III gives an overview of the various objectives of this research and an overview of the current and previous research done in indentation testing of Silicon carbide (SiC).

Chapter IV describes the experimental methods, and various analytical equipment used in this research. The metallurgical preparation prior to indentation testing and characterization used after indentation are presented. The methods used and the results for tip-shape and area function calibration for different indenter geometries are also explained and discussed.

Chapter V contains the results and discussion of Berkovich and spherical indentation experiments performed on single crystal SiC-6H samples in different crystallographic orientations. This chapter discusses the elastic and plastic anisotropy of the SiC-6H samples and compares experimental results with theoretical elastic anisotropic contact analysis predictions.

Chapter VI contains the results of cracking in SiC-6H single crystal samples when indented in the <0001> direction using pyramidal indenters with varying centerline to face angles. This chapter also discusses the applicability of various models used in fracture toughness measurements.

Chapter VII contains the results and discussion of indentation experiments performed on different polycrystalline SiC ceramics. This chapter explores the energy absorbed during indentation concept as a way to analyze the indentation response of polycrystalline materials.

Chapter VIII presents an energy analysis of different materials, both single crystal SiC-6H<0001> and polycrystalline SiC using Berkovich indentation.

Chapter IX contains the results of flow properties for single crystal SiC-6H <0001> sample determined by indentation with a series of triangular pyramidal indenters.

CHAPTER 2. Indentation Testing

Moh's in 1812 [28] documented the first semi-quantitative hardness test by ranking the ability of one material to scratch another material of interest. Brinell in 1900 introduced the Brinell tester, which used a spherical indenter and measurement of the imprint on the material of interest to determine the Brinell hardness number. Meyer in 1908 first proposed hardness as a ratio of the load applied to the projected area of the indentation. Ludwik and Vickers in 1908 and 1925 [28] introduced hardness testers using conical and pyramidal indenters, which are still in use today. Hertz [29] developed a linear elastic solution for contact between two spheres to account for elastic deformation. Boussinesq [30] introduced the methods of potential theory to solve the contact problem between two linearly elastic isotropic solids. Figure 2 shows the stress fields beneath a spherical indenter based on the contact solution developed by Hertz and Boussinesq. Sneddon in 1948 developed the methods formulated by Hertz and Boussinesq to solve the contact problem between a rigid conical indenter and a semi-infinite half plane [31]. Later on in 1965, Sneddon also developed a contact solution for any arbitrary axisymmetric indenter and a semi-infinite elastic half space [32]. These analytical solutions by Hertz, Boussinesq, and Sneddon are based on certain assumptions, namely the specimen is an infinite half-space, the indenter has an ideal geometry with known parameters (perfect cone, sphere, etc.), and the material is linearly elastic. A majority of materials exhibit plastic flow during an indentation experiment. Sneddon's derivation, which depends on linear elastic assumptions, cannot be applied during loading of most indenters for which significant plasticity is observed. Various other researchers (Hill, Ford and Alexander, Dumas, Hill) investigated the plasticity during indentation.

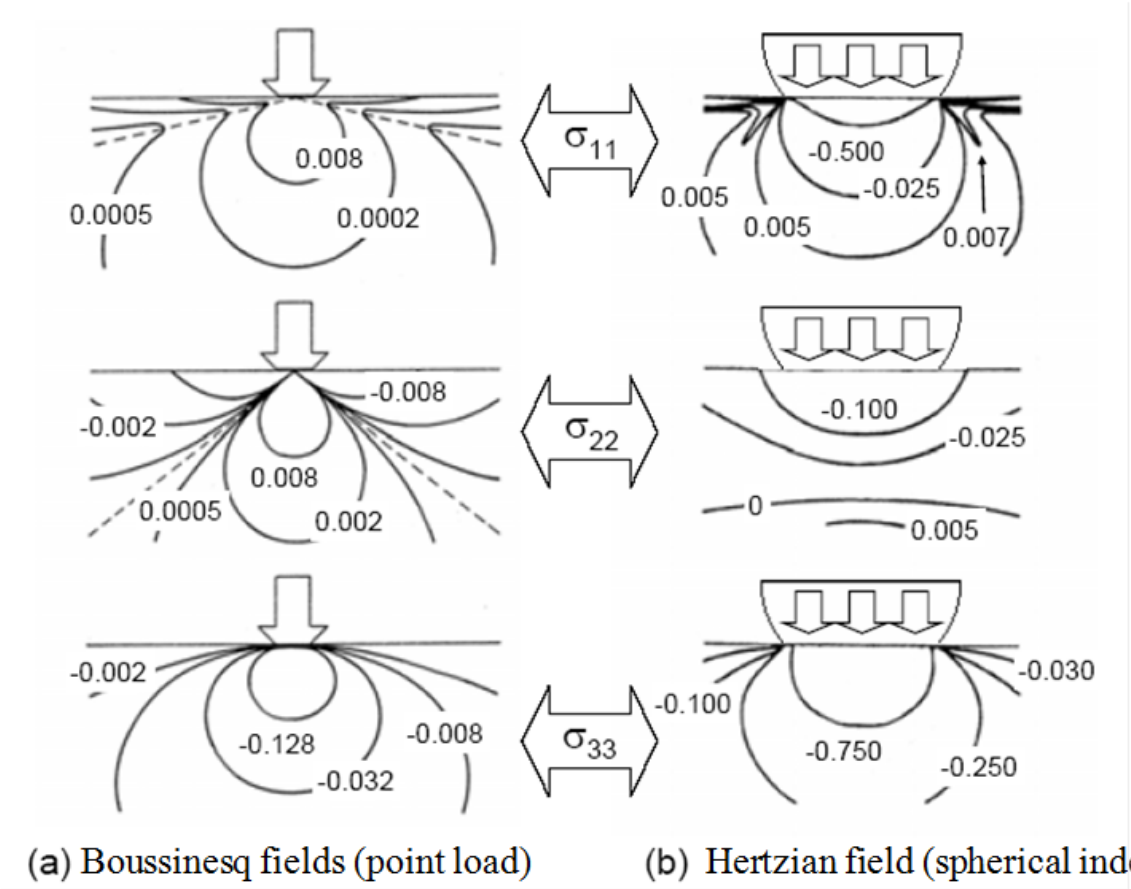

Figure 2: Stress fields beneath an indenter [33].

Alekhin, Ternovskii, Bulychev in the 1970's [34] and Pethica [35] and Loubet [36] in the 1980's along with several other researchers developed the use of depth sensing indentation tests. Ternovskii in 1974 first developed an equation (Equation 1 below) to relate the stiffness (S) to the reduced modulus (E^*) of the material using the load and displacement measured during the indentation test.

$$S = \frac{dP}{dh} = 2E^* \frac{\sqrt{A}}{\sqrt{\pi}} \tag{1}$$

The reduced modulus E^* is obtained from Young's modulus E and Poisson's ratio of the sample and the values of the indenter material ($E_i = 1141\ GPa$, $\nu_i = 0.07$ for diamond), using the relation (Equation 2),

$$\frac{1}{E^*} = \frac{1-\upsilon_m^{\,2}}{E_m} + \frac{1-\upsilon_i^{\,2}}{E_i} \tag{2}$$

Oliver [37] and Pharr [38] in 1992 demonstrated that the equation developed by Tenovskii is valid for axisymmetric indenters with an infinitely smooth profile and can be used to determine the elastic properties of a material. While the loading segment in a nanoindentation experiment for a majority of materials is elastic-plastic, the unloading stage is purely elastic. The method proposed by Oliver – Pharr in 1992 [37], which uses the unloading curve to estimate the modulus and hardness of a material, is one of the most widely used methods to calculate elastic properties of a material during nanoindentation and is the dominant analysis method in most commercial nanoindenters. Equation 3 below defines the hardness, where, P_{max} is the peak applied load, h_{max} is the displacement into the surface or the indentation depth at P_{max}, $A_c(h_c)$ is the projected contact area at that load, and h_c is the contact depth,

$$H = \frac{P_{max}}{A_c(h_c)} \quad \text{and} \quad h_c = h_{max} - \varepsilon\frac{P_{max}}{S} \tag{3}$$

S is the stiffness and ε is the constant depending on the indenter geometry. Oliver and Pharr [39] described the indenter shape factor (ε) in terms of effective indenter shape as shown in Figure 3. Figure 3 shows schematically the effect of pressure distribution under the indenter on the amount of recovery during unloading/reloading, which causes a deviation from flat punch behavior.

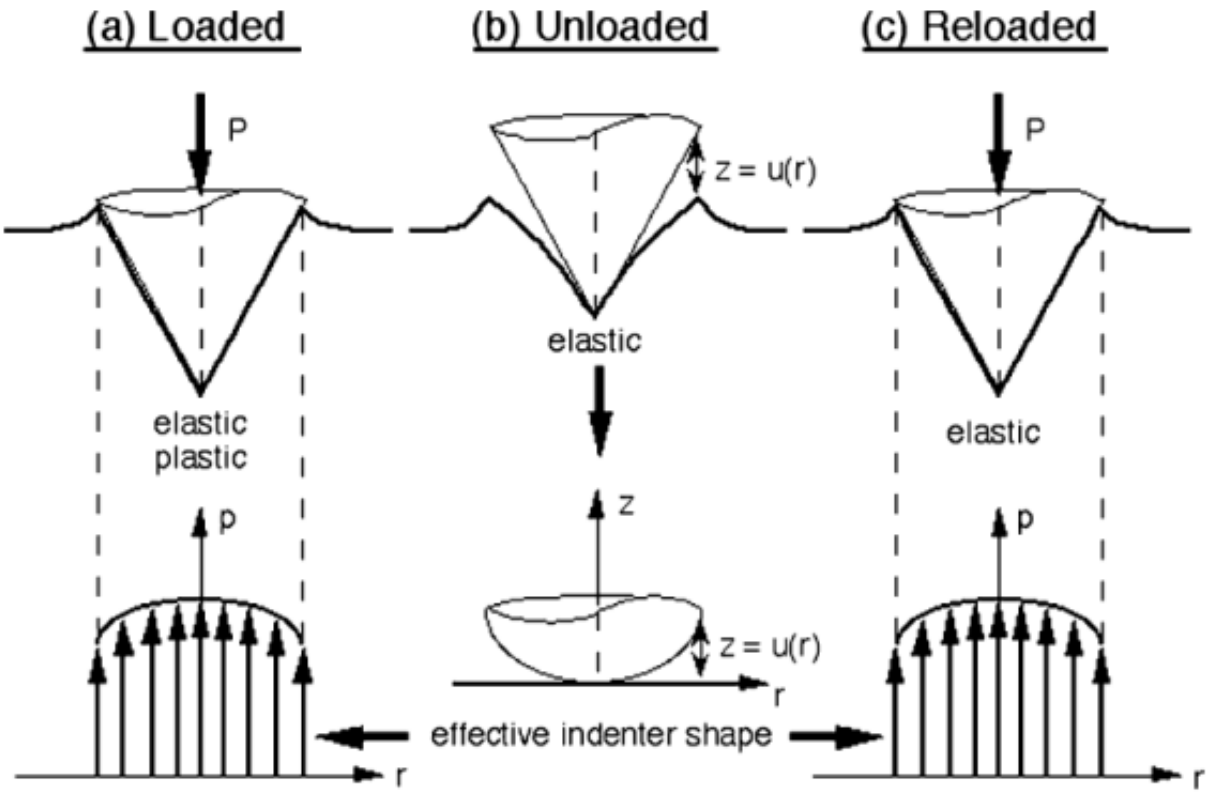

Figure 3: Effective indenter shape due to pressure distribution under the indenter [39].

Pharr and Bolshakov [40] developed a method based on finite element modeling to determine ε and found that ε is dependent on the material constants and the indenter shape. The values of ε were found to be in between 0.74-0.79 over a range of materials. Oliver and Pharr proposed a relationship between the reduced modulus of the material and the hardness during an indentation experiment as shown in Equation 4 below,

$$\frac{H}{E_r^2} = \frac{4\beta^2}{\pi}\frac{P}{S^2} \tag{4}$$

where, β is a dimensionless parameter that accounts for non-axisymmetric indenter shapes and is usually taken as 1.034 for Berkovich indenters. Table 3 shows the geometry, constants and the correction factors of the different indenter tips commonly used for nanoindentation experiments. Figure 4 below shows the indentation parameters for two frequently used indenters- spheres and triangular pyramids. For the pyramid, α is the effective cone angle and θ is the semi-angle.

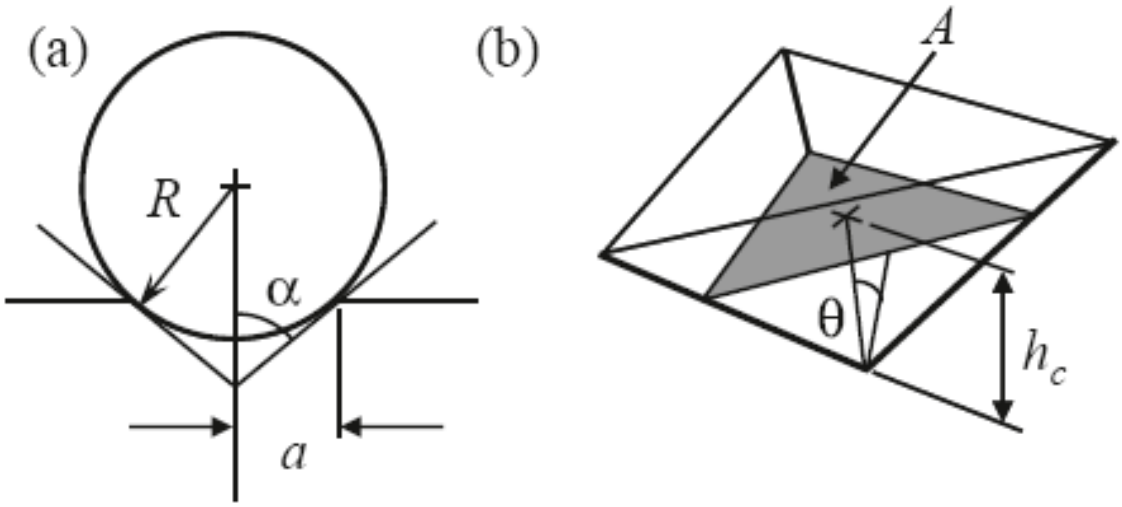

Figure 4: Indentation parameters for (a) Spherical and (b) Berkovich indenters.

Table 3: Indenter geometry for commonly used tips [33].

Indenter type	Semi angle (θ)	Effective cone angle (α)	Intercept factor (ε)	Geometry correction factor (β)	Projected area
Berkovich	65.3 °	70.3 °	0.75	1.034	$A = 3h_p^2\tan^2\theta$
Cube Corner	35.26 °	42.28 °	0.75	1.034	$A = 3h_p^2\tan^2\theta$
Cone	α	α	0.72	1	$A = \pi h_p^2\tan^2\alpha$
Knoop	θ_1=86.25 ° θ_2=65 °	77.64 °	0.75	1.012	$A = 2h_p^2\tan\theta_1\tan\theta_2$
Sphere	N/A	N/A	0.75	1	$A \approx \pi 2Rh_p$
Vickers	68 °	70.32 °	0.75	1.012	$A = 4h_p^2\tan^2\theta$

2.1 Spherical indentation

Spherical indenters are popular for investigating the onset of plasticity, i.e, the transition from elastic to plastic deformation. They are also useful in replicating and measuring the contact damage in certain service conditions. The yield strength of a material and the stress strain curve can in principle be obtained using spherical indentation. Figure 5 shows a schematic of a spherical indentation experiment. According to Hertzian contact theory [29] the mean contact pressure is proportional to the square root of the penetration depth (h) according to:

$$p_m = \frac{P}{\pi a^2} = \frac{4}{3\pi}\sqrt{\frac{h}{R}} \tag{5}$$

where, p_m is the mean contact pressure, a is the contact radius, E^* the reduced elastic modulus, and R is the radius of the indenter tip.

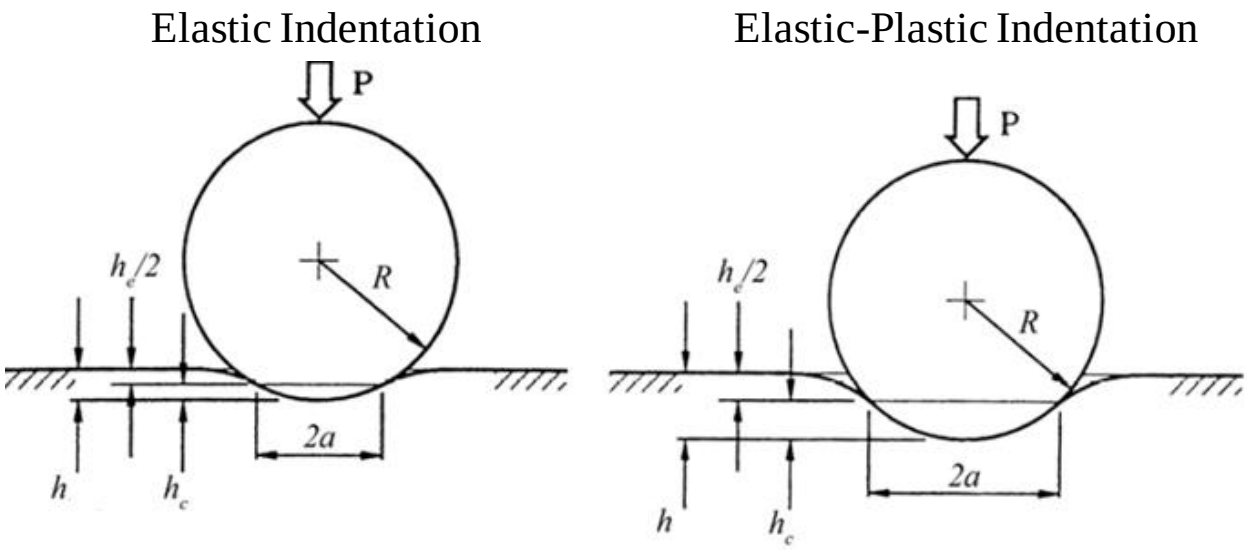

Figure 5: Schematic of a spherical indentation [41].

Herbert et al. [42] developed a method to obtain the stress strain curves of metals and metallic alloys using spherical indentation based on models developed by Hertz [29], Oliver-Pharr [37] and Tabor [43]. Spherical indentation can be used to study defect nucleation and propagation events since the transition from purely elastic to plastic deformation during an indentation experiment which is marked by sudden displacement excursions called “pop-in” in the load displacement (*P*-*h*) curves. Gane and Bowden [44] first observed pop-ins in metal crystals and associated them with dislocation nucleation or the sudden onset of plasticity. Crack nucleation and propagation [45], phase transformations [10] and mechanically induced twinning [46] have also been associated with pop-in behavior. Neglecting thermal contributions and the possible formation of stacking faults, the shear stress necessary for homogeneous dislocation nucleation can be calculated from the elastic self-energy stored in a dislocation loop [47]. Homogeneous dislocation nucleation is only possible if there are no mobile or pre-existing

dislocations near the indenter. The maximum critical shear stress (τ_{th}) required for dislocation nucleation is given by,

$$\tau_{th} \approx \frac{Gb}{2\pi d} \tag{6}$$

where, G is the shear modulus and b is the magnitude of the Burger's vector and d is the separation distance between two neighboring planes. The maximum shear stress beneath a spherical indenter according to Tresca criterion is a function of the mean contact pressure indentation depth h and the tip radius R [48] and is given by:

$$\tau_T = (0.46)\, p_m = (0.46)\frac{4}{3\pi}\sqrt{\frac{h}{R}} \tag{7}$$

Gouldstone et al. [49] also developed an equation for the maximum shear stress beneath an indenter as shown below,

$$\tau_{max} = 0.31\left(\frac{6P}{\pi^3}\right)^{1/3}\left(\frac{E^*}{R}\right)^{2/3} \tag{8}$$

Polyani and Orowan derived a simple model to determine the cleavage strength of a perfect crystal assuming that there are no defects, no stress concentrations at the crack tip and that all the atoms separate simultaneously when they reach a critical separation distance. The relation is:

$$\sigma_{th} = \frac{1}{2}\sqrt{\frac{E\gamma}{a}} \tag{9}$$

where, γ is the surface energy of the cleaved surfaces and a is the original equilibrium interplanar spacing for the cleaved planes. Since accurate measurement of surface energy in different

directions is extremely difficult, this equation can be further simplified assuming that the critical separation distance required for cleavage is of the same order of the initial separation distance. This yields the simple expression:

$$\sigma_{th} \approx \frac{E}{\pi} \tag{10}$$

The maximum tensile stress in a spherical indentation experiment is:

$$\sigma_{max} = \left(\frac{1-2v_m}{2\pi}\right)\left(\frac{4E^*}{3R}\right)^{2/3} P^{1/3} \tag{11}$$

Field and Swain [41] developed a model based on Sneddon's [31, 32] work to calculate the elastic-plastic response of a material to spherical indentation. The Field and Swain technique describes the onset of full plastic flow using,

$$\left(\frac{p_m}{Y}\right) = 3 \tag{12}$$

where, Y is the yield stress of the material. The mean contact pressure (P_m) is equivalent to the hardness of the material after the first pop-in event. This gives the value of the critical load (P_c) corresponding to the onset of plastic flow (with no work hardening) to be

$$P_c = \frac{9}{16}\left(\frac{R}{E^*}\right)^2 3\pi\left(Y^3\right) \tag{13}$$

2.2 Pyramidal Indentation

The indenter proposed by E.S Berkovich in 1951 [50] is the most commonly used three sided pyramidal tip for nanoindentation experiments. The Berkovich indenter is preferred because of its well defined geometry. A typical indentation load displacement curve obtained with a Berkovich indenter is shown in Figure 6.

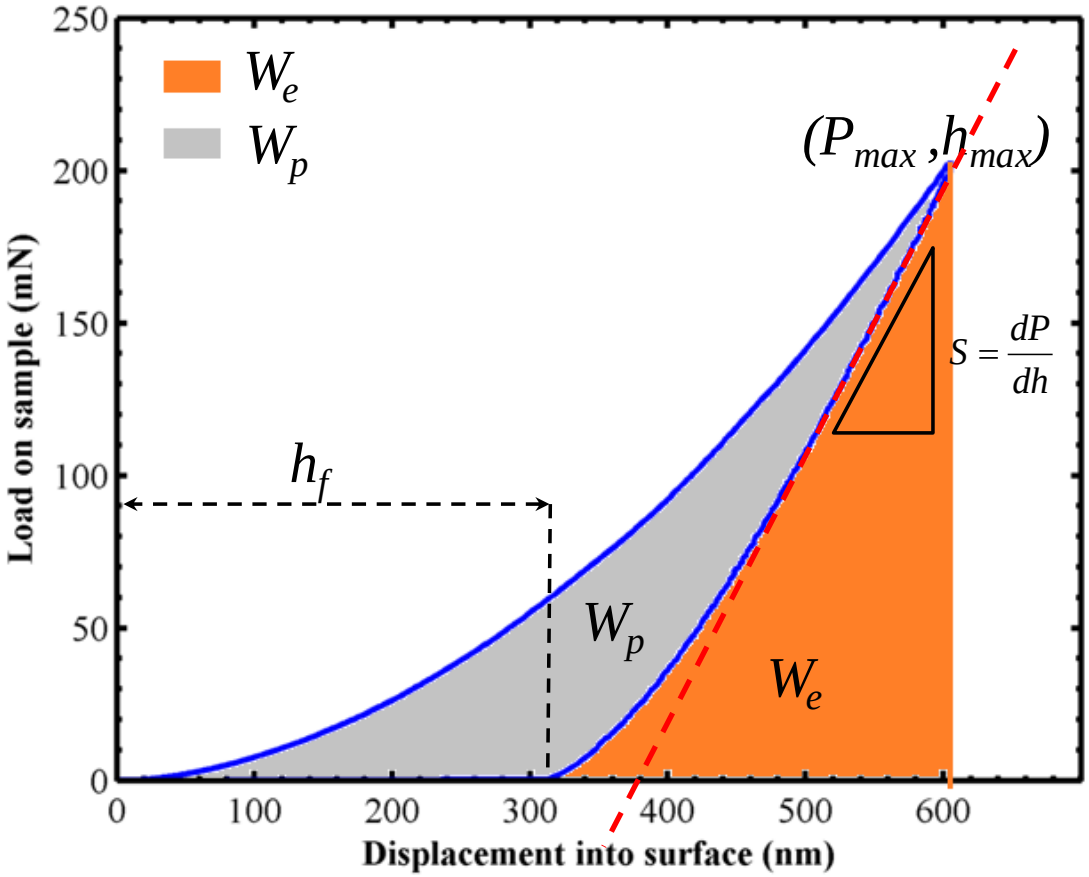

Figure 6: Schematic *P-h* curve for Berkovich indentation of a homogeneous elastic-plastic solid.

In Figure 6, W_e (the elastic work done) is the area under the unloading curve, W_T (total work done) is the area under the loading curve W_p is the Irreversible or plastic work (W_T-W_e).

Cheng and Cheng [51, 52] developed a method to calculate the modulus and hardness of a material based on the area under the loading and unloading curves. They developed a relation between the indentation hardness and the reduced modulus using scaling analysis and finite element simulations in terms of work which is given by:

$$\frac{W_e}{W_T} \approx \lambda \frac{H}{E_r} \tag{14}$$

where, λ depends on the indenter geometry and has values were found to be in the range from 5.33 to 4.678 [51-53]. Malzbender et al. [54-56] developed different formulations to calculate the hardness and modulus of a material based on the area under the load displacement curves. They concluded that the hardness and modulus calculated using these methods was independent of the contact area. Using the Equation 14 above and the equation developed by Oliver and Pharr, the relationship between the indentation hardness and modulus in terms of work done can be expressed as:

$$H_{CC} = \left(\frac{1}{\lambda^2}\right)\left(\frac{W_e}{W_T}\right)^2 \Big/ \left(\frac{4\beta^2}{\pi}\frac{P}{S^2}\right) \tag{15}$$

$$E^*_{CC} = \left(\frac{1}{\lambda}\right)\left(\frac{W_e}{W_T}\right) \Big/ \left(\frac{4\beta^2}{\pi}\frac{P}{S^2}\right) \tag{16}$$

Chen and Bull [57] developed a model which relates the energy done during indentation (Equation 17) using numerical simulations based on the work of Cheng and Cheng to incorporate the work hardening exponent *n.* It yields:

$$\frac{W_e}{W_T} = \left(\frac{1.5\pi\left(1.24+0.2n\right)}{\left(2.24+0.2n\right)}\right)\frac{\pi\, H}{\beta\, E_r}\left(Tan\,\alpha\right)\left(\frac{1}{\left(1+\left(\frac{\pi\varepsilon\, H}{2\beta\, E_r}Tan\,\alpha\right)\right)}\right) \tag{17}$$

The reduced indentation modulus and hardness can be obtained from the above relationship using Equation 14 which gives,

$$E^*_{CB} = \left(\frac{\left(\frac{W_e}{W_T}\right)\left(Cot\,\alpha\right)}{\left(\left(\frac{1.5\pi\left(1.24+0.2n\right)}{\left(2.24+0.2n\right)}\right)-\pi\varepsilon\frac{W_e}{2\,W_T}\right)}\right)\Bigg/\left(\frac{4\,\beta\, P_{max}}{\pi\, S^2}\right) \tag{18}$$

$$H_{CB} = \left(\frac{\left(\frac{W_e}{W_T}\right)\left(Cot\,\alpha\right)}{\left(\left(\frac{1.5\pi\left(1.24+0.2n\right)}{\left(2.24+0.2n\right)}\right)-\pi\varepsilon\frac{W_e}{2\,W_T}\right)}\right)^2\Bigg/\left(\frac{4\,P_{max}}{\pi\, S^2}\right) \tag{19}$$

A comparison of the values of hardness and modulus obtained using the method outlined by Cheng-Cheng with those obtained using the Oliver-Pharr approach should give an indication of the pile-up/sink in behavior of the material during nanoindentation experiments. The Cheng-Cheng model was developed using continuum mechanics and Mises effective stress which applies to metal plasticity and also agrees with results on ceramics and silica [51, 52]. Three sided pyramidal tips with different axis to face angles can be used to produce different effective strains in a material. Jang et al. [58] studied the effect of indentation using different axis to face angles (Figure 7) in silicon and germanium. The applied stress intensity factor at crack tips resulting from indentation tests changes with different axis to face angles. This can be helpful in studying crack propagation and crack initiation.

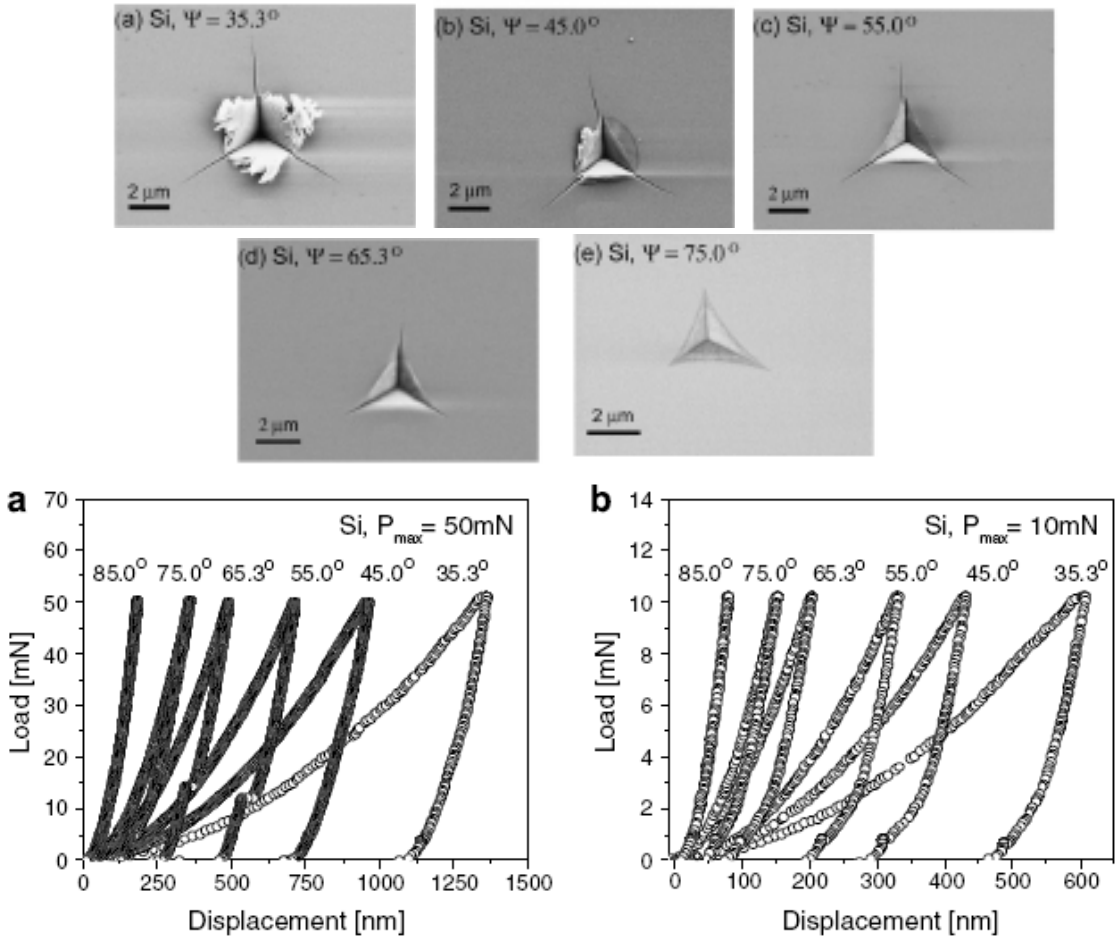

Figure 7: Influence of indenter angle on cracking in Si [58].

2.3 Fracture toughness measurement using nanoindentation

Nanoindentation has proved to be a useful tool to evaluate the fracture toughness (mode I) of materials based on the formation of cracks at the corners during indentation. The length of cracks which extend due to the residual stress field can be related to the fracture toughness of the material. Lawn and Evans [59] proposed the use of Vickers indentation for fracture toughness measurement in the 1980s to relate the plane-strain, mode-I, critical stress intensity factor (K_{IC})

to the observed crack lengths. The Lawn equation (Equation 20 below) is based on Hill's expanding cavity solution for an elastic-plastic solid assuming a half-penny crack.

$$K_{IC} = \alpha\left(\frac{E}{H}\right)^{1/2}\left(\frac{P}{c^{3/2}}\right) \tag{20}$$

In this equation, P is the indentation load, E is Young's modulus, H is the hardness, c is the total length from the center of the indent to the end of crack and α is a constant related to the crack morphology and the shape of the indenter used. From the expressions proposed by different researchers over the last two decades, those proposed by Anstis [60], who fitted Equation 20 using experimental data for brittle materials over a range of K_{IC} (1 to 12 MPa.m$^{1/2}$), and Laugier [61] who modified Equation 20 according to specifics of the crack geometry, have been the most commonly used. Gong et al. [62] also suggested a modification for the Anstis equation to include the indentation size effect at low loads. The Laugier equation (Equation 21) which was developed for determining the fracture toughness of WC-Co (Tungsten Carbide – Cobalt) ceramics for Palmquist cracks, is given by

$$K_{IC} = \chi_v\left(\frac{l}{a}\right)^{-1/2}\left(\frac{E}{H}\right)^{2/3}\left(\frac{P}{c^{3/2}}\right) \tag{21}$$

where, l is the length of the length of the crack, a is the length from the center of the indent to the corner of the indent, and E, H, P and c have the same meaning as in Equation 20, χ_v was found to be 0.015 for radial cracks [61]. Anstis and Laugier developed equations primarily for the four sided Vickers indenters which were then further improved by Dukino and Swain in 1992 [63] for three sided pyramidal indenters by taking into account the number of symmetric cracks proposed by Ouchterlony. Fitting of the Laugier equation (Equation 21) gave a χ_v value of 0.016 for a Berkovich indenter [63]. Conventional indentation cracking methods for fracture toughness

measurement requires a long crack larger than the indent size. In ceramics, the indent size is comparable to the equilibrium crack size [59, 60]. The role of plasticity is difficult to evaluate in hard ceramics which gives a more qualitative measure of the toughness when measured using indentation cracking methods [58].

2.4 Estimation of flow properties using nanoindentation experiments

Extraction of (stress, strain) flow properties using the values of hardness and modulus obtained during nanoindentation experiments relies on the calculation of constraint factors and characteristic strains for a given geometrically self-similar indenter and an assumed constitutive relationship. A unique solution can be obtained using pyramidal indenters with different centerline to face angles combined with finite element analysis. Various researchers have used nanoindentation data to obtain stress-strain curves for a material. Figure 8 summarizes Tabor's concept for estimating the stress-strain and the method used by Shim et al. [64]. The finite element procedure starts with an initial guess of the yield strength. It is assumed that the materials have a linear elastic response up to yield point, follow the Holloman stress strain law, the constraint factor relates hardness to flow stress and that the conical finite element simulations used approximates the behavior of the three sided pyramid indenter used in experiments.

Since it is not possible to get information about plasticity in ceramics using uniaxial testing at room temperatures, nanoindentation with different centerline to face angle indenters can be used to extract information about the plasticity of these ceramics. The constraint on deformation due to the indentation geometry produces plastic deformation in these materials, even though they are very brittle in conventional tension or compression tests.

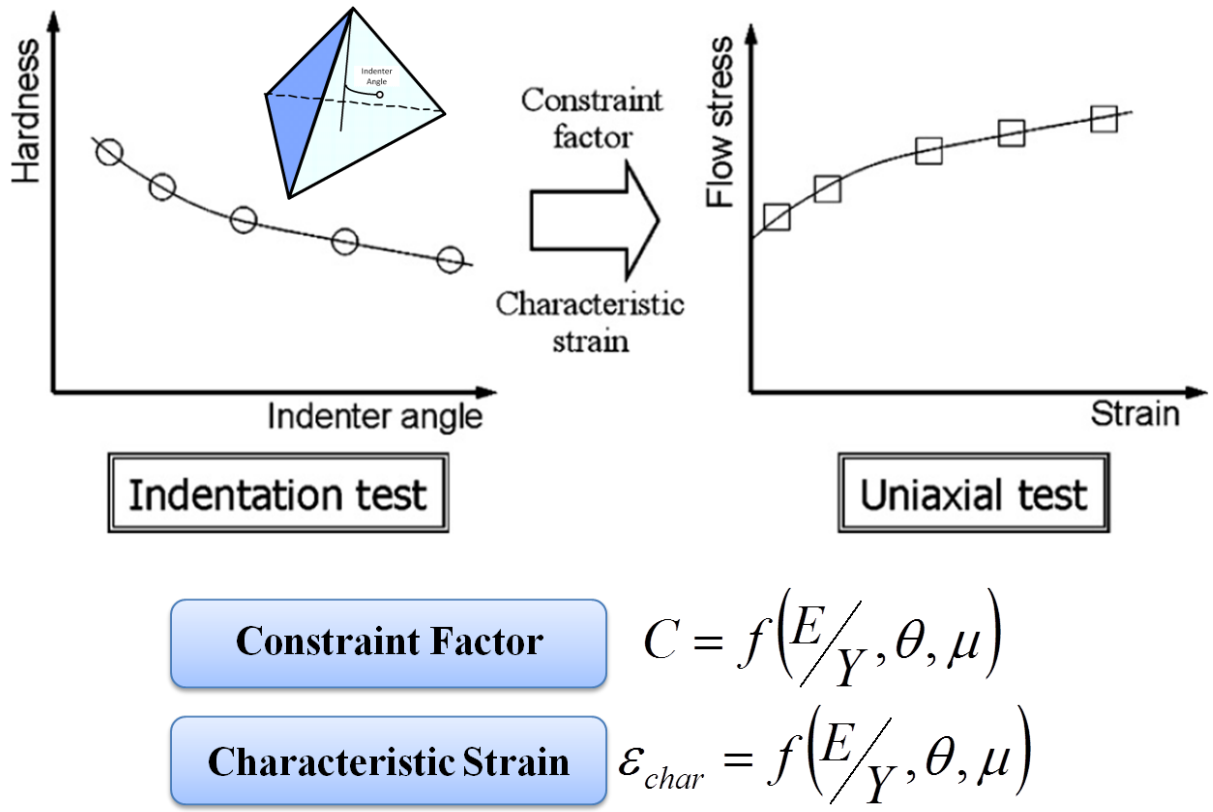

Figure 8: Tabor's concept for estimating stress-strain using indentation hardness [85].

2.5 Important considerations during nanoindentation experiments

2.5.1 Thermal Drift and Creep

Creep and thermal drift are two phenomena which need to be taken in account during nanoindentation experiments. Thermal drift occurs when the entire indentation system is not in thermal equilibrium. This results in errors in displacement measurements due to the thermal expansion or contraction. Drift measurement is normally done by holding a fixed load (20% of peak load) during the unloading portion of the test and measuring the displacement over time. Creep deformation can be observed during the hold period at peak load during a nanoindentation experiment. Chudoba et al. [65] studied the influence of creep behavior on the hardness and

modulus measurements. Creep effects are minimized by holding for a fixed time at peak load such that the creep displacements become negligible during unloading.

2.5.2 Tip, Area function and nanoindenter calibrations

Nanoindentation systems require several calibration measurements, (1) Frame compliance calibration (2) Indenter area function calibration and (3) Tip shape calibration. These calibrations require standard materials. An ideal standard calibration material should have the following properties.

1. Does not show a pile-up or sink in behavior.
2. Is elastically isotropic.
3. Gives consistent modulus values over a range of indentation depths.
4. Is easily obtainable with a highly polished surface (optically flat).
5. Is thermally stable and shows little creep.
6. Shows little or no indentation size effect (ISE).

The origin of the indentation size effect, which is characterized by a decrease in the indentation hardness with an increase in indentation size/depth, is an active research topic in the nanoindentation research field. Most materials will show some pile-up or sink in behavior. A material with a high H/E^* ratio will reduce pile-up during an indentation experiment. Since the area function determination requires knowledge of the compliance of the nanoindentation system, one of the most important calibrations used in nanoindentation testing is the frame compliance calibration. A material with a low H/E^* ratio is generally used for this to ensure a large and stiff indenter contact area. Aluminum and tungsten, which are both elastically isotropic

with a low H/E^* ratio, are most commonly used for frame compliance calibration. Fused silica is a material commonly used for the indenter area function calibrations because of its elastic isotropy, economy and creep properties. Fused silica is relatively hard and stiff, which ensures that the loads applied for small indentation depths are large enough within the force resolution of the nanoindenter. Table 4 below shows the material properties of the commonly used calibration standards.

Table 4: Material properties of calibration standard used in nanoindentation [33].

Material	**Elastic Modulus (GPa)**	**Poisson's Ratio (v)**	**Hardness (GPa)**
Diamond	1147	0.07	>100
Fused Silica	72.1	0.17	8.8
Sapphire	370	0.25	30
Tungsten	441	0.28	6.6

CHAPTER 3. Literature Review and Objectives of this research

3.1 Indentation testing of Silicon carbide (SiC)

Most commercial polycrystalline SiC is composed of the SiC-6H polytype. Elastic modulus measurements of polycrystalline SiC have been made using various methods, including sonic resonance, tensile, flexural, and indentation techniques with both Vickers indenters and nanoindentation [12, 13]. SiC has a high resistance to yielding, but unlike metals, cracks and pre-existing flaws easily propagate because there is very limited dislocation mediated plastic deformation. A few researchers have attempted to investigate the fracture strength of single crystal SiC-6H using microspecimens [66-69]. Henshall et al. [69] found that the fracture toughness of single crystal SiC-6H is 3.3 $MPa.m^{1/2}$ using 3-point bend specimens. The 3- point bend specimens were aligned such that the notch was in the (11-20) plane and the direction of crack propagation was <1-100>. Liang et al. [70] measured the fracture toughness of polycrystalline SiC and compared it to single edge-notched beam SENB measurements and found the fracture toughness to be around 3 $MPa.m^{1/2}$. Sharpe et al. [66, 67] found the fracture strength of SiC-6H microspecimens to be 0.5-1.5 GPa in tension, when the tensile axis was orientated parallel to the <10-10> direction. The results of Henshall and Sharpe show that the measurements are highly dependent on surface flaws and pre-exisiting defects. Shaffer et.al [71] studied the hardness anisotropy in SiC-6H single crystals using a Knoop indenter with a 100 g load by indenting on the (10-10) and (11-20) planes with the long axis parallel or perpendicular to the <0001> directions. The maximum hardness measured was 29.17 GPa in the <0001> direction with the long axis parallel to the <11-20> direction and the minimum was 21.29 GPa in the <10-10> direction with the long axis parallel to the <0001> direction. The results from Shaffer et al. are shown in Table 5.

Table 5: Hardness anisotropy in SiC-6H using a Knoop indenter by Shaffer et al. [71].

Face	Indenter orientation	Hardness (kg/mm²)		
		Lowest	Average	Highest
(0001)	Parallel $(10\bar{1}0)$	2900	2917 ± 10	2935
(0001)	Parallel $(11\bar{2}0)$	2917	2954 ± 27	3026
$(10\bar{1}0)$	Parallel *c*	2027	2129 ± 45	2179
$(10\bar{1}0)$	Perpendicular *c*	2700	2755 ± 40	2827
$(11\bar{2}0)$	Parallel *c*	2321	2391 ± 34	2434
$(11\bar{2}0)$	Perpendicular *c*	2717	2755 ± 22	2790

Nihara et al. [72] and Swayer et al. [73] also performed Knoop hardness measurements on the (0001), (10-10) and (11-20) planes and concluded that the primary-slip system in SiC-6H on which plastic deformation under indentation occurs preferentially is (0001)<11-20> at low temperatures and (1010) <11-20> at high temperatures. Henshall et al. [74] in 1985 used a combination of Vickers and Berkovich indentation in SiC-6H on the (0001) and the (1-100) planes along with SENB measurements to determine the anisotropy of the fracture toughness. Miyoshi et al. [75] showed that friction, deformation, and fracture of the SiC (0001) surface depends on the crystallographic orientation and that the anisotropies are primarily controlled by the slip system (10-10) <11-20> and cleavages of (10-10) and (0001). Qian et al. [76] measured the Knoop and Vickers hardness and fracture toughness of SiC-6H single crystals and observed that the values at the asymptotic-hardness region are significantly smaller (~20%) than those at low loads indicating an indentation size-effect. Page et al. [10] reported the behavior of single crystal alumina and silicon carbide using nanoindentation in 1991. It is generally accepted that dislocation motion is difficult in SiC-6H due to the hexagonal structure (few slip systems) and covalent bonding which results in a high Peierls' stress. In order to study inelastic deformation

mechanisms in SiC-6H Page et al. [10, 77] performed TEM measurements (Figure 9) of the deformation zones beneath the indenter and found that plastic deformation is accommodated entirely by nucleation and outward propagation of dislocations on the basal plane, which points to the importance of dislocation mediated plasticity during indentation of SiC-6H. In the absence of flaws or pre-existing dislocations, plastic deformation occurs when the maximum shear stress below the indenter tip approaches theoretical strength, whereas cleavage occurs when the maximum tensile strength around the tip exceeds the theoretical cleavage strength. The location of the indent and the stress states during loading are necessary to determine which mode controls the deformation or cracking. Kitahara et al.[78] concluded that the primary cleavage planes both in SiC-6H are less resistant to fracture in some cases during indentation experiments which means cleavage of single crystals is an important factor in addition to grain boundary failure in the assessment of cracking in polycrystals.

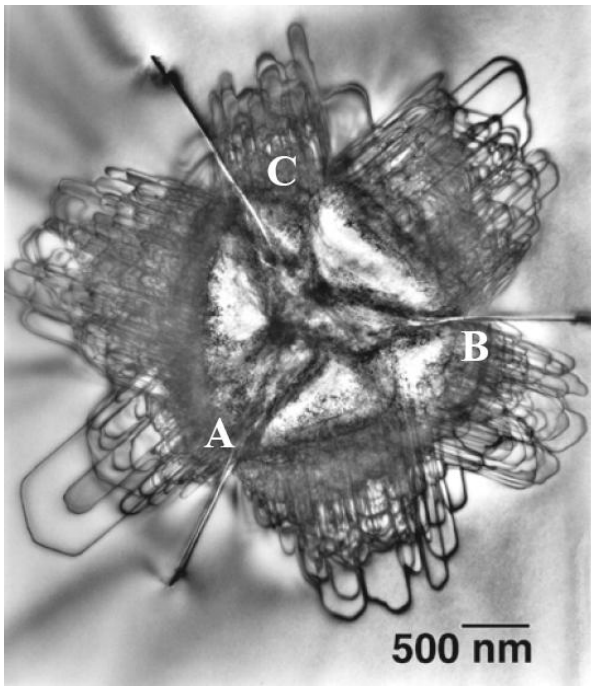

Figure 9: TEM image of Berkovich nanoindentation in SiC-6H in <0001> direction showing a rosette of basal dislocation loops [77].

Another study by Yan et al. [79] showed evidence that single crystal SiC-6H transforms into polycrystalline SiC directly under the indenter tip, in addition to forming microcracks and basal plane dislocations. Shim et al. [64] used a combination of nanoindentation experiments with pyramidal indenters and finite element simulations to extract flow properties of SiC-6H. Previous research on commercial polycrystalline SiC materials by Wereszcak et al. (Figure 10), using spherical indenters showed that the cracking features and the load displacement curves for different forms of SiC are different. This indicates a difference in the impact response of the different SiC polycrystalline samples which can be studied using indentation experiments. Various other researchers have also used nanoindentation using Berkovich indenters to evaluate the modulus and hardness of polycrystalline ceramics [80, 81].

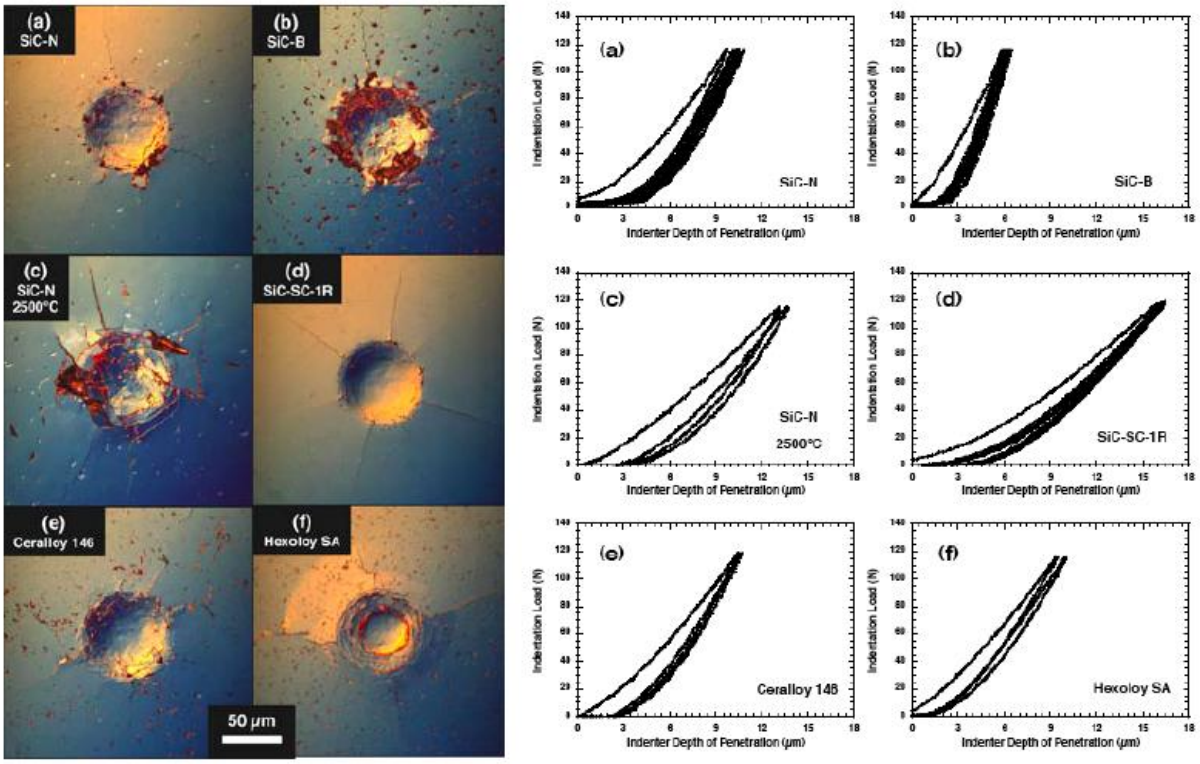

Figure 10: Hertzian Indentation tests with a 300 µm diameter diamond sphere [82].

3.2 Objectives of this research

The primary goal of this research is to understand the response of single and polycrystalline SiC to blunt and sharp indenters. This research focuses on experimental testing of single and polycrystalline SiC to understand the initiation and crack propagation in SiC and the relationships between fracture and plasticity. The validity of fracture toughness measurement using indentation cracking methods when the crack size is comparable or less than the contact size will be studied. This research will increase the fundamental understanding of the role of microstructural variables like grain size, grain boundary fracture strength, grain aspect ratio, etc. on deformation and fracture mechanisms in polycrystalline SiC ceramics and the role of material properties in energy absorption ability of the ceramic. These microstructural parameters can be varied during processing to enhance the impact performance of the material.

Objective 1: Study the elastic and plastic anisotropy in SiC-6H single crystal

Anisotropy in polycrystalline materials is the result of texture. The presence and amount of preferred grain orientation in a polycrystalline sample determines the degree of anisotropy in bulk material properties. It is therefore necessary to study basic properties like the elastic modulus (E) and hardness (H) of single crystal SiC-6H in different orientations to determine the role of anisotropy on the fracture behavior of the polycrystalline materials. Nanoindentation experiments using pyramidal indenters with different face angles and spherical indenters with different diameters will be used to study the mechanical response of SiC-6H single crystals in different crystallographic orientations. The modulus obtained from experimental results in different orientations will be compared to the values obtained using theoretical elastic contact prediction [83, 84]. Gao et al. [83] and Li et al. [84] used anisotropic elastic contact theory to calculate the indentation moduli, resolved shear stress and the Hertzian stress field for different

crystallographic indentation orientations. Using single crystal elastic constants a model was developed to calculate the E_{eff} in different indentation directions of a SiC-6H single crystal. This E_{eff} is converted to E using the following equation,

$$1/E_{eff} = (1-\upsilon_m{}^2)/E \quad (22)$$

where, ν_m is the Poisson's ratio of the material.

Objective 2: Experimental Evaluation of fracture and plastic flow of single and polycrystalline SiC for blunt and sharp contacts

Goal 1: Indentation cracking and fracture toughness measurement in single and polycrystalline ceramics

Measurement of fracture toughness using conventional indentation methods depends on the formation of a long crack that propagates and arrests in a stabilizing stress field. This toughness measurement, which depends on calculating the driving force by measuring the crack lengths, cannot be used for short cracks and when the crack bridging zone is larger. The applied stress intensity factor can be changed by using three sided pyramidal indenter with varying centerline to face angles.

Goal 2: Elastic and plastic properties of commercial polycrystalline SiC ceramics

Nanoindentation experiments using pyramidal indenters with varying axis to face angles and spherical indenters with different radii will be conducted on polycrystalline SiC ceramics with different microstructures (grain size, grain boundary phases etc.). The results will be used to obtain the basic properties of the material like modulus and hardness. Scanning electron

microscopy will be used to study the morphology of the residual impression after indentation. These experiments will be used to obtain flow stress data at different strains in the sample, which will help study the plasticity of the polycrystalline ceramics.

Goal 3: Energy analysis of load displacement curves for single and a polycrystalline ceramics

Area under the irreversible part of the load-displacement curve during a nanoindentation test is a direct measure of the energy dissipated during contact. Nanoindentation experiments carried out using a Berkovich tip at different peak loads will be used to obtain a relationship between the ratio of elastic energy to the total energy and the microstructure of the material.

Goal 4: Extraction of flow properties of single and polycrystalline ceramics using pyramidal indenters with different angles.

Finite element analysis using equivalent cones will be used in conjunction with the measured hardness values to find the yield strength and the work hardening exponents for single crystalline SiC. Since the different pyramidal indenters induce different characteristic strains in the material, this information can be used to generate a stress strain curve for the material.

CHAPTER 4. Materials and Methods

4.1 Nanoindentation

A Nanoindenter XP® (Nano Instruments Innovation Center, MTS Corporation, Knoxville, TN) was used to perform nanoindentation experiments at ambient temperature using Berkovich, pyramidal and spherical tips of varying radii on both single and polycrystalline SiC samples used in this research. All nanoindentation experiments were done using the CSM (Continuous Stiffness Measurement) technique [37] which gives the load on the sample and the contact stiffness as a function of the displacement of the indenter into the samples. The single crystal samples (semiconductor-grade Cree Research, Inc., Durham, NC) used in this study was electronics grade α-SiC (6H polytype). The crystal was transparent with a greenish color from the N impurity with EPI grade polished Si-face. The single crystal wafer was broken along the cleavage planes in the <a> direction and then mounted in resin. Polishing of the mounted samples was done by mechanical polishing with SiC grit paper followed by polishing with Buehler MasterMet 2 non-crystallizing colloidal silica (SiO_2) polishing suspension (0.02 μm) using a vibratory polishing machine. The SiC-6H Cree samples were indented using a Berkovich indenter, different pyramidal indenters (45°, 55°, 65°, 75°) and spherical indenters with different radii, perpendicular to the (0001) and the (-12-10) plane. Single crystal SiC-6H samples from Nitride Crystals Inc. were also used to study the mechanical anisotropy of SiC-6H. The crystals were cut in different orientations using a diamond saw. A schematic of the zenith angle geometry in the SiC-6H single crystal is shown in Figure 11 below. The samples were then mounted in resin and mechanically polished with SiC grit paper followed by 120 hours in colloidal silica using a vibratory polisher prior to nanoindentation. Nanoindentation was conducted using

Berkovich, different pyramidal and spherical indenters with different radii using the same method as used for the Cree SiC-6H samples.

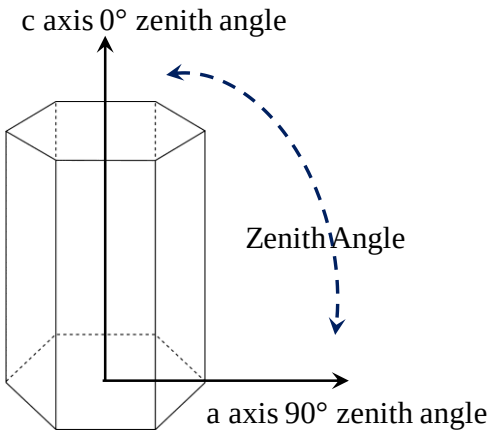

Figure 11: Zenith angle geometry for SiC-6H single crystal

The commercial polycrystalline SiC samples were obtained from different vendors and are designated SiC-N, SiC-HPN and SiC-RN. Basic physical properties of the polycrystalline SiC samples are listed in Table 3. The commercial polycrystalline samples were cut and then mechanically polished prior to nanoindentation. The final polishing was done using a water based non-crystallizing colloidal silica solution similar to the single crystal samples. Scanning electron microscopy was used to image the post indentation residual impressions made by different indenters on various SiC samples. A Zeiss Auriga dual beam FIB/SEM instrument was used for scanning electron microscopy. A Nikon interference microscope was also used to characterize the amount of pile-up post indentation in single crystal samples.

4.2 Laue Diffraction analysis to determine zenith angles

The polished SiC-6H Nitride Crystal Inc. samples along different orientations were then analyzed using a Laue diffractometer to determine the exact zenith angles. Figure 12 below shows the Laue patterns for the different orientations. The software package Orientexpress was then used to analyze the Laue diffraction patterns to determine the exact zenith angles.

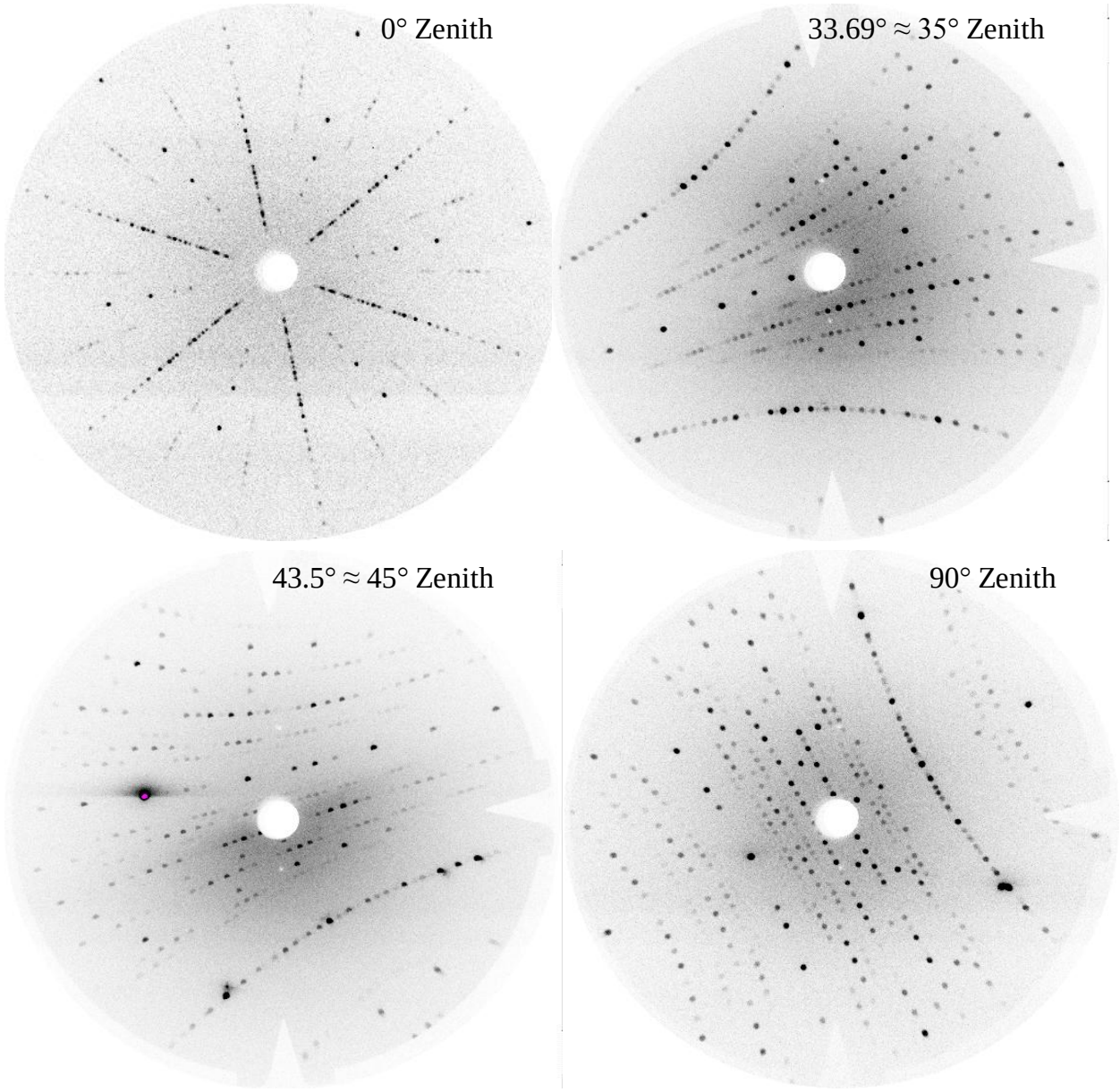

Figure 12: Zenith angle measurements using Laue diffraction.

4.3 Tip radii and area function calibration

For an ideal infinitely sharp tip, the projected contact area is a function of the contact depth. In the case of a Berkovich tip this contact area (*A*) is given by,

$$A = 3\sqrt{3}h_c^2 \tan^2 65.3 = 24.5h_c^2 \tag{23}$$

However, indenters used in practical testing generally have some tip defects (blunting etc.). The actual area functions for the Berkovich and the different pyramidal tips semi-angle (45°, 55°, 75°) were generated using fused silica specimen of known modulus (E_{FS}*=74.1 GPa*) and Poisson's ratio (*ν=0.17*) and the method outlined by Oliver and Pharr [39]. The area functions obtained are in the form of Equation 24 below,

$$A_c = a_0 h_c^2 + a_1 h_c + a_2 h_c^{1/2} + a_3 h_c^{1/4} + a_4 h_c^{1/8} + a_5 h_c^{1/16} \tag{24}$$

This area function is basically a polynomial which, when used with fused silica gives a modulus of 74.1 GPa in our case. The load (*P*) vs. displacement into surface (*h*) and modulus (*E) vs h* curves for fused silica specimen for the Berkovich indenter and the different pyramidal indenters used in this research are shown in Appendix II. Table 6 below shows the calculated constants for the area function for different pyramidal indenters.

Table 6: Area function constants for various pyramidal indenters.

	ψ	a_0	a_1	a_2	a_3	a_4
B45	45°	5.04684	852.222	-2371.1	-2226	959.551
B55	55°	10.8907	428.38	39.16	94.1505	171.301
B65	65°	20.7828	903.898	-1622.46	-616.799	515.673
B75	75°	65.8389	903.898	-1187.94	-2473.94	-589.92

The tip radii for the spherical indenters used in this research were determined using tungsten single crystal specimens of known modulus ($E=411\ GPa$) and Poisson's ratio ($\nu=0.28$). Assuming the *P-h* curve prior to the pop-in events to be completely elastic, the data was fit to the Hertz spherical contact solution to estimate the tip radius of the spherical indenters. Appendix III shows *P-h* curves along with Hertzian fit for the spherical indenters used in this study. Table 7 below summarizes the tip radii obtained for all spherical indenters.

Table 7: Tip radius calibration for spherical indenters.

Tip Designation	Manufacturer's Diameter (μm)	Radius from tungsten calibration (μm)
S9	1	0.36
S11	3	1.7
S10	10	7.5
S3	100	50

4.4 FEA analysis to determine flow properties

ABAQUS was used to perform finite element analysis using an axis-symmetric model with a rigid conical indenter. Previous research [64] has shown that a rigid conical indenter with different equivalent angles can be used to approximate the pyramidal indenters with different face angles. The method used by Shim et al. uses the measured hardness values from SEM or other methods to account for pile-up to obtain the stress-strain curve of the material. Figure 13 illustrates the method used in the FEA simulations to obtain the flow properties from the indentation measurements.

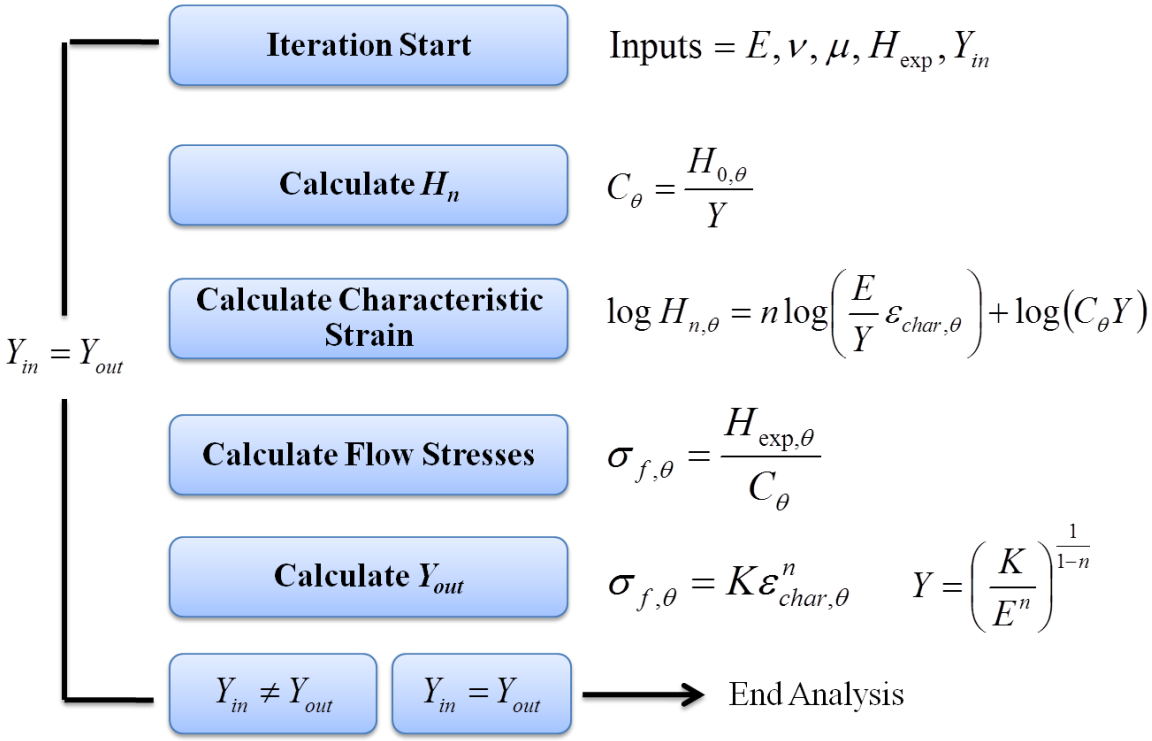

Figure 13: Flow Chart for FEA analysis to determine flow properties [85].

CHAPTER 5. Indentation of SiC-6H single crystal

5.1 Spherical Indentation on SiC-6H single crystal

5.1.1 Cree SiC-6H

Figure 14 below shows *P-h* curves for different spherical indenters in the <0001> and <01-10> direction on Cree SiC-6H single crystal specimens. The *P-h* curves for the <0001> and the <01-10> direction indentation experiments show three distinct regions: the purely elastic portion, the discrete displacement bursts or "pop-ins" and an elastic plastic portion after pop-in. The critical load at which pop-in occurs varies from test to test. Discrete displacement bursts or "pop-ins" are observed for smaller diameter spherical indenters, while for larger diameter indenters the *P-h* curve is completely elastic. In a defect free crystalline material the local resolved shear stress values are close to the theoretical strength of a material and therefore in a defect free material the loads at which pop-in events occur should be the same. The variations of the pop-in loads may be due to a distribution of defects near the contact area. Hertzian contact Figure 15 and Figure 16 show the maximum shear stress and the maximum tensile stress beneath an indenter for both orientations of SiC-6H the <0001> and the <01-10>. Analysis of the *P-h* data shows that the SiC-6H <0001> sample has a higher minimum pop-in load than the SiC-6H <01-10> sample for all the spherical indenters. The load-displacement response for both the SiC-6H samples (<0001> and <01-10>) for indentation with a 50 μm radius sphere is completely elastic. Using Hertzian analysis and the calibrated radius of the spherical indenter the modulus of the SiC-6H in the <0001> and the <01-10> orientations can be calculated. The calculated modulus is 510 ± 4.5 GPa and 488 ± 3.8 GPa in the <0001> and <01-10> orientations respectively, for spherical indentation with a 50 μm radius sphere.

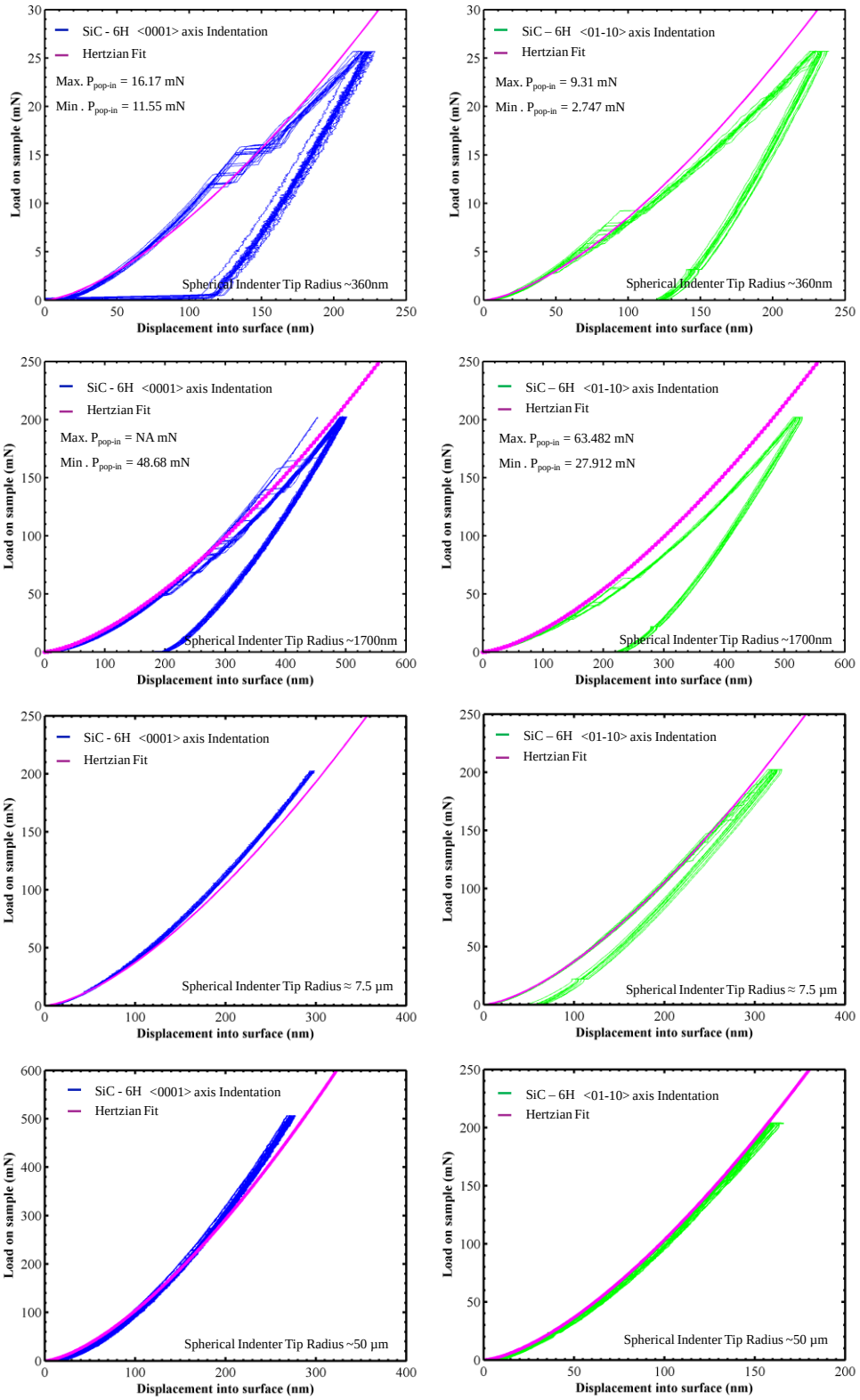

Figure 14: *P-h* curves for spherical indentation on Cree SiC-6H in <0001> and <01-10> directions.

Figure 15 below shows the shear stress beneath the spherical indenter for indentation in the <0001> and <01-10> directions. It can be seen that, the maximum shear stress at pop-in loads for the larger spheres are lower than those for the smaller spheres. This observation is consistent with previous researchers who reported differences in τ_{max} due to nanoindentation size effects [86, 87]. This difference can be explained by the fact that the number of dislocations or defects in the stressed volume increases with the increase in the indenter size. It is therefore possible that for small indenters, the volume of the stressed material beneath the indenter is dislocation free which requires dislocation nucleation to occur at the theoretical stress resulting in pop-ins. An increase in the indenter radius or the stressed volume increases the possibility of encountering nearby pre-existing dislocations. The motion of these pre-existing dislocations assists the onset of plasticity resulting in lower maximum shear stresses for larger indenters. We can conclude that plasticity tends to be initiated by pre-existing dislocations rather than nucleation of dislocations when sufficiently large volumes are stressed. Umeno et al. [74] using DFT simulations found the shear strength of single crystal SiC in the <0001> direction to be ~ 30 GPa. Figure 16 shows the maximum tensile stress beneath the spherical indenter for indentation in the <0001> and <01-10> orientations. Since the maximum tensile stress is much lower than the theoretical, thus, no cracking is expected, as observed.

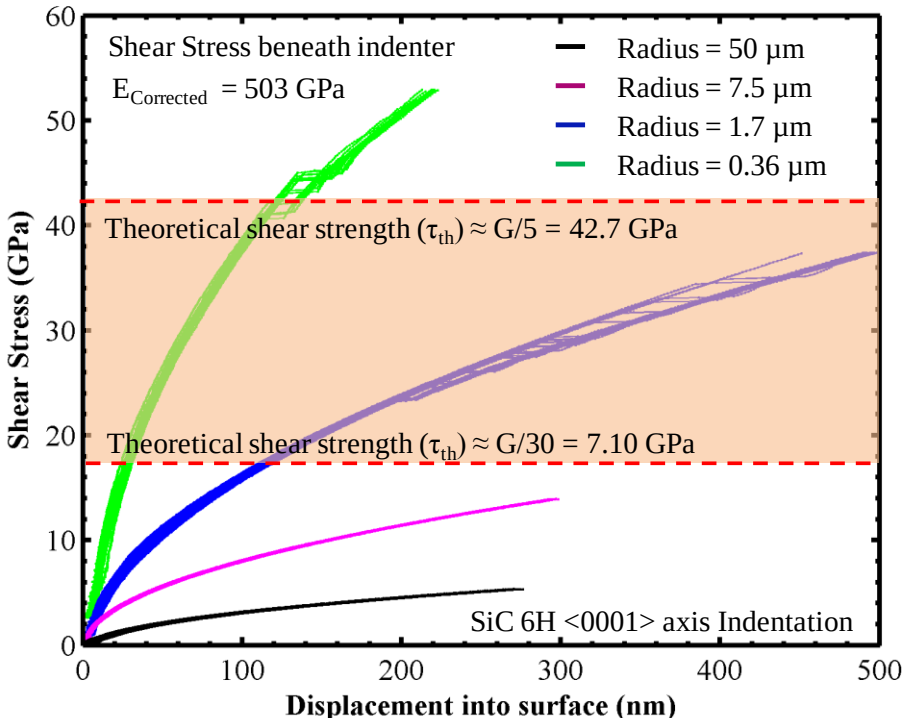

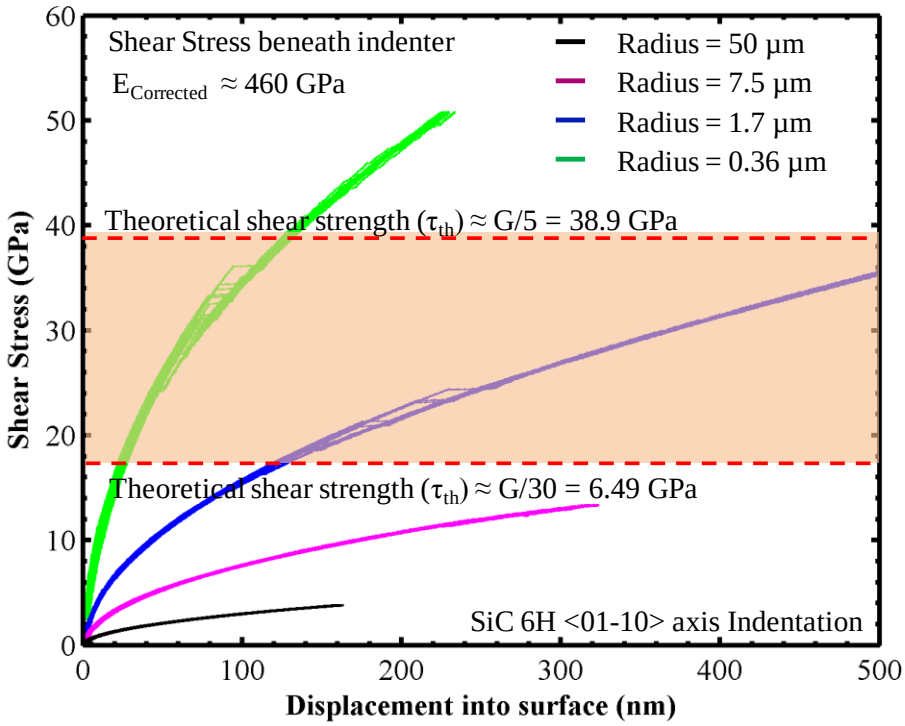

Figure 15: Maximum shear stress beneath the indenter for Cree SiC-6H <0001> and <01-10> axis spherical indentation.

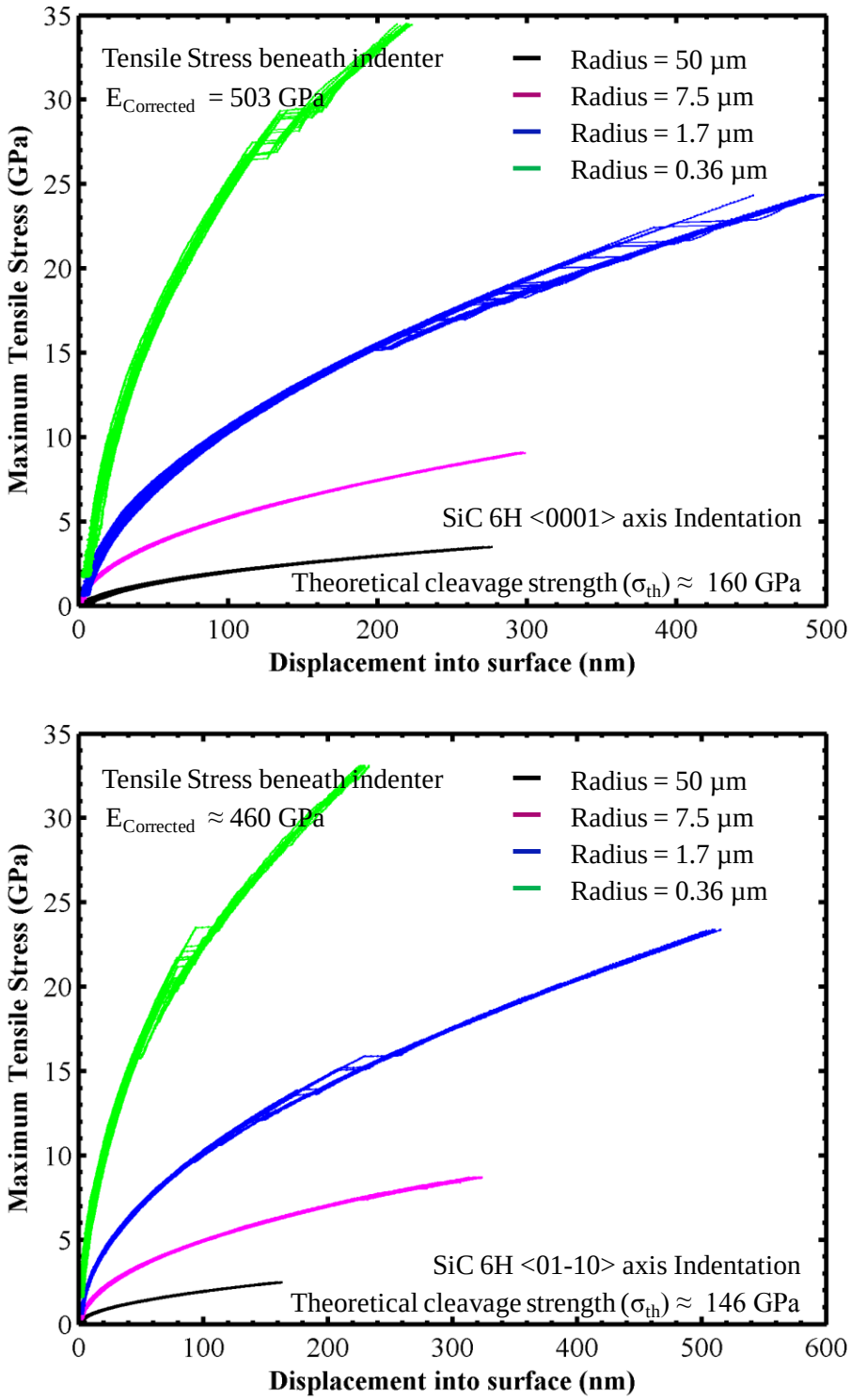

Figure 16: Maximum tensile stress beneath the indenter for Cree SiC-6H <0001> and <01-10> axis spherical indentation.

5.2 Berkovich Indentation on SiC-6H single crystal

5.2.1 Cree SiC-6H

Figure 17, 18, and 19 below shows the *P-h*, *Modulus (E)-h* and *Hardness (H)-h* curves respectively, for SiC-6H single crystal Cree samples. The figures below show averaged data from at least 20 indents. The hardness and the modulus data is corrected for pile-up behavior by using SEM and interference microscope images of the indents to determine the actual contact area. A representative image used in the pile-up corrections is shown in Appendix I. It can be seen from the Figure 18 that the SiC-6H <0001> sample shows an indentation size effect on the hardness. This is probably due to pop-in behavior at low loads during the Berkovich indentation experiments on SiC-6H <0001> samples. The SiC-6H <01-10> samples do not show any pop-in behavior during Berkovich indentation. The results are summarized in Table 8 below. The hardness and modulus of SiC-6H in the <0001> direction are higher than in the <01-10> direction. The difference in modulus and hardness between the <0001> and the <01-10> directions is ~7% and <0.5% respectively indicating that SiC-6H has only a small elastic and plastic anisotropy.

Table 8: Modulus and hardness of Cree SiC-6H measured by Berkovich indentation.

Sample	**Berkovich Indentation**			
	E_{OP}	H_{OP}	E_{Corr}	H_{Corr}
	(GPa)	**(GPa)**	**(GPa)**	**(GPa)**
SiC-6H <0001>	549.66 ± 20.63	40.97 ± 1.21	503.13 ± 28.19	32.26 ± 5.01
SiC-6H <01-10>	513.71 ± 19.84	39.13 ± 0.79	461.94 ± 22.49	30.81 ± 2.1

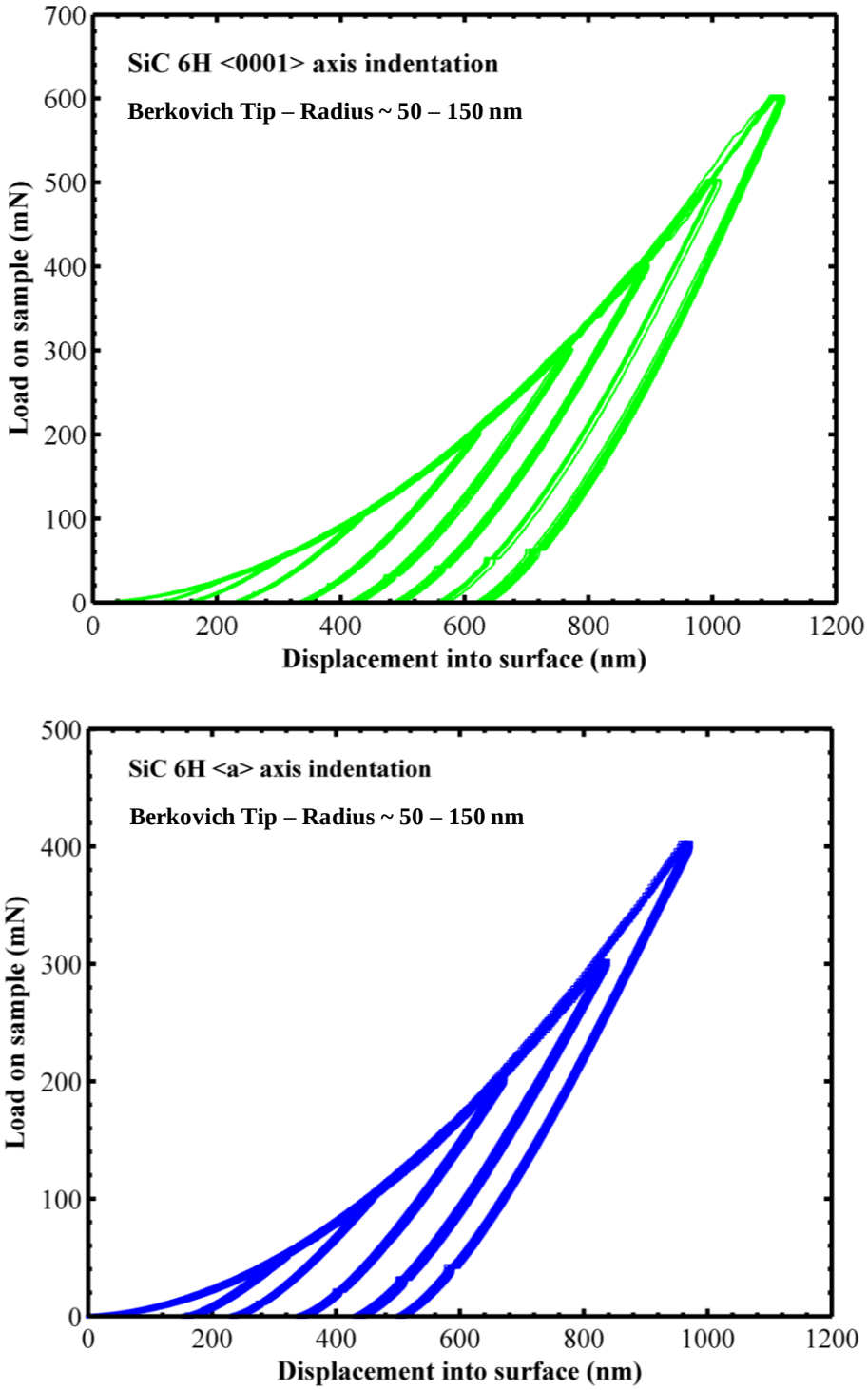

Figure 17: *P-h* loading-unloading curves for Berkovich indentation of Cree SiC-6H samples.

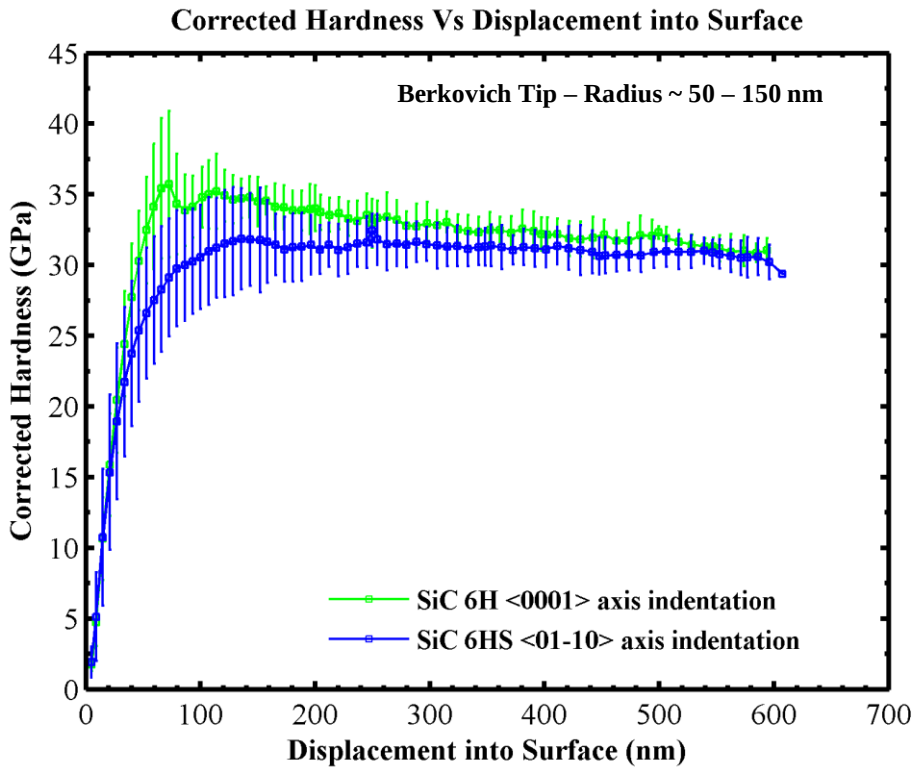

Figure 18: *H-h* curves for Berkovich indentation of Cree SiC-6H samples.

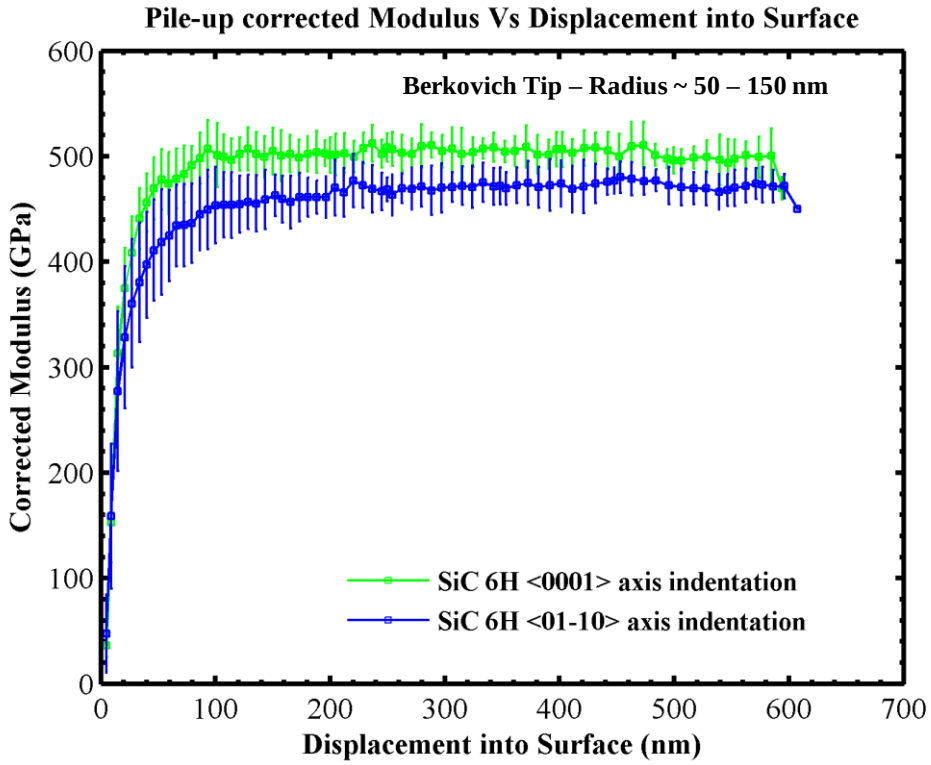

Figure 19: *E-h* curves for Berkovich indentation of Cree SiC-6H samples.

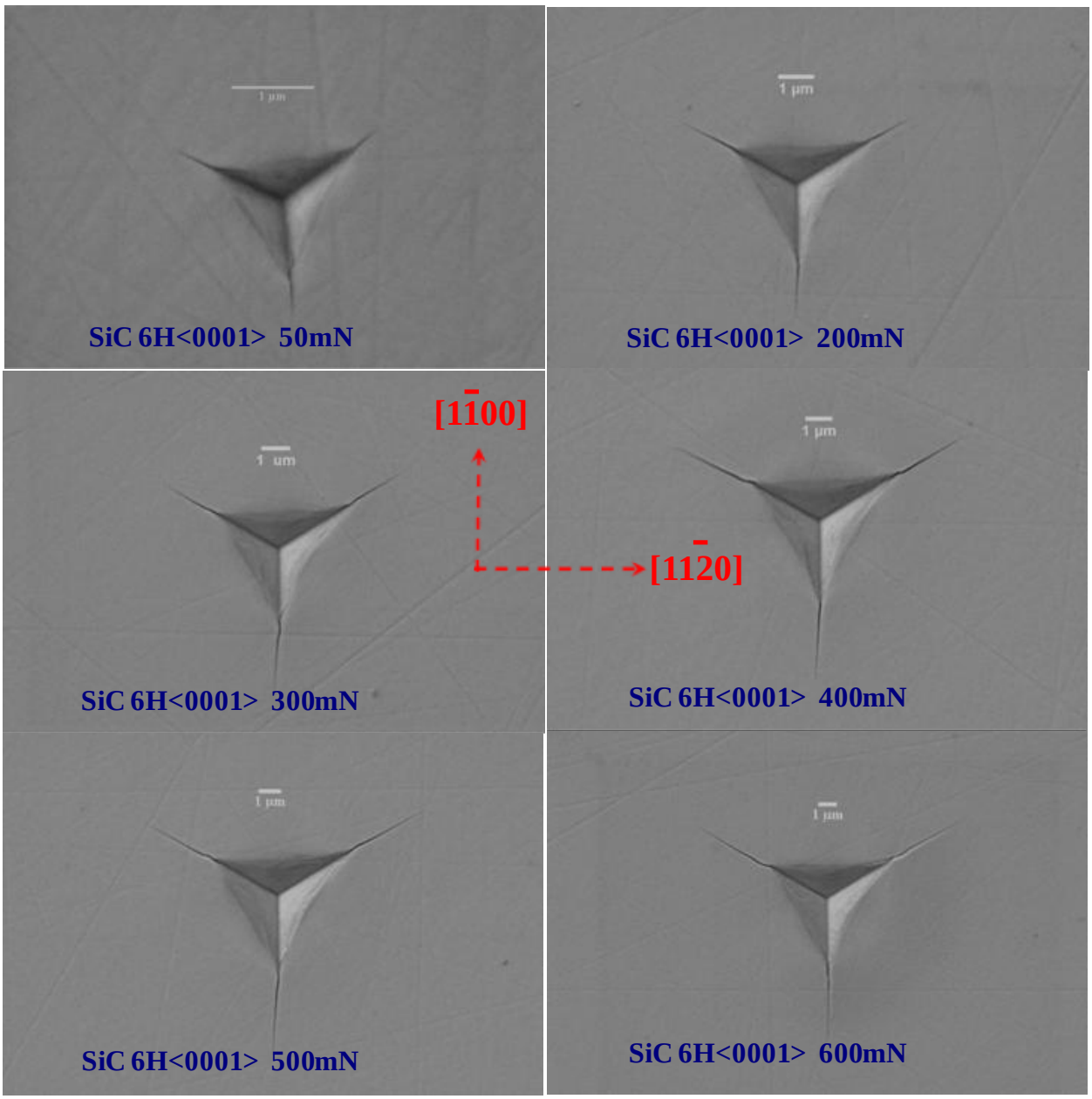

Figure 20: Representative SEM images of Berkovich indentation of Cree SiC-6H <0001>.

The hardness values are similar to those obtained in previous research by Shaffer et al. [71], who obtained a hardness of around 30 GPa in the c-axis and around 26 GPa in the a-axis using a Knoop indenter, and by Henshall et al. [74] who obtained hardness values of around 30 GPa in the <0001> and 28 GPa in the <1-100> direction using a Berkovich indenter. Figure 20

and Figure 21 show SEM images of Berkovich indentations in SiC-6H single crystal samples. There is a difference in the cracking pattern between the two orientations. When indented in the <0001> direction, cracks originate at the tip, whereas for <01-10> some of the cracks originate from the side of the indent for reasons related to anisotropy in cleavage cracking.

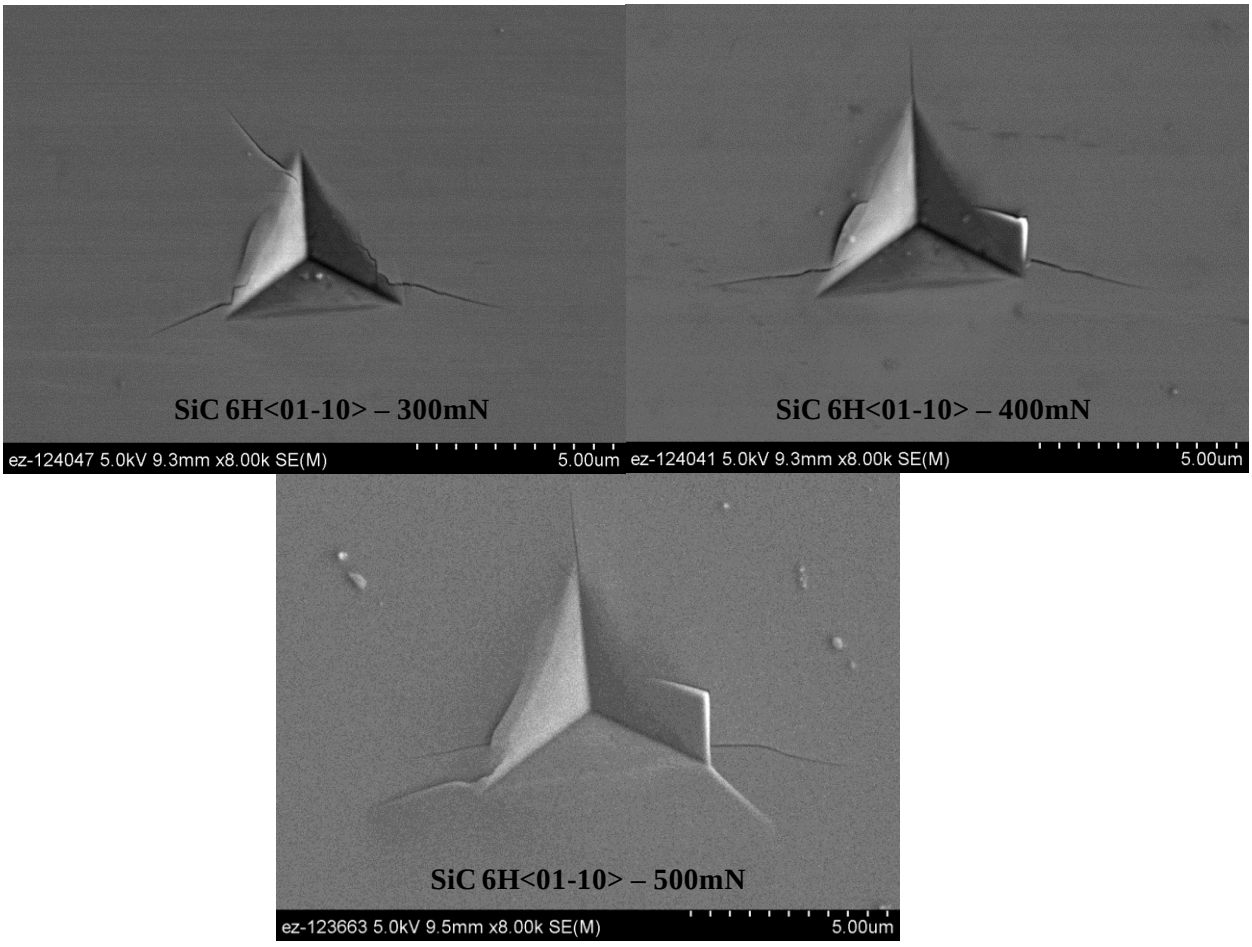

Figure 21: Representative SEM images for Berkovich indentation in Cree SiC-6H <01-10>.

5.2.2 Nitride Crystals (NC) SiC-6H

Figure 22 and 23 below show the results from Berkovich indentation experiments on NC SiC-6H single crystal samples with different zenith angles. The results shown are an average of

at least 20 indents. It follows from load displacement curves shown in Figure 22, that the 44° zenith angle SiC sample has the lowest modulus. The results are summarized in Table 9. The 0° zenith (c-axis) indentation has the highest modulus and hardness values while the 44° zenith angle orientation has the lowest. The difference in the highest and the lowest modulus is about 8%, and the different in the highest and lowest modulus is also about 8%. This result indicates that the elastic and plastic anisotropies in SiC are relatively small.

Table 9: Summary results of Berkovich indentation on NC SiC-6H in different orientations.

Sample	Zenith Angle (degrees)	Berkovich Indentation			
		E_{OP} (GPa)	H_{OP} (GPa)	$\boldsymbol{E_{Corr}}$ (GPa)	$\boldsymbol{H_{corr}}$ (GPa)
NC SiC 6H	0	497.2 ± 9.4	36.8 ± 1	460.18 ± 8.4	31.55 ± 0.7
NC SiC 6H	35	471.9 ± 5.7	35.3 ± 0.8	444.33 ± 8.7	30.26 ± 1.1
NC SiC 6H	44	461.2 ± 6.0	31.6 ± 0.6	439.04 ± 7.2	27.09 ± 0.5
NC SiC 6H	90	468.3 ± 3.8	32.1 ± 0.4	448.82 ± 6.1	27.52 ± 0.7

It is also interesting to note that no pop-in's were observed in the <0001> direction or in any other zenith angle for Nitride Crystals Inc. SiC samples. The hardness measurements show similar trends to those noticed in the Cree SiC-6H single crystal samples.

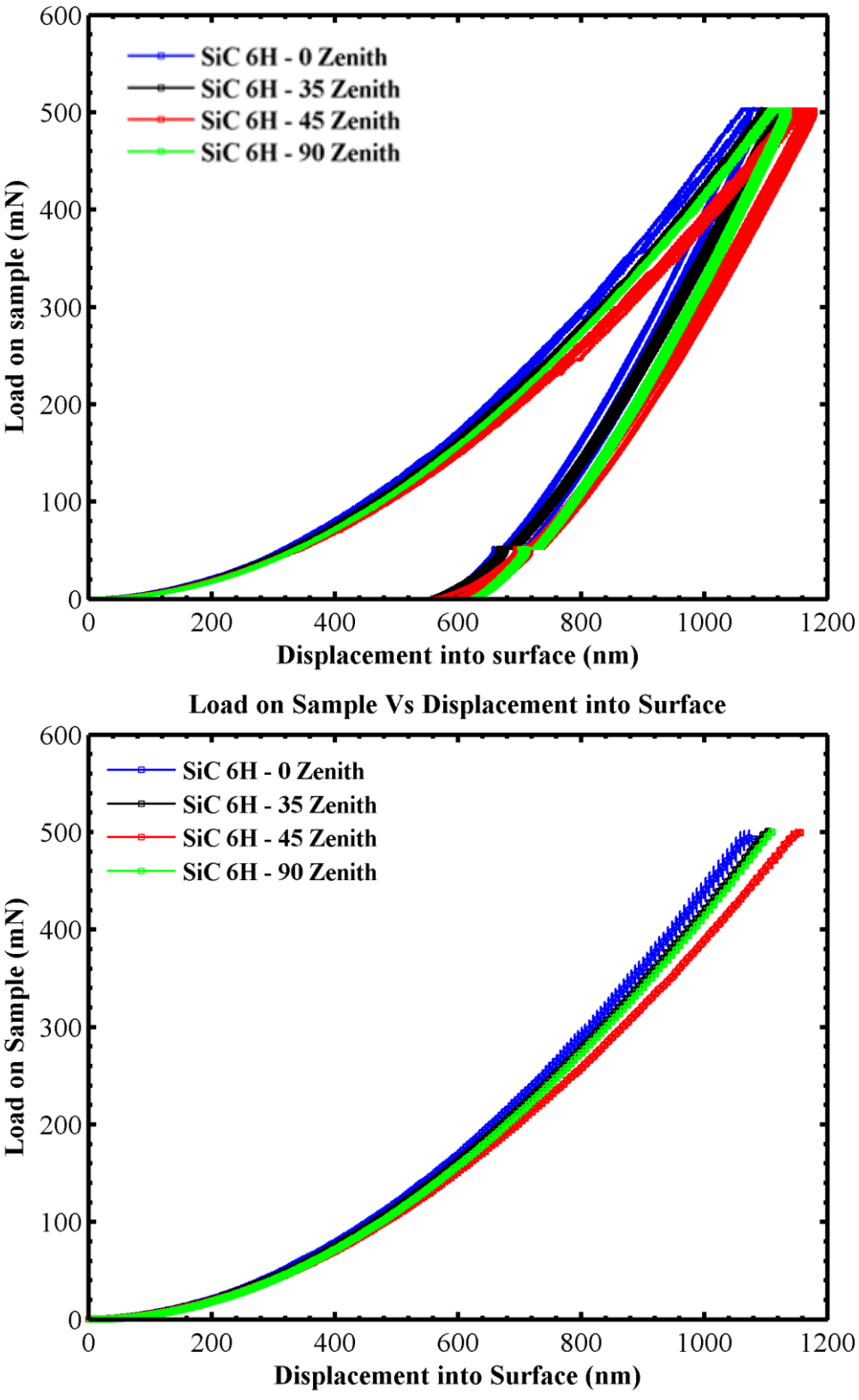

Figure 22: *P-h* curves for NC SiC-6H samples for different zenith angles.

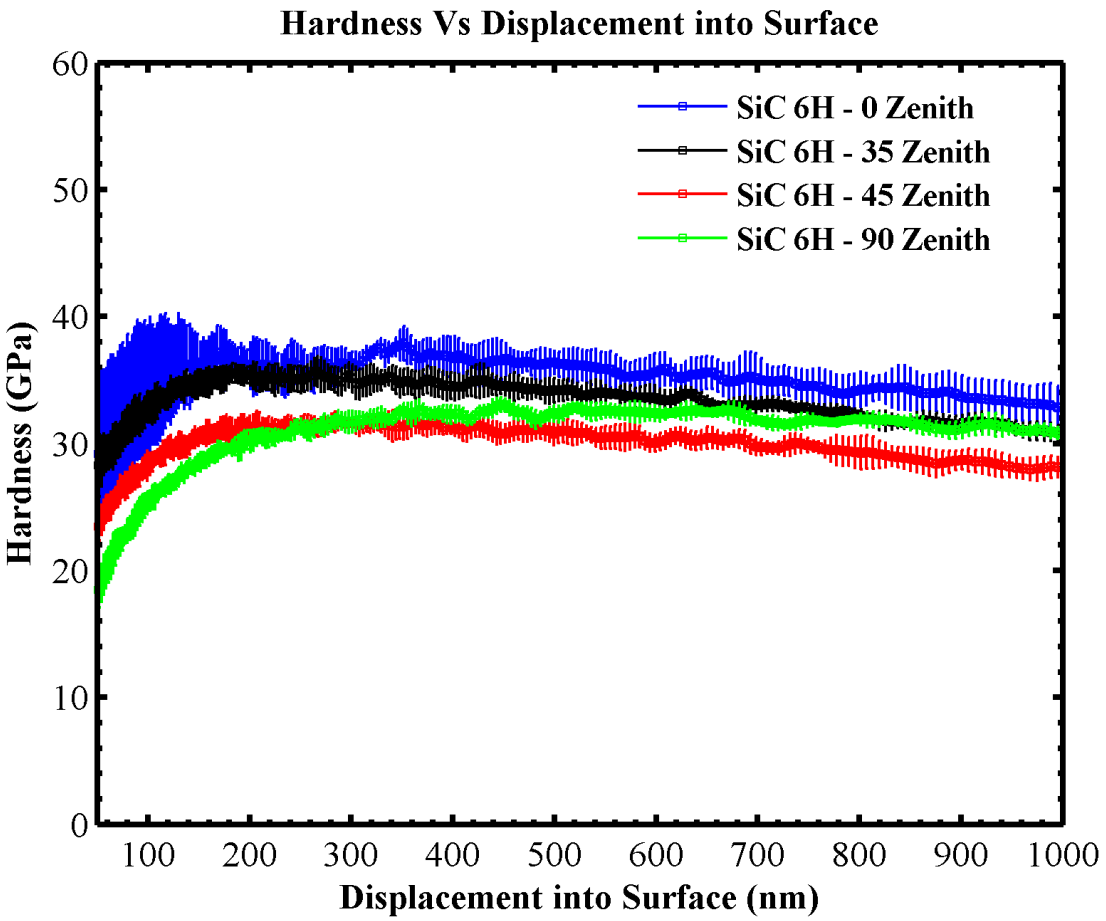

Figure 23: *H-h* curves for NC SiC-6H single crystal samples with different zenith angles.

5.3 Anisotropic elastic analysis of SiC-6H

The HCP crystal structure of SiC is transversely isotropic; therefore the indentation moduli will only depend on the zenith angle, i.e the angle between the indentation direction and the c-axis. Using the method described by Gao et al. [83] and Li et al., [84] indentation effective moduli were calculated using single crystal elastic constants (C_{11} = 501 ± 4 GPa, C_{33} = 553 ± 4 GPa, C_{44} = 163 ± 4 GPa, C_{12} = 111 ± 5 GPa, and C_{13} = 52 ± 9 GPa) measured using Brillouin scattering experiments [5, 8, 9]. Figure 24 below the effective indentation moduli and the

modulus (calculated using a 0.18 Poisson's ratio) as a function of zenith angle. The difference in the largest indentation moduli (0° zenith – <0001> axis indentation) and the smallest indentation moduli (45° zenith) is very small about ~7%. Figure 25 shows the indentation modulus E_{eff} and E calculated using elastic contact prediction and the experimental values obtained using spherical and Berkovich indentation in different orientations for SiC-6H single crystal samples. The difference in the values between two SiC-6H materials can be attributed to dopant levels in the samples, the type of dopants and the growth processes used for single crystal growth (temperature gradients etc.). The difference between the values obtained from anisotropic elastic contact analysis and the experimental values can be attributed to assumption that for anisotropic elastic contact analysis the material is a perfect crystal whereas the actual material has dopants and other defects, there are errors in the measurements of elastic constants in Brillouin scattering experiments (usually about 10%) and there are some errors in the nanoindentation experiments.

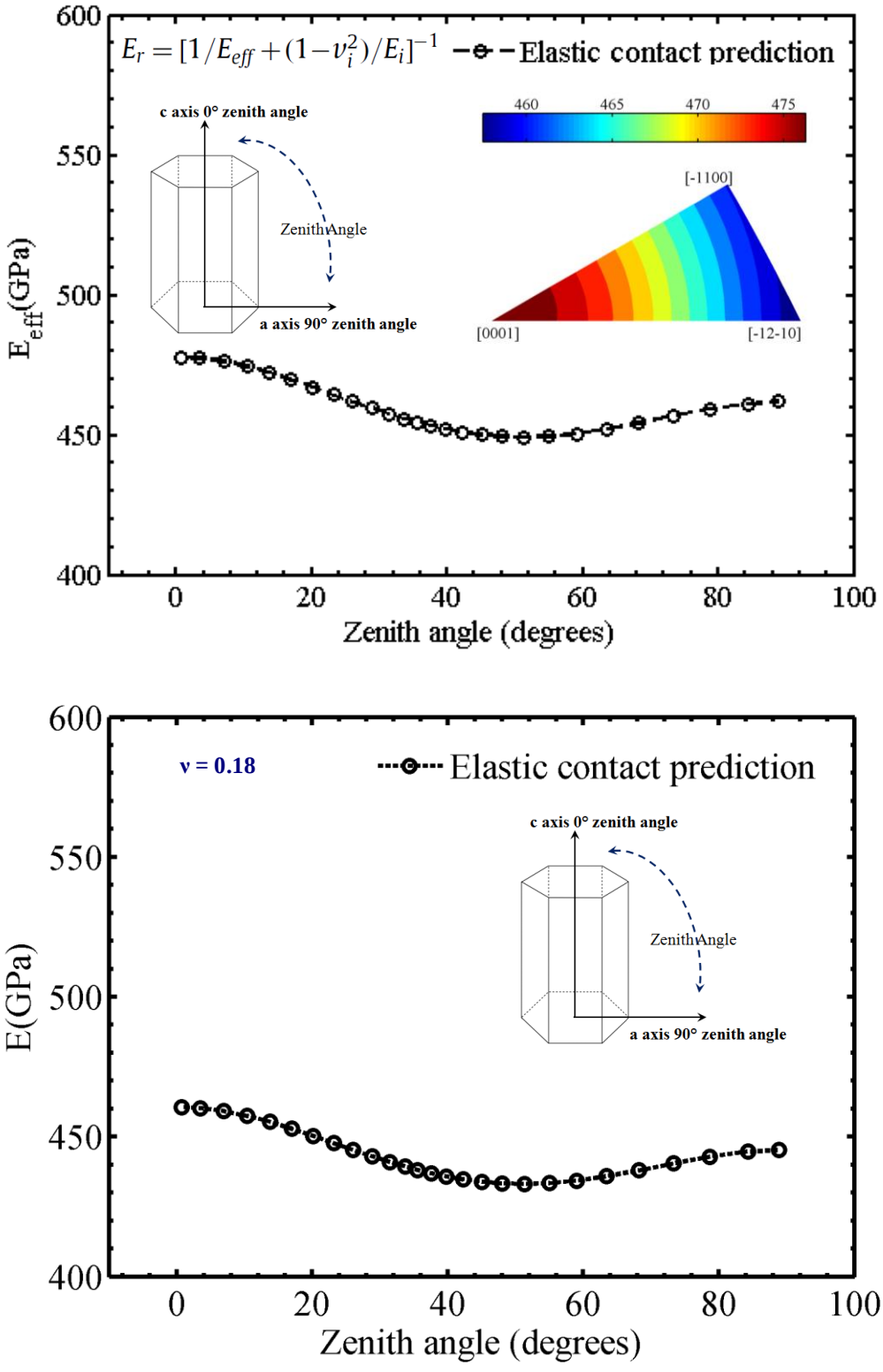

Figure 24: E_{eff} and E vs zenith angle calculated using elastic constants.

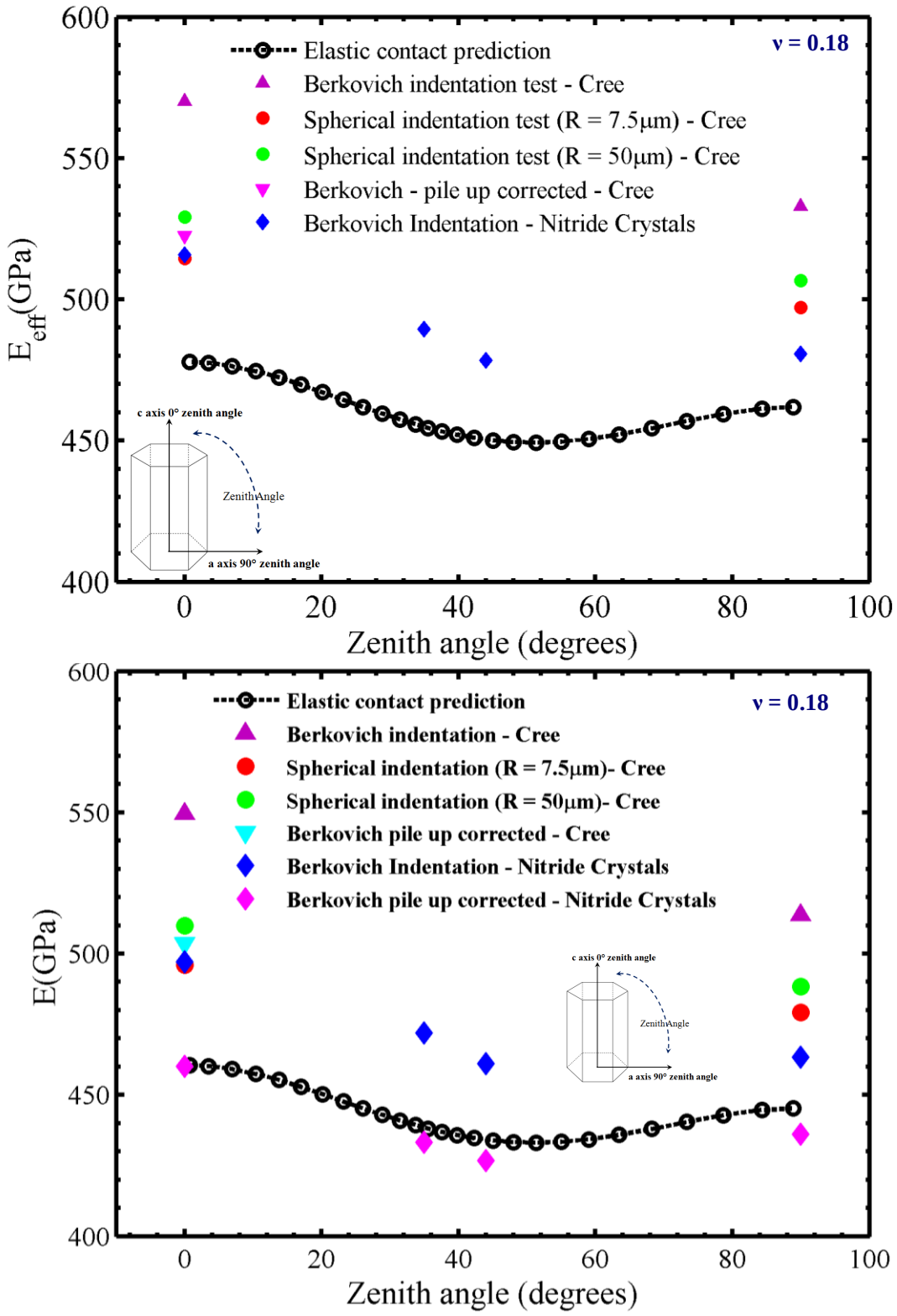

Figure 25: Comparison of E_{eff} and E vs zenith angle between experiments and elastic contact analysis.

5.4 Hardness anisotropy in SiC-6H single crystals

Figure 26 shows the difference in Oliver-Pharr measured hardness and the corrected hardness (pile-up area corrections) for Cree and Nitride Crystals SiC-6H single crystals as a function of zenith angle. The difference between the maximum (0° Zenith) and the minimum hardness (45° Zenith) is about 10%. The difference in the hardness values is consistent with the results obtained by Shaffer et al. [71] who obtained hardness values of 30 GPa in the <0001> direction and approximately 25 and 26 GPa respectively when indenting on the (10-10) and the (1-120) faces respectively.

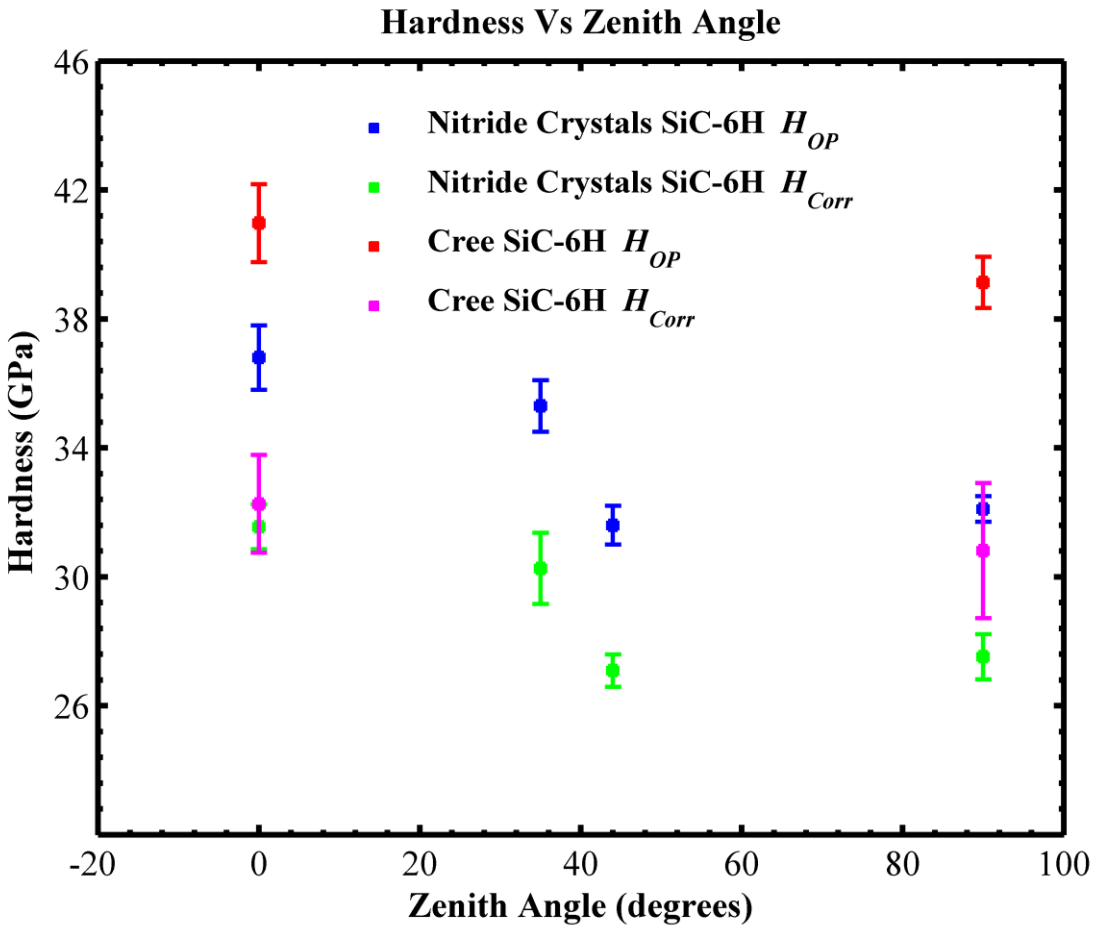

Figure 26: Comparison of hardness vs zenith angle for Cree and Nitride Crystals SiC.

CONCLUSIONS

In this chapter we have studied the elastic and plastic anisotropy in single crystal SiC-6H samples using Berkovich and spherical indenters. The nanoindentation results on different orientations of SiC-6H show that the trends predicted by the theoretical analysis are born out in experimental measurements. Although there are differences in the values of hardness and modulus in a specific orientation between SiC single crystals samples from the two different vendors the trend is the same. The results indicate that the elastic and plastic anisotropies in SiC-6H in different orientations is relatively small. The experimental results obtained in this research show similar trends as in previous literature results which were primarily done with a Knoop indenter. The important conclusions that can be drawn from this work are as follows:

1. The c-axis has the highest modulus and hardness compared to other directions.
2. These results show that there is ~10% difference in the measured corrected modulus ~7% difference in the corrected hardness between <0001> and <01-10> axis indentation of Cree SiC-6H single crystal samples.
3. The maximum shear stress at pop-in approaches the upper limit of theoretical shear strength (~G/5) in the <0001> direction indicating nucleation of dislocations as the deformation mechanism for the 1 μm diameter spherical indenter.

CHAPTER 6. Indentation cracking in Cree SiC-6H

6.1 Orientation effects in Cree SiC-6H single crystals during indentation in the <0001> direction

The Cree SiC-6H single crystal samples were indented with a Berkovich indenter in the <0001> direction by rotating them in the <a> plane to study indenter orientation effects if any in SiC-6H. Figure 27 shows representative images in four different rotations around the <0001> axis in the <a> plane. The yellow lines in the images show the path of the cracks. It can be seen from the images that the crack propagation in the single crystal generally takes place parallel to the nearest cleavage plane. There is very little difference (<1% between the maximum and the minimum) in the measured hardness, modulus and the crack lengths in these indentation experiments indicating that SiC-6H does not exhibit significant orientation effects during Berkovich indentation experiments in the <0001> direction. Table 10 shows the average hardness, modulus, and c/a ratios for different rotation angles.

Table 10: Hardness, modulus and c/a ratios for Berkovich indentation along c–axis in different orientations around c axis.

	E_{OP} (GPa)	H_{OP} (GPa)	c/a @ 500mN
R1 (θ ≈ 19°)	543.813 ± 27.137	49.701 ± 3.678	1.972 ± 0.069
R2 (θ ≈ 12°)	546.585 ± 29.299	49.641 ± 3.143	1.964 ± 0.098
R3 (θ ≈ 5°)	545.640 ± 24.467	49.086 ± 2.751	2.033 ± 0.078
R4 (θ ≈ 7°)	542.770 ± 21.443	48.852 ± 2.491	1.989 ± 0.139

These observations agree with observations made by Shaffer et al. [71] who also noticed that there was no significant difference in the hardness values when using the Knoop indenter in the <0001> axis with the long axis of the indenter parallel to the (10-10) and (11-20) faces.

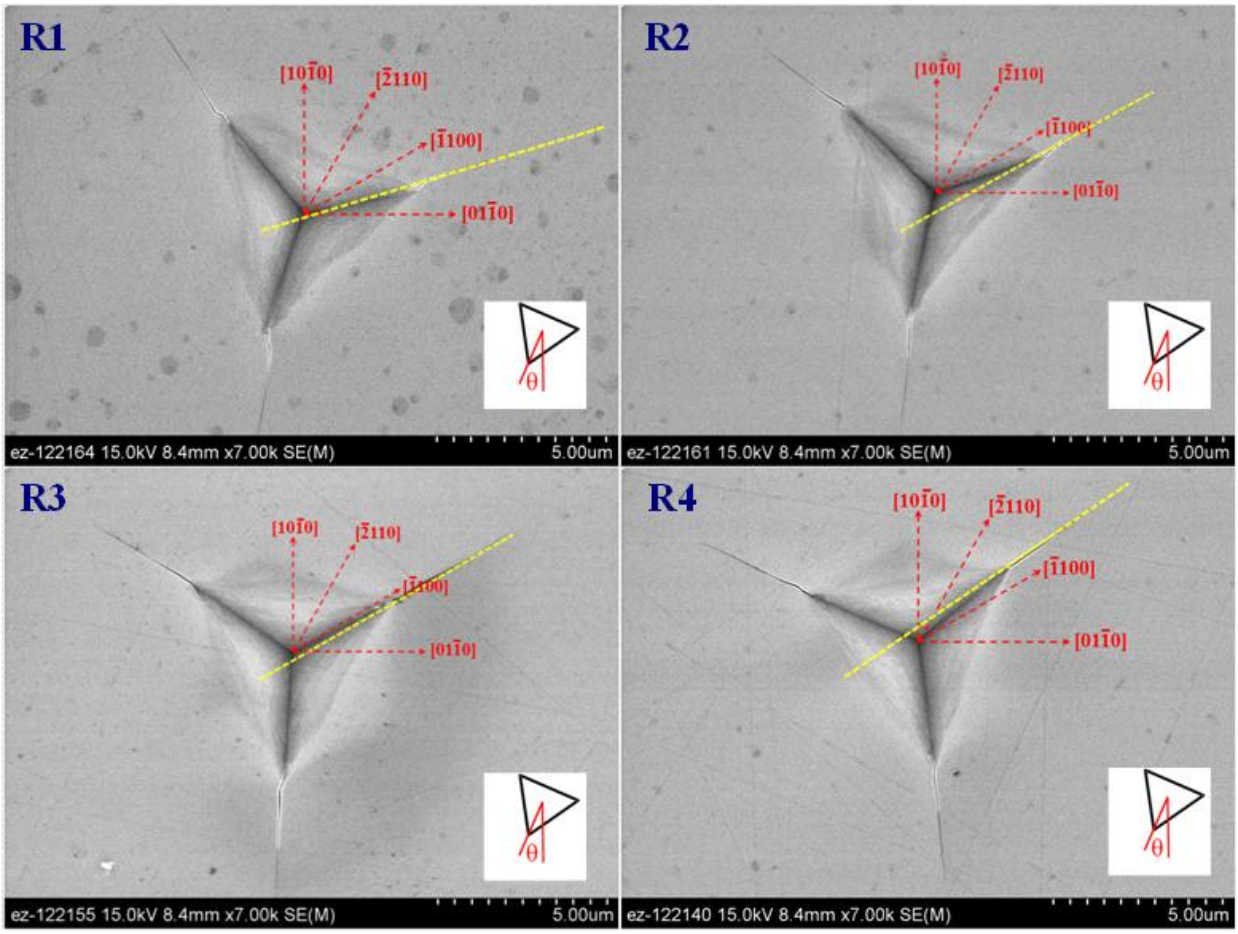

Figure 27: Representative images of Berkovich Indentations in Cree SiC-6H in the <0001> direction with different rotations around the <0001> axis.

6.2 Influence of indenter angle (centerline to face) on cracking in Cree SiC-6H <0001>

Pyramidal tips with different centerline to face angles were used to study the effect of the indenter angle on the cracking of SiC-6H <0001>. Figure 28 shows representative SEM images of indents using a 55° degree pyramidal indenter on Cree SiC-6H in the <0001> direction.

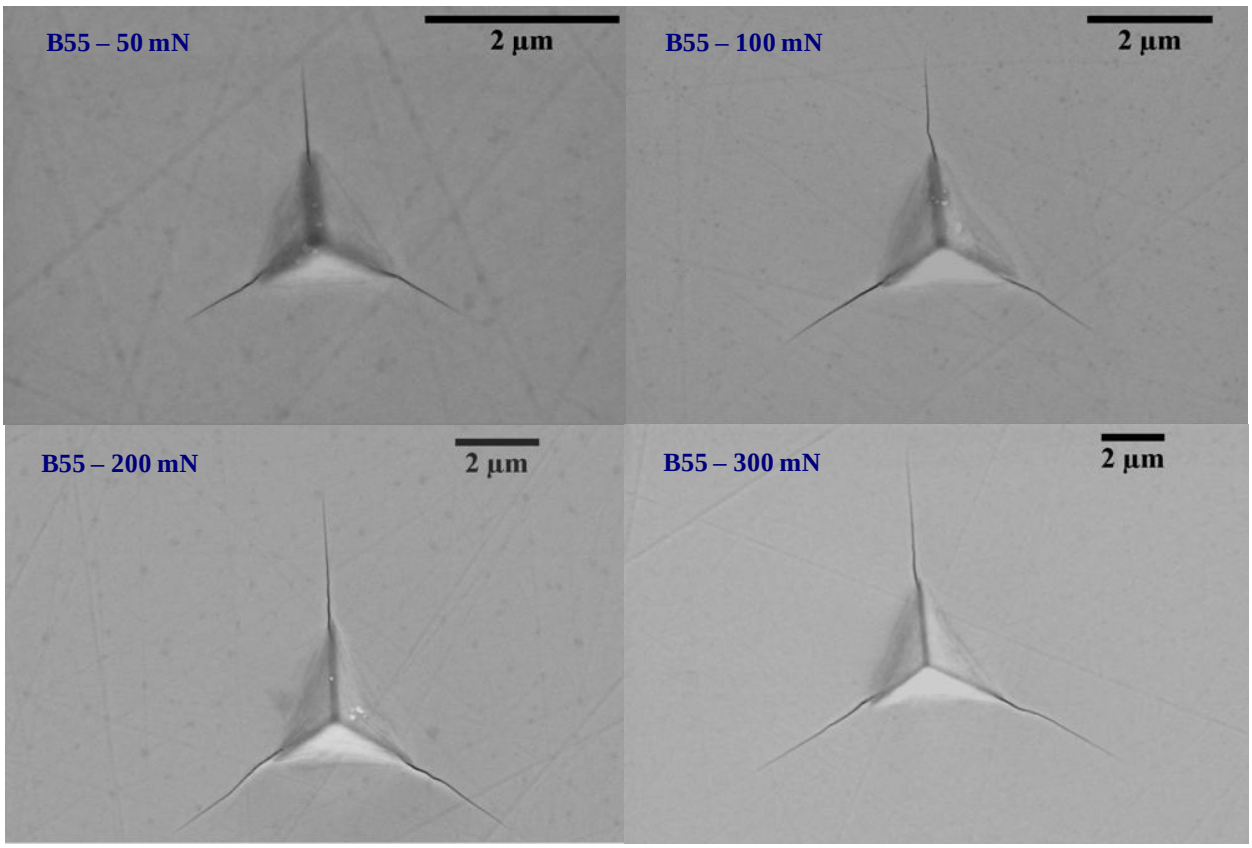

Figure 28: Representative SEM images of indentation with a 55° pyramidal tip in Cree SiC-6H <0001>.

Figure 29 shows representative images of indentation using a 65° pyramidal indenter (Berkovich) at high loads (1N or greater). Figure 20 shows representative images of Berkovich indentation in Cree SiC-6H in the <0001> direction at peak loads less than 500 mN. Figure 30 shows representative SEM images of indentations in Cree SiC-6H <0001> using a 75° degree pyramidal indenter at various peak loads.

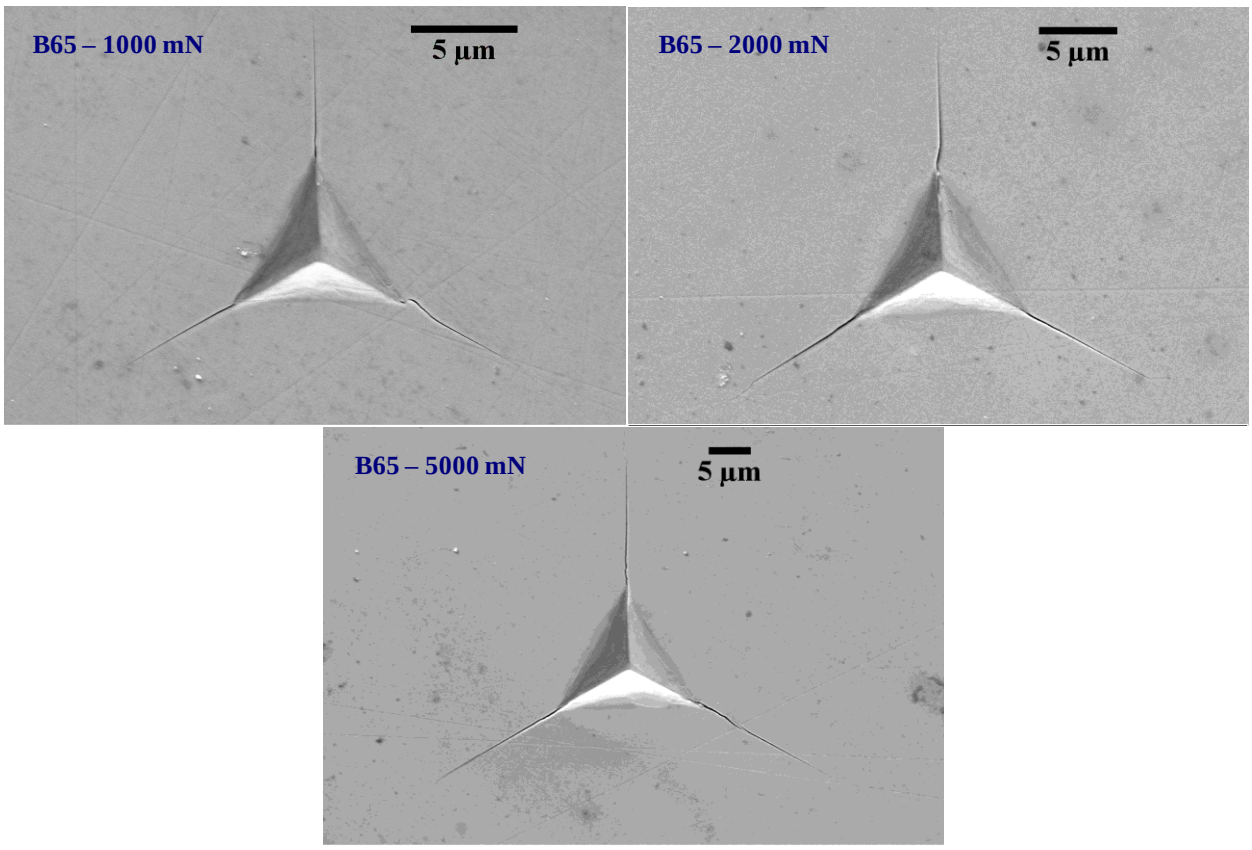

Figure 29: Representative SEM images of indentations with 65° (Berkovich) tip in Cree SiC-6H<0001> at high loads.

The sharper the indenter the more strain it will generate in a material for a given peak load. A 55° pyramidal indenter therefore has a greater displacement into surface than a 75° degree indenter at a particular peak load. At low loads for brittle ceramics previous literature has shown that, it is expected that there will be median radial cracking at low loads which Palmquist cracking will be at higher loads. Previous research [26, 58] has shown that a sharper indenter, which induces more strain in the material, may be able to change the cracking mode from median radial cracking mode to Palmquist cracking mode.

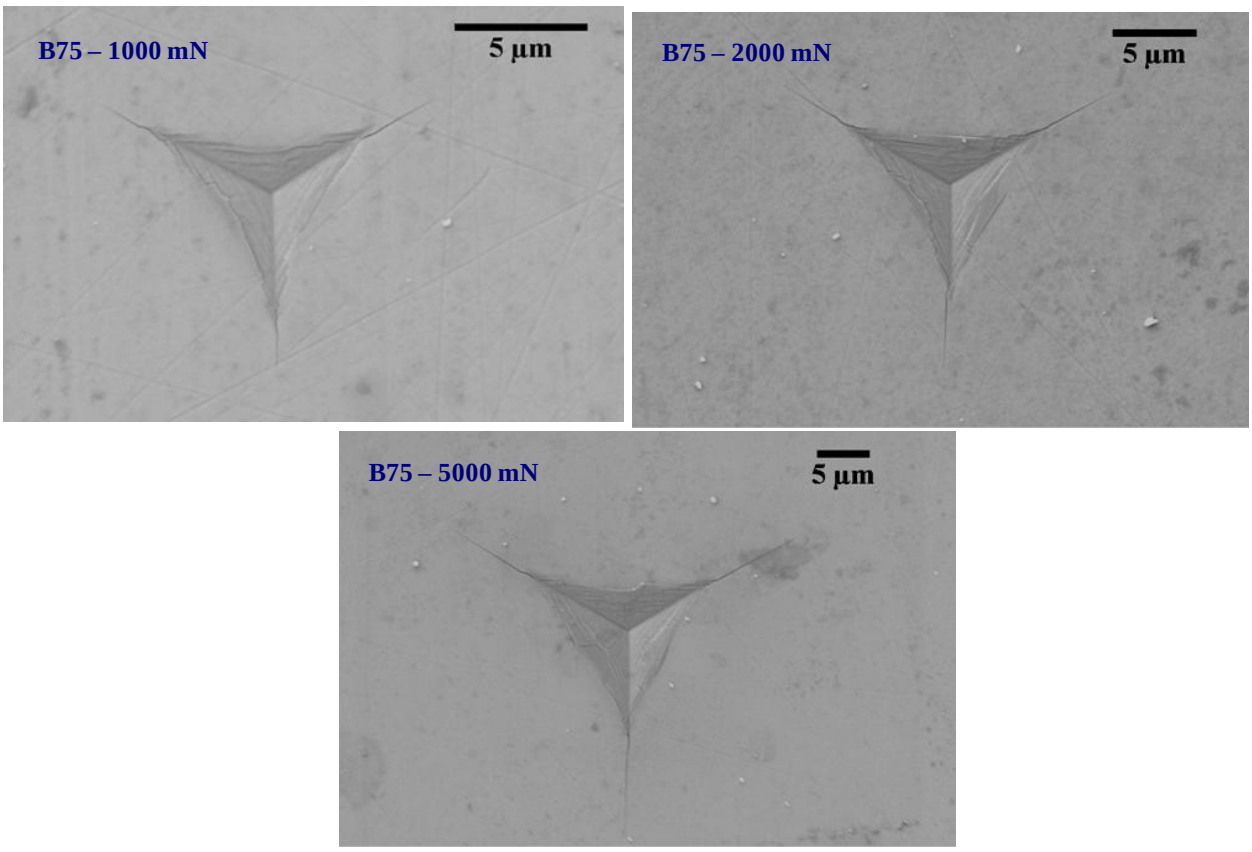

Figure 30: Representative SEM images of indentations with 75° tip in Cree SiC-6H <0001> at high loads.

It can be seen from Figure 28, Figure 29, and Figure 30 that the he surface cracking patterns for all the 55°, 65° and 75° pyramidal indenters appear to be similar. However there might be a difference in the subsurface cracking between the sharper (55°) and the more blunt (75°) indenters. It can also be seen from SEM images that at a particular peak load the crack lengths for a shaper indenter are much larger than a blunt indenter.

6.3 Fracture toughness measurement in SiC-6H<0001>

Figure 31 shows the variation of c/a and c/l values for various loads for Berkovich indentation in the Cree SiC-6H<0001> samples. The results show that the c/a ratios are not constant indicating that the cracking behavior of the Cree SiC-6H<0001> is not geometrically self similar. Figure 32 shows the c/a values with different peak loads for a 55°, 65° and 75° degree pyramidal indenter. The c/a ratio increases with an increase in peak load, indicating that the indentation in SiC-6H <0001> is not geometrically self similar.

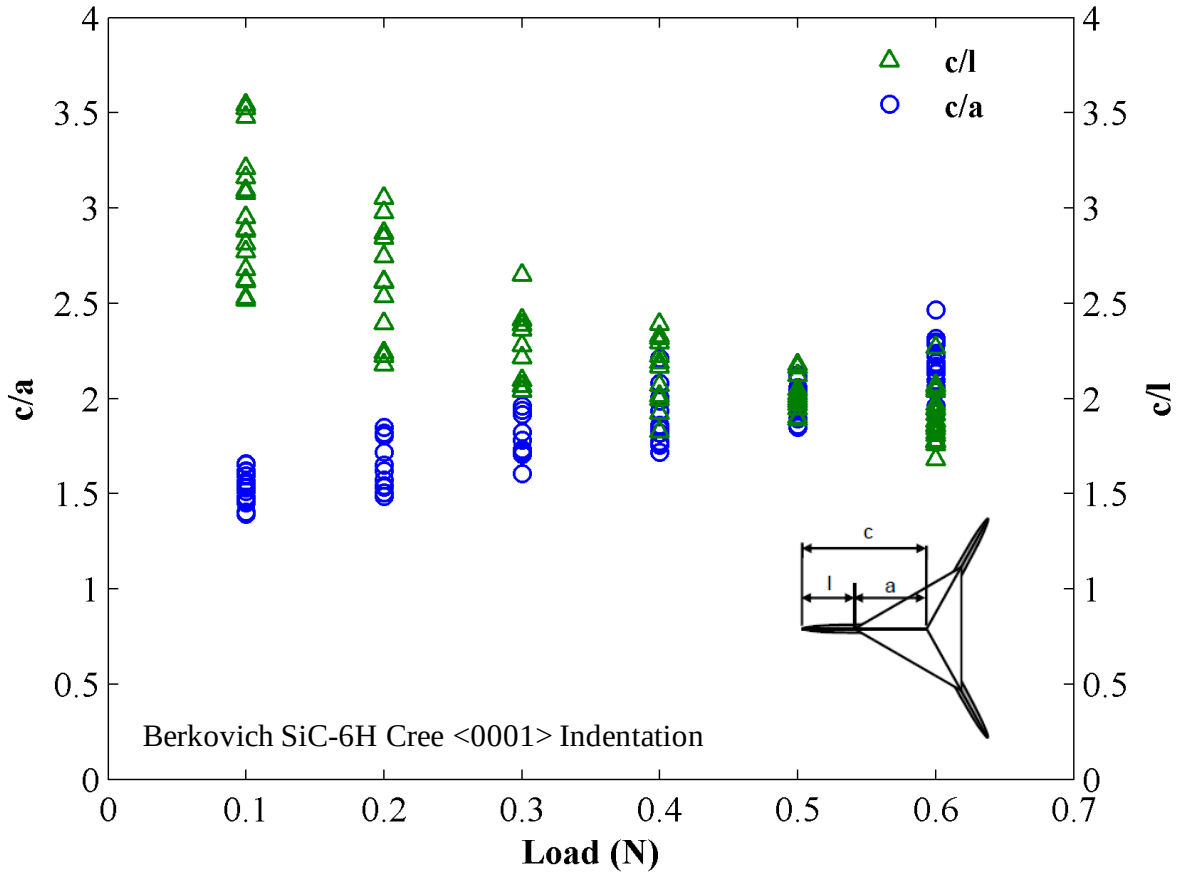

Figure 31: *P* vs *c/a* and *c/l* for Berkovich indentation of Cree SiC-6H <0001>.

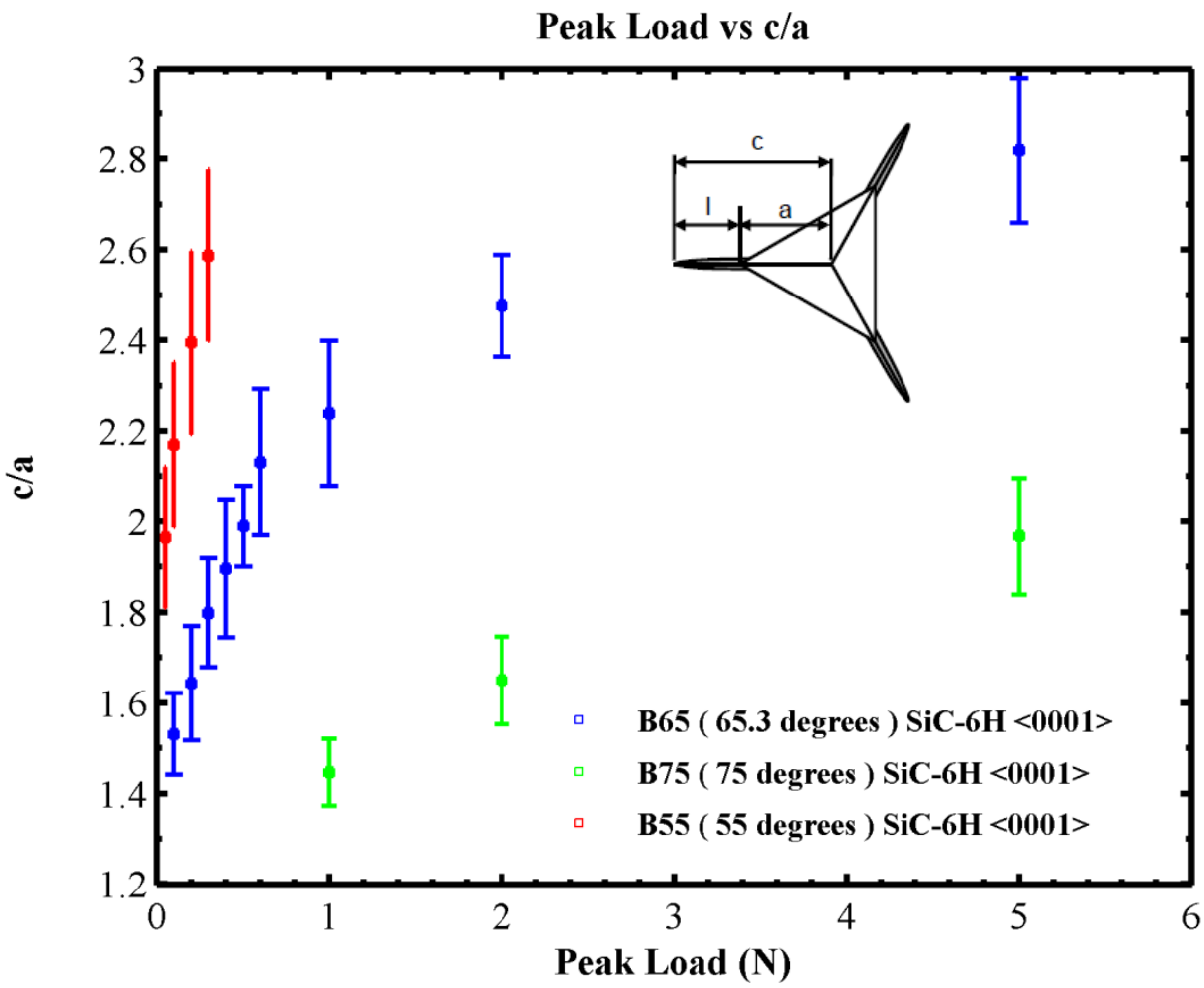

Figure 32: *P vs c/a* for indentation in SiC-6H<0001> with different pyramidal indenters.

Figure 33 shows the $P/c^{1.5}$ values at various peak loads for different centerline to face angle pyramidal indenters in SiC-6H <0001>. According to the Lawn, Evans, and Marshall model, the $P/c^{1.5}$ ratio should stay constant for a given material provided that there is no change in the cracking mode. It can be seen from the Figure 33 that the ratio stays approximately constant for the Berkovich indenter up to 1N peak load, after which it starts increasing. This might be indicative of a change from the median cracking to the Palmquist cracking regime.

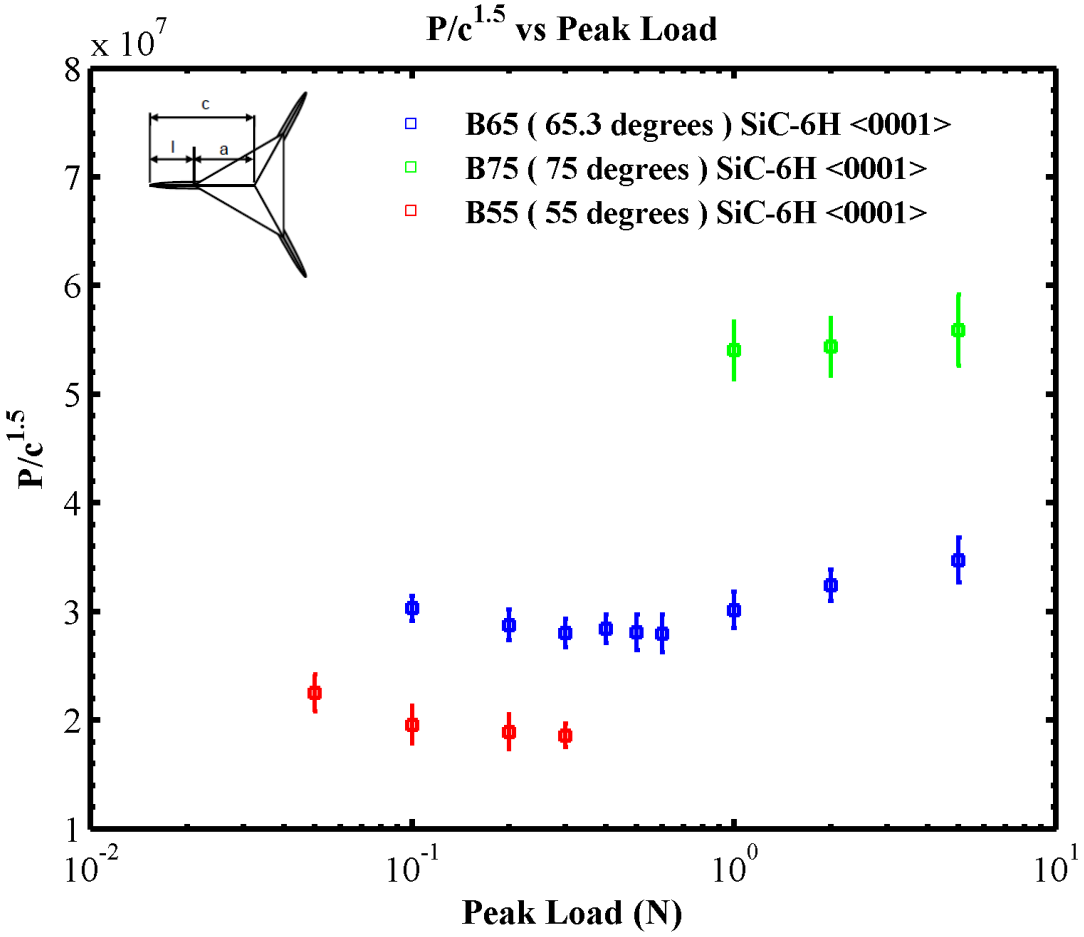

Figure 33: *P/c*$^{1.5}$ *vs Peak Load (N)* for SiC-6H <0001> indentation with different centerline to face angle indenters.

Figure 34 shows the fracture toughness of SiC-6H <0001> at various peak loads evaluated using both the Lawn and the Laugier models. The Lawn model gives constant values up to 1N loads, after which the Laugier model gives constant values. Since the Lawn model and the Laugier model were developed for median and Palmquist cracking systems respectively, it is conceivable that at low loads (<1N), the cracking is median radial type while at higher loads (>1N), the cracking is of Palmquist type. The observed fracture toughness is about 3.2 MPa.m$^{1/2}$.

Liang et al. [70] also obtained similar values of approximately 3 MPa.m$^{1/2}$ for polycrystalline SiC using indentation methods that were verified using SENB experiments.

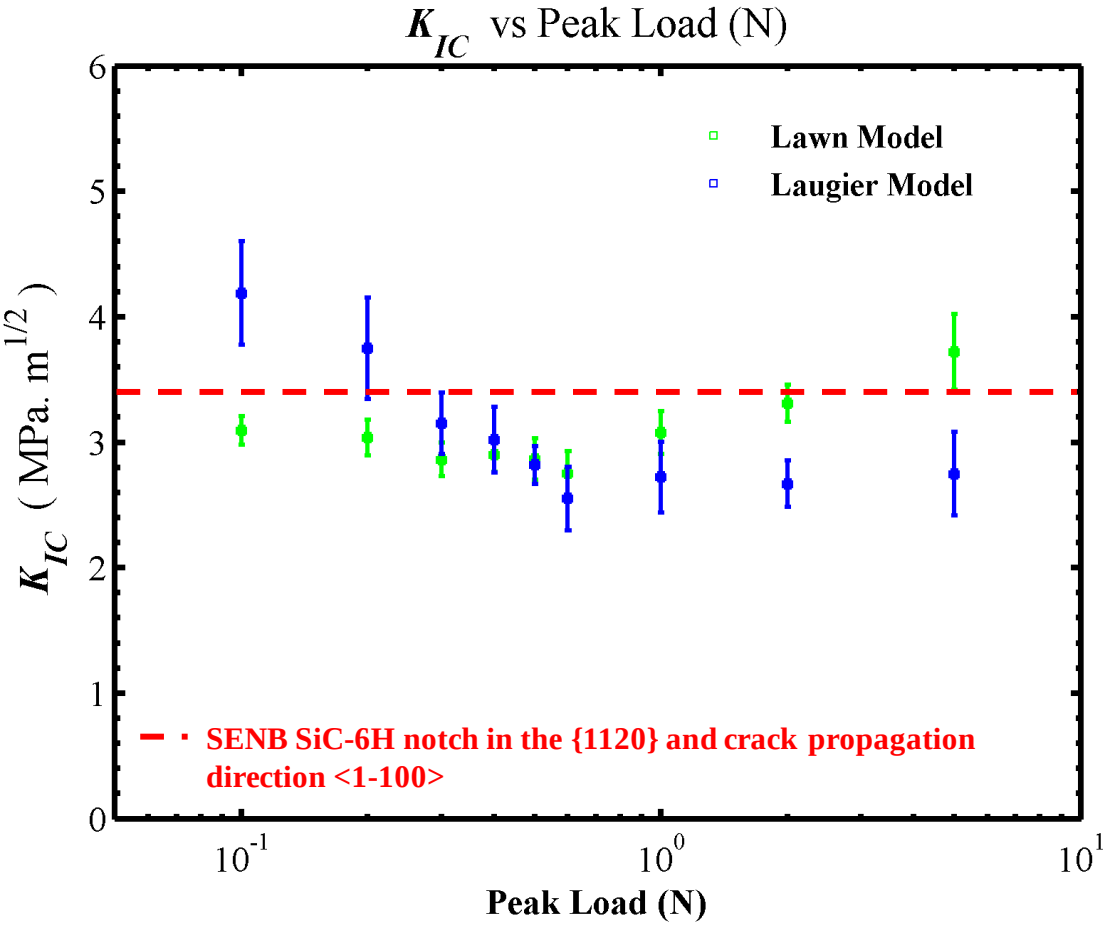

Figure 34: Fracture toughness measurement in SiC-6H<0001> using Berkovich indenter.

Applying the Laugier and the Lawn models for fracture toughness measurement with pyramidal indenters with different centerline to face angles requires accurate constants. In order to check whether the fracture toughness equations are valid for a given indenter, the Lawn equation and the Laugier equation can be modified to Equation 25 and Equation 26 respectively ,

$$K_{IC}/\alpha\left(\frac{E}{H}\right)^{1/2}=\left(\frac{P}{c^{3/2}}\right)=constant \tag{25}$$

$$K_{IC}/\chi_v\left(\frac{E}{H}\right)^{2/3}=\left(\frac{l}{a}\right)^{-1/2}\left(\frac{P}{c^{3/2}}\right)=constant \tag{26}$$

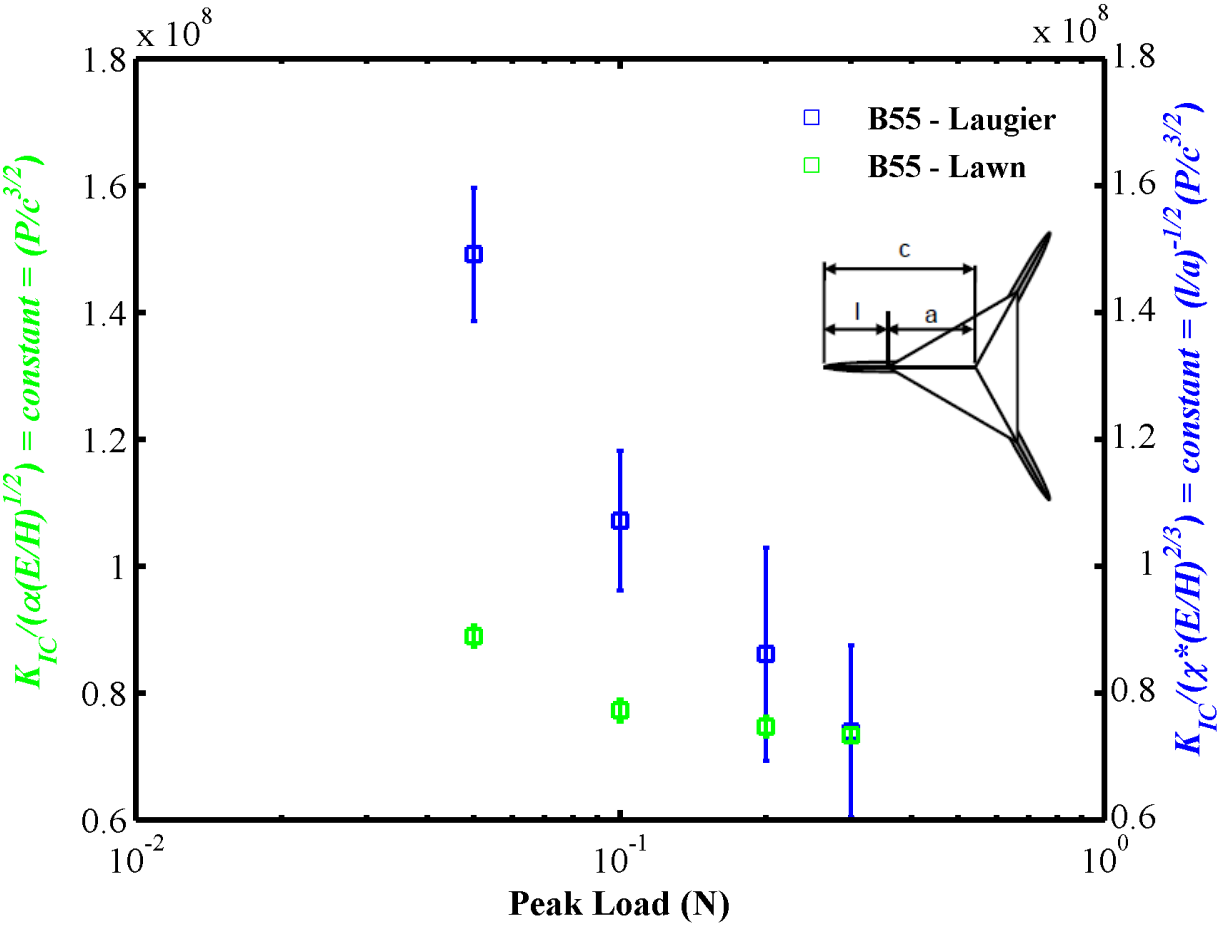

Figure 35: Evaluation of Laugier and Lawn models for fracture toughness measurement in SiC-6H <0001> using a 55° degree pyramidal indenter.

Figure 35 and Figure 36 show the evaluation of the validity of the Laugier and Lawn models for fracture toughness measurement in SiC-6H <0001>. It can be seen from Figure 35 that the Laugier model does not yield constant values for the modified equation at low loads for a

55° degree centerline to face angle indenter as compared to the Lawn model. It can be seen from Figure 36 that for a 75° degree centerline to face angle indenter, the Lawn model is valid for peak loads up to 5N. The Laugier model does not seem to yield constant values up to 5N peak load for a 75° pyramidal indenter. It is conceivable that at higher loads for a 75° indenter, the Laugier model might give constant values for fracture toughness.

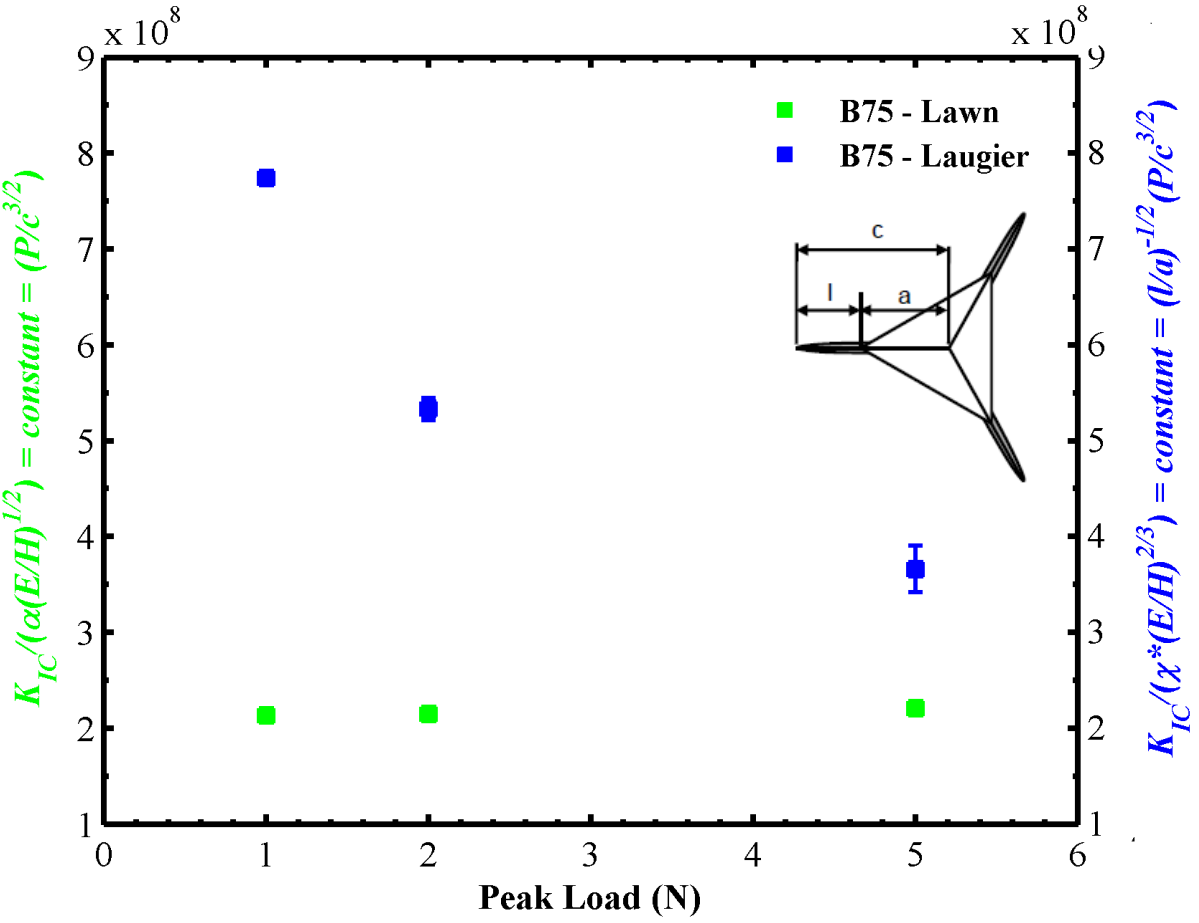

Figure 36: Evaluation of Laugier and Lawn models for fracture toughness measurement in SiC-6H <0001> using a 75° degree pyramidal indenter.

CONCLUSIONS

In this chapter, we have studied the indenter orientation effects in SiC-6H single crystals during Berkovich indentation experiments in the <0001> direction. Different center-line to face angle pyramidal indenters were used to study influence of indenter angle on the cracking behavior in SiC-6H in the <0001> direction. It is found that for a given peak load, a sharper indenter will produce more strains and thus larger penetration depth in a material. The crack lengths will also be larger for a sharper indenter at a given peak load. The Laugier and Lawn models for fracture toughness measurement were evaluated in different cracking modes. The more important results can be concluded as follows:

1. There is no orientation dependence on the cracking behavior around the c-axis, i.e SiC-6H is a transversely isotropic material.
2. The Lawn model for fracture toughness measurement seems to work much better than the Laugier model for the estimating the fracture toughness of SiC-6H <0001> single crystal samples within the range of our testing loads.
3. For a Berkovich indenter, it is conceivable that there is a change in the cracking mode as you increase from low peak loads (<100mN) to high peak loads (5N) as seen in $\boldsymbol{K_{IC}}$ vs Peak Load (mN) graph in Figure 34. It can be seen that the Lawn model, which is specifically for median radial cracking modes, works well at low peak loads while the Laugier model which is specifically for Palmquist cracking mode, works better at loads greater than 1N.

CHAPTER 7. Nanoindentation of polycrystalline ceramics

7.1 Berkovich Indentation

Nanoindentation experiments using pyramidal indenters with different face angles and spherical indenters with different tip radii were carried out on several polycrystalline SiC ceramics. Nanoindentation experiments were conducted primarily to analyze the variation of the elastic energy to total energy ratios, and modulus and hardness with respect to microstructure. Berkovich indentation tests were carried out at peak loads ranging from 25 mN to 500 mN.

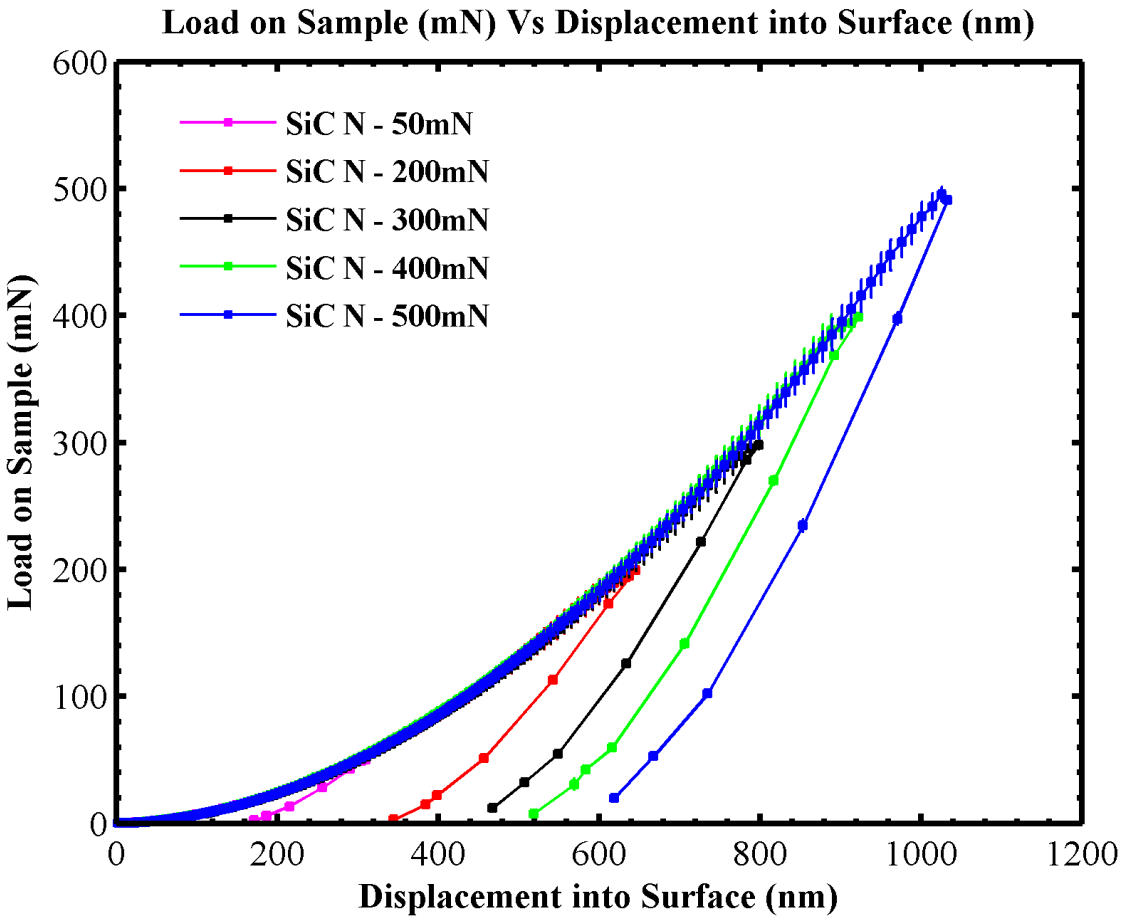

Figure 37: Average *P-h* curves for Berkovich indentation of SiC-N.

The modulus and hardness values obtained in an indentation experiment is compared to values obtained using ultrasonic measurements and other traditional testing methods available in literature. Figure 37 shows the P-h curves for Berkovich indentation of SiC-N at various peak loads. Figure 38 shows the average load-displacement curves for Berkovich indentation of polycrystalline SiC samples at a peak load of 100 mN.

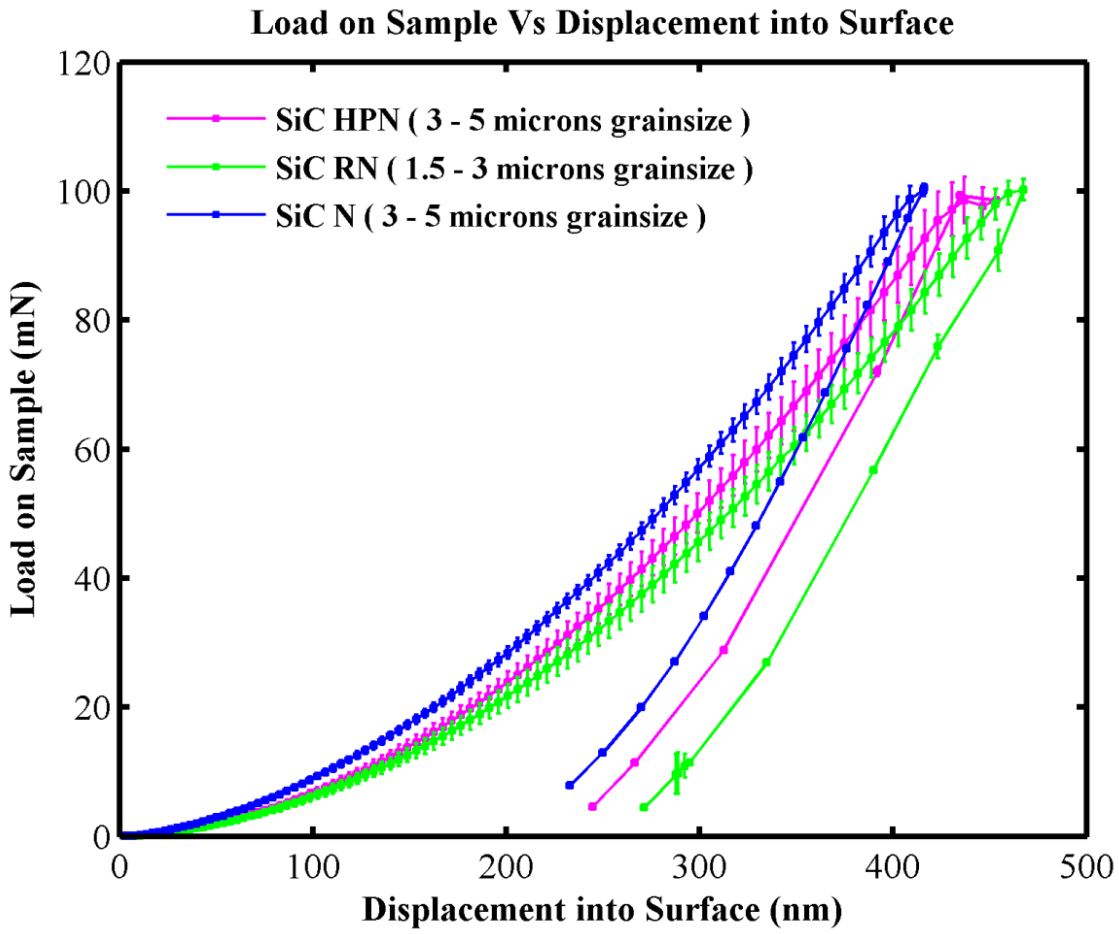

Figure 38: Average *P-h* curves for Berkovich indentation of polycrystalline SiC at 100 mN peak load.

The load displacement response for a polycrystalline material during a nanoindentation experiment is due to the contributions of the main phase and the intergranular phase. As seen

from the load – displacement curves, in Figure 38, the response is different for the different polycrystalline ceramics. This is partially due to the fact that at a 100 mN peak load the size of the indent is about 2-3 µm which is more than the average grain size in SiC-RN but not the other samples. Figure 39 shows average load-displacement curves for Berkovich indentation at a 500 mN peak load. At this load, the size of the indent of about 7 µm is greater than the average grain size of all the materials and therefore the load-displacement response for a 500 mN peak load Berkovich indentation experiment is similar for all the materials. The response of SiC-RN at 100 mN peak load is different than the other two polycrystalline samples, due to the different grain size 1.5-3 µm compared to 3-5 µm.

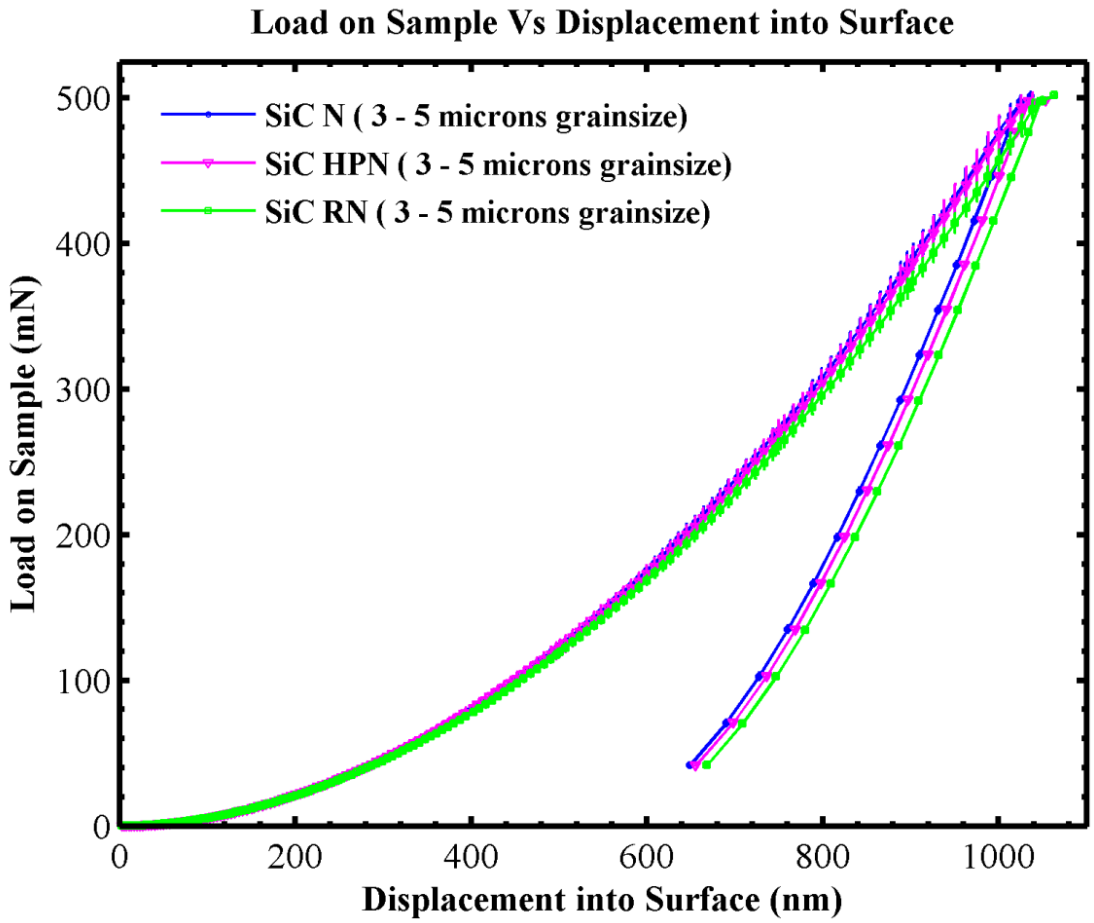

Figure 39: *P-h* curves for Berkovich indentation of polycrystalline SiC at 500 mN peak load.

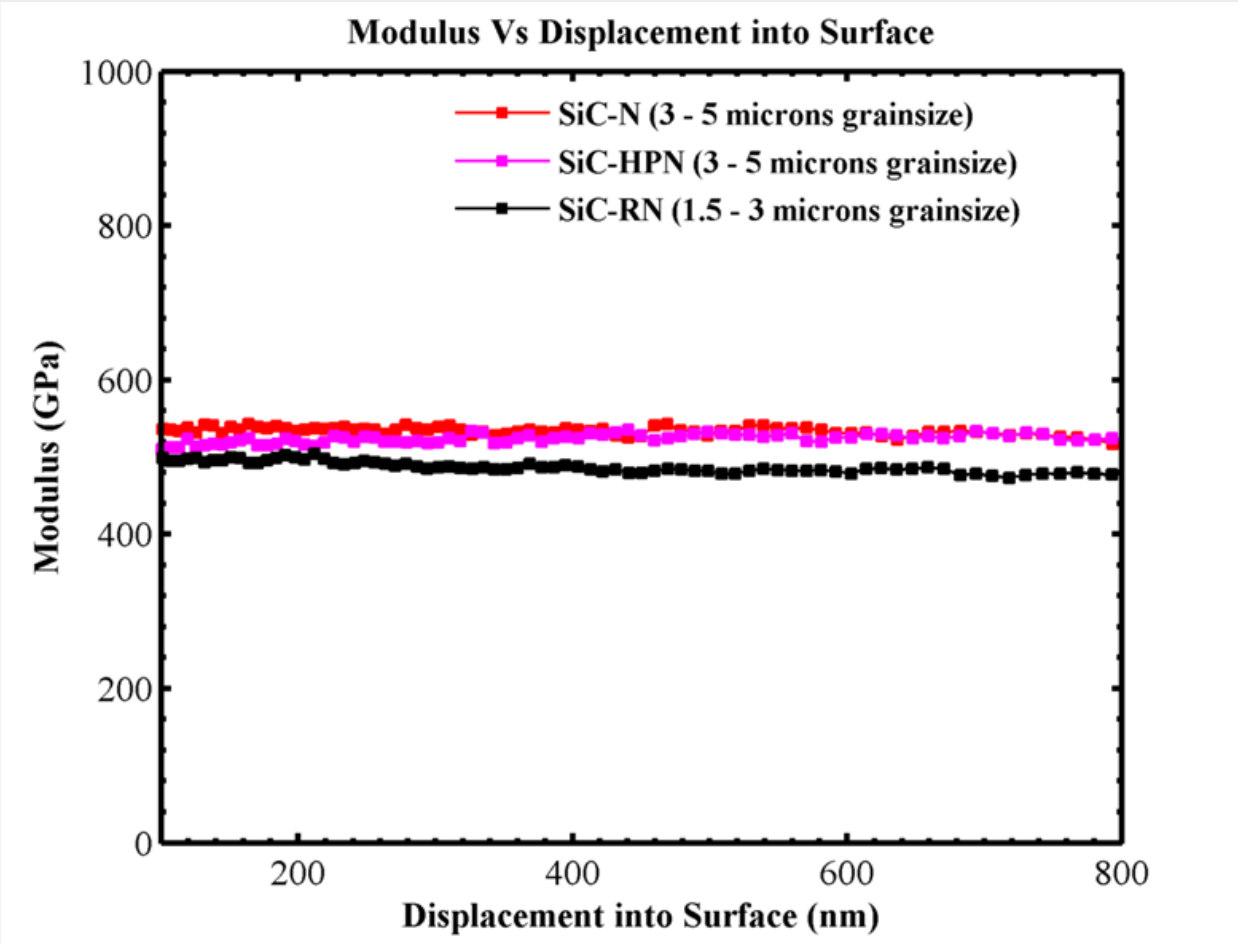

Figure 40: Modulus vs displacement into surface curves for different polycrystalline ceramics using Berkovich indentation.

Figure 40 and Figure 41 show the modulus and hardness vs displacement into the surface for different polycrystalline SiC samples during a Berkovich indentation experiment. It can be seen that all the polycrystalline SiC samples show very similar hardness and modulus values the difference between the highest modulus (SiC-N) and the lowest modulus (SiC-RN) being approximately 10%. It can be seen from Figure 41, that all the three polycrystalline samples show an indentation size effect. The effect is more pronounced for SiC-N than the other two. The SiC-RN seems to show an indentation size effect up to a penetration depth of 400 nm after which

it is relatively constant. The indent size at 400 nm is about 2.5 - 3 µm while the average grain size for SiC-RN is about 1.5 – 3 µm. It is conceivable that the indentation size effect at low loads and low penetration depths in SiC-RN is due to orientation effects. As soon as the indent size is equal to or greater than the average grain size of the material the indentation size effect is no longer seen. Similar arguments can be made for SiC-N and SiC-HPN.

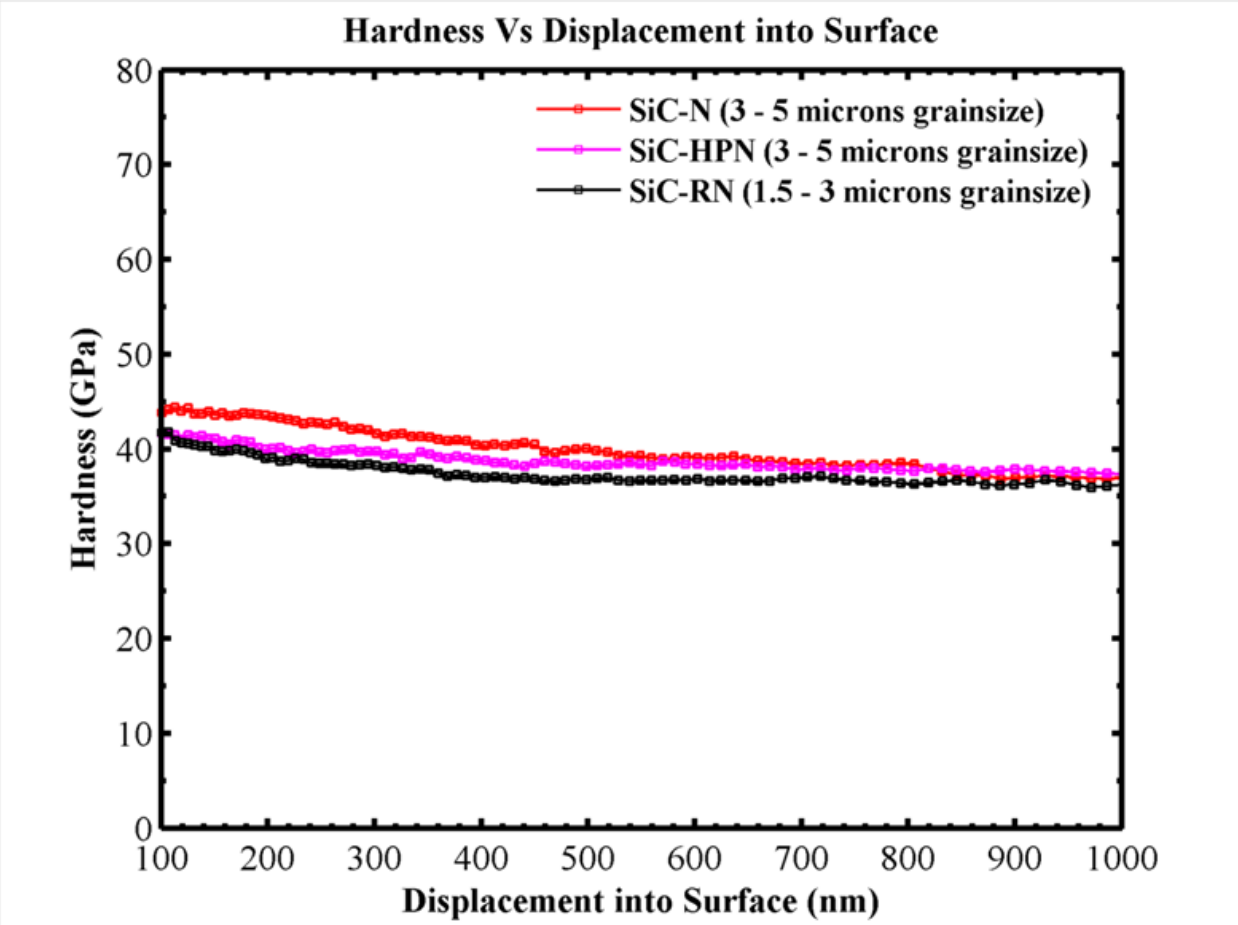

Figure 41: Hardness vs displacement into surface curves for different polycrystalline ceramics using Berkovich indentation.

Figure 42 shows representative SEM images of maximum and minimum damage in SiC-RN during Berkovich indentation at various peak loads. The indentation response of a material is

primarily due to the contributions of the main phase (SiC), the intergranular phase and cracking effects. The secondary phase in the polycrystalline SiC samples used in this research is primarily inorganic oxides which are softer and more compliant (stiffness). The local volumetric ratio between the main phase and the intergranular phase can affect the response at low indentation loads (low penetration depths). Figure 43 shows the modulus and hardness during a Berkovich indentation experiment at various indentation depths in SiC-RN. The modulus and hardness are relatively constant over the entire range of indentation depths. At peak loads of less than 25 mN, when the indentation depths are approximately 200 nm, which corresponds to an indent size of approximately 1.5 μm, there is an increased scatter in the modulus and hardness values. Since the indent size is less than or equal to the average grain size, the scatter may be due to local volumetric ratio between the main and secondary phase and cracking in addition to the anisotropy. However, for peak loads greater than 100 mN which corresponds to a penetration depth of approximately 450 nm there is hardly any scatter in the modulus and hardness values. The modulus and hardness values at peak load greater than 200 mN are relatively constant. This indicates that the grain boundary phase, the secondary phase or cracking effects does not play a significant role in the hardness and the modulus material response when the indent size is greater than the average grain size.

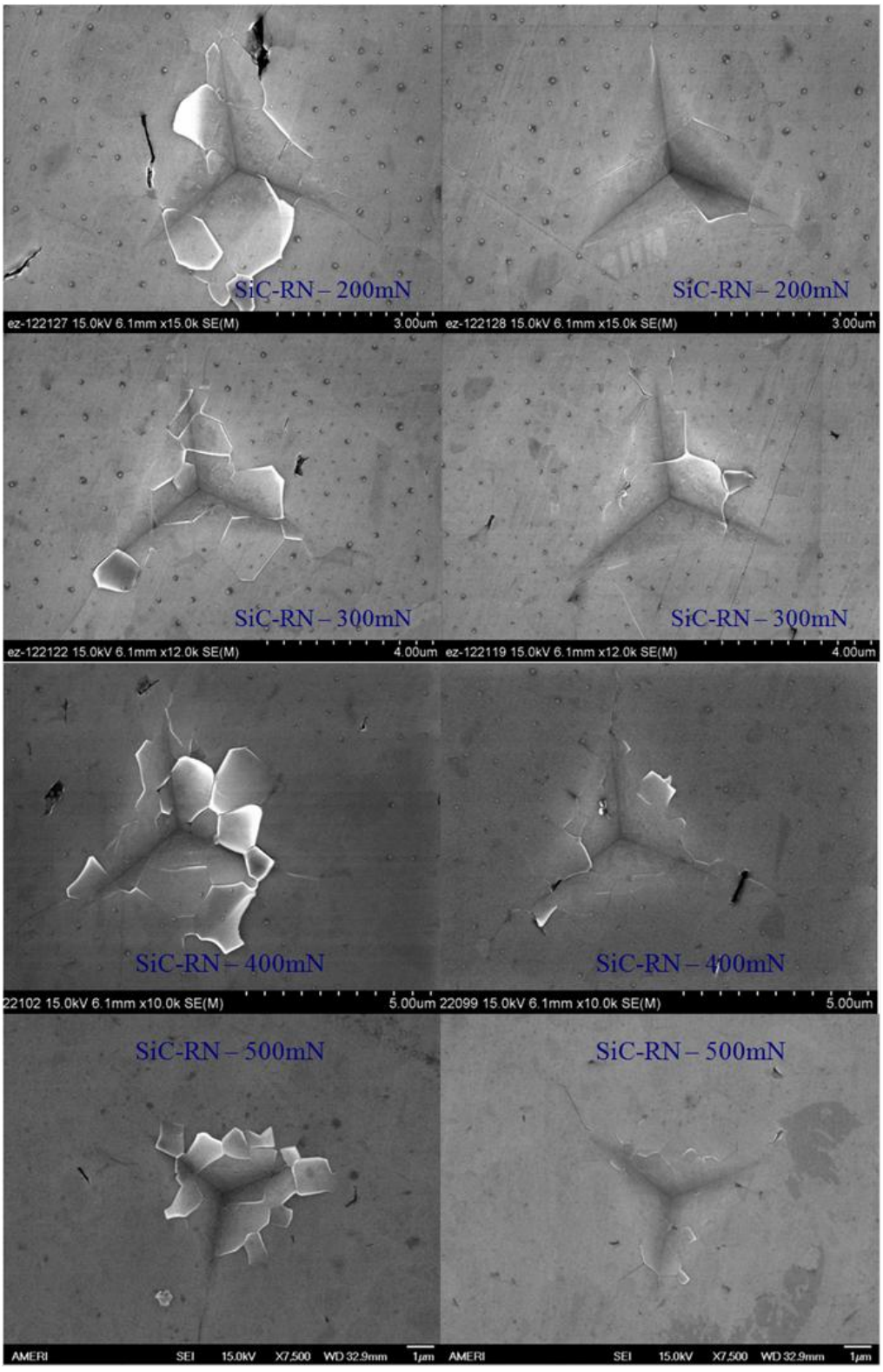

Figure 42: Representative images showing maximum damage and minimum damage during Berkovich indentation in SiC-RN at different peak loads.

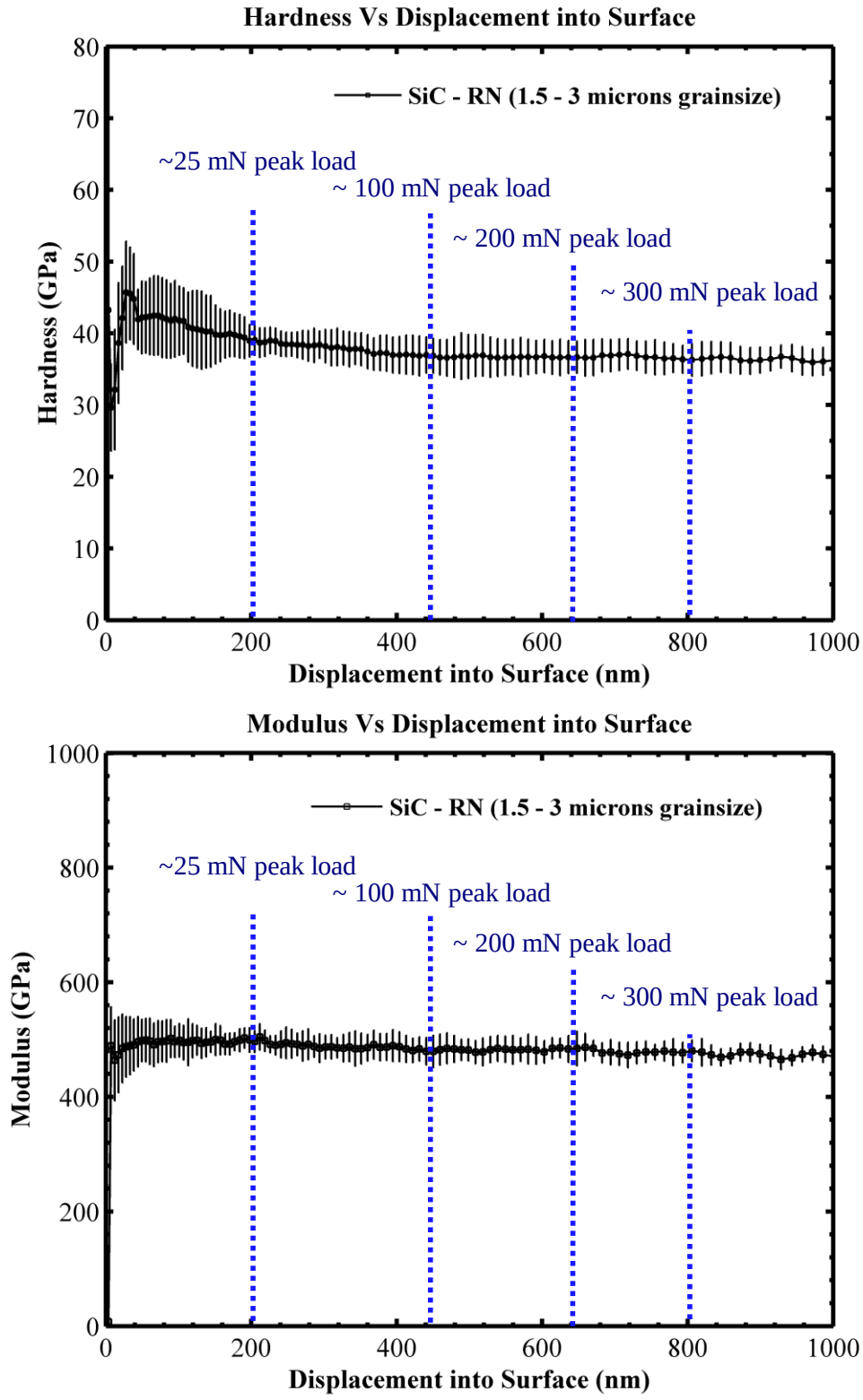

Figure 43: *E-h* and *H-h* curves for SiC-RN in a Berkovich indentation experiment.

Figure 44 shows representative SEM images of different polycrystalline ceramics (SiC-N, SiC-RN and SiC-HPN) along with Cree SiC-6H at 500 mN peak load. At 500 mN peak load, the indent size in these SiC polycrystalline ceramic samples is about 7 μm. It can be seen from the SEM images that the SiC-RN sample with the smallest average grain size (1.5 - 3 μm), has more grain push out than the SiC-N and SiC-HPN with a larger average grain size (3 – 5 μm). It can be seen from these results and the results from Figure 42, that the grain boundary phase, the secondary phase and cracking does not have a major affect the modulus and hardness measurements when the indent size is larger than the grain size. Table 11 summarizes the results for the Berkovich indentation experiments on different polycrystalline SiC samples.

Table 11: Experimental hardness and modulus values of different polycrystalline SiC.

	E_{OP} (GPa)	H_{OP} (GPa)	$E_{Literature}$ (GPa)	$H_{Literature}$ (GPa)
SiC-N	530.13 ± 31.12	40.04 ± 4.09	453.7	27.2
SiC-HPN	527.99 ± 36.67	38.16 ± 4.34	443.1	25.3
SiC-RN	483.74 ± 34.14	36.96 ± 3.10	431.5	28.9

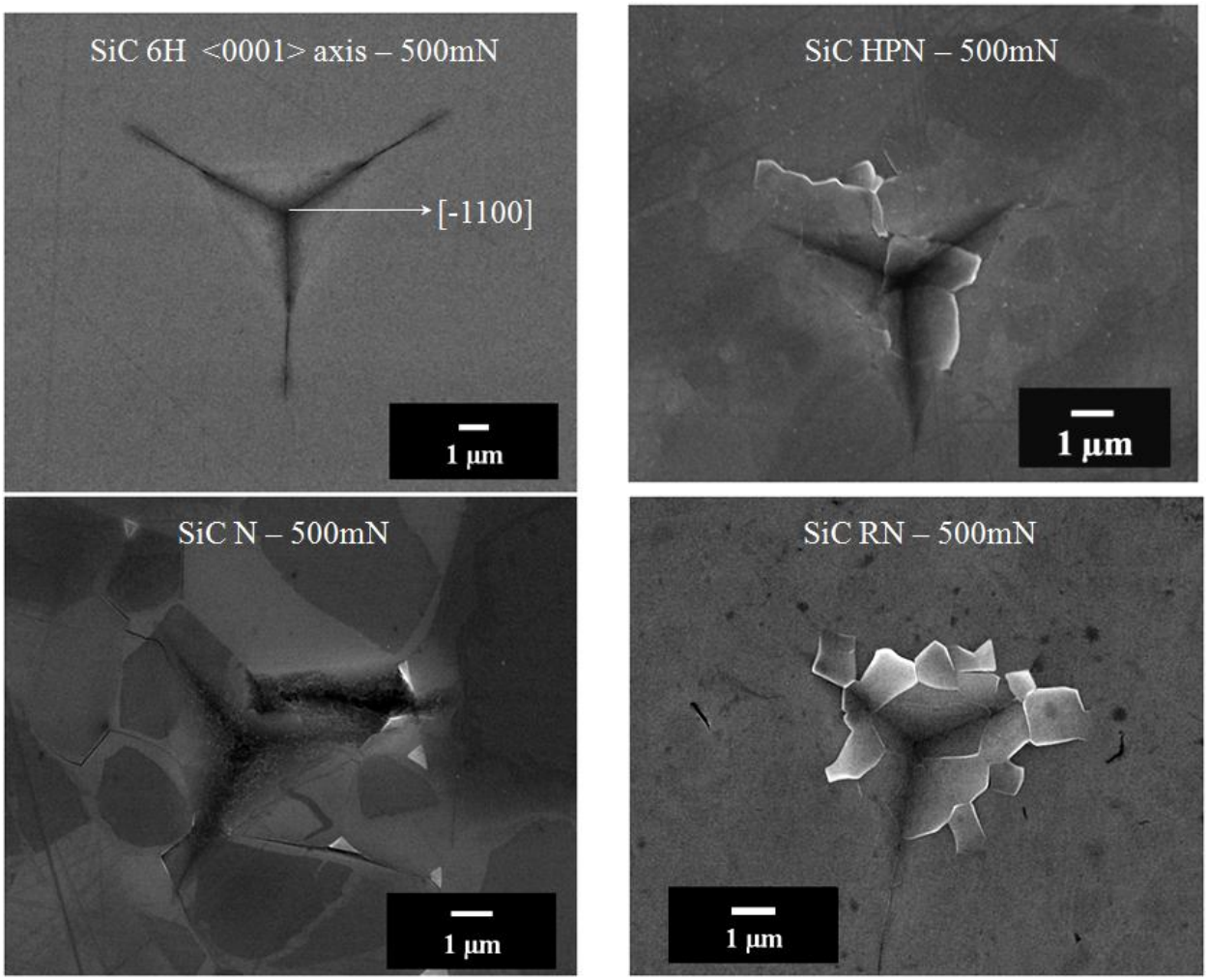

Figure 44: Representative SEM images of Berkovich indentation in polycrystalline SiC at 500mN peak load.

7.2 Spherical Indentation

Figure 45 and Figure 46 shows load-displacement curves for spherical indentation experiments using a 7.5 µm diameter and a 50 µm diameter tip respectively.

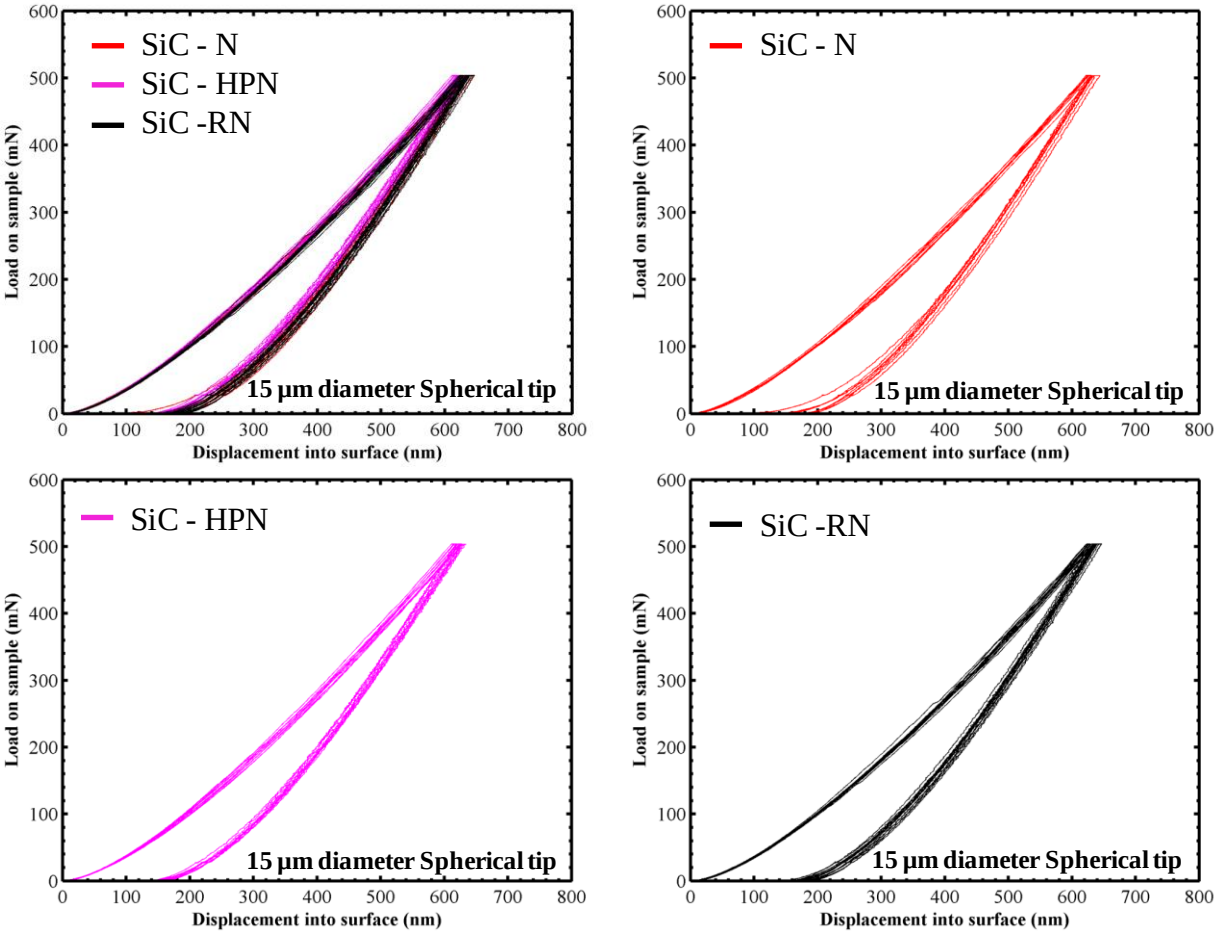

Figure 45: Load displacement response of different polycrystalline SiC materials during spherical indentation experiments with a 15 µm diameter tip.

It can be seen that that there is hardly any difference in the response of the three polycrystalline SiC materials examined in this research during spherical indentation experiments. The indentation response for the 15 µm diameter spherical tip is elastic plastic for all materials while the response for 50 µm diameter tip is completely elastic for all materials. In previous work, Wereszczak et al. [82] showed that there is a difference in the fracture and cracking modes in different polycrystalline ceramics. However, those loads were in excess of 100 N which is outside the testing limits of the current nanoindentation equipment.

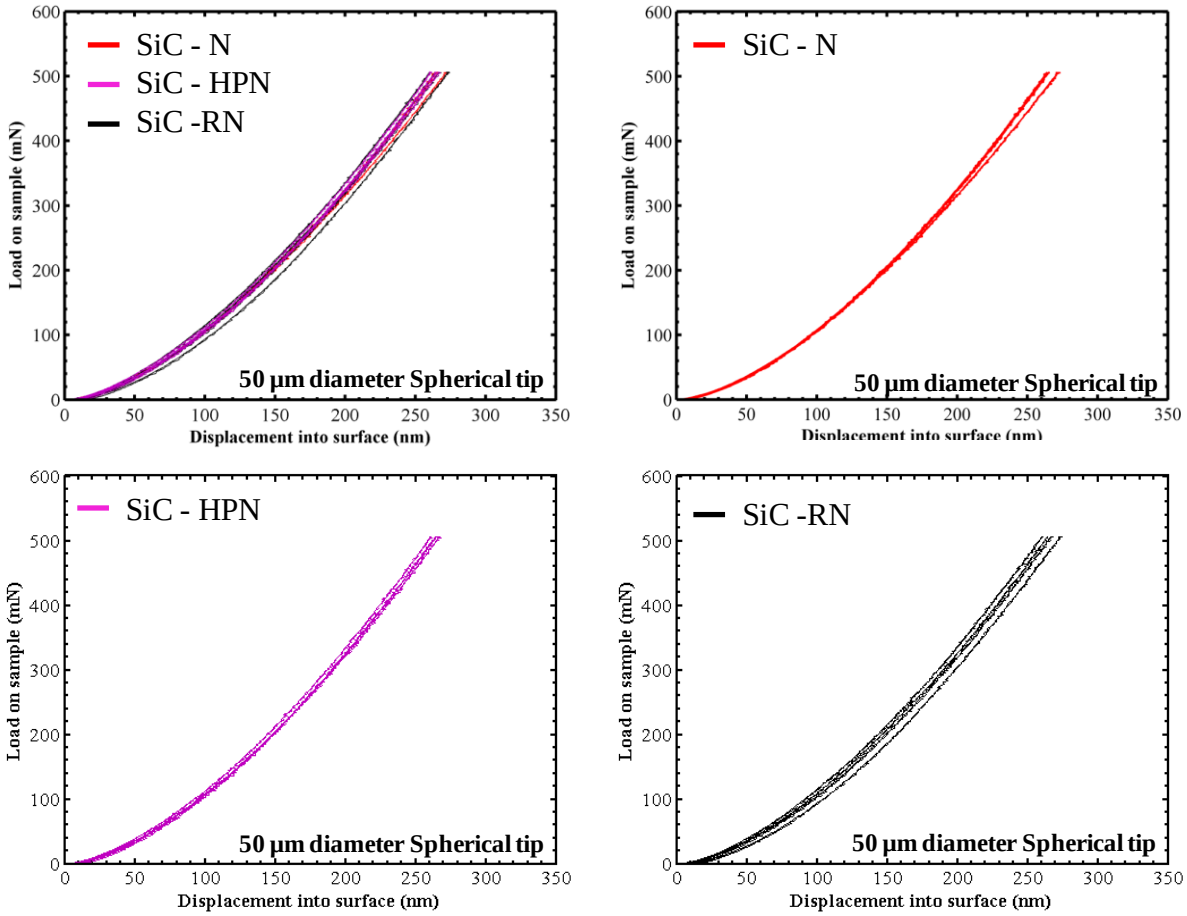

Figure 46: Load displacement response of different polycrystalline SiC materials during spherical indentation experiments with a 50 µm diameter tip.

CONCLUSION

In this chapter, we have studied the response of different polycrystalline SiC ceramics to Berkovich and spherical indentation. Since the indentation response of a material is due to the main phase, the secondary phase and indentation related effects like cracking etc., it is sensitive to local volumetric ratios at low peak loads when the indent size is less than the grain size. It is found that the hardness and modulus measurements, at peak loads (greater than 100 mN in case

of SiC-RN and 300 mN in case of SiC-N and SiC-HPN) when the indent size is large enough to incorporate multiple grains, are relatively independent of grain boundary effects, cracking effects and grain push out. Based on these observations, it can be postulated that the difference in the load displacement response of SiC-RN, SiC N and SiC-HPN during Berkovich indentation at 100 mN peak load, when the indent size is less than the average grain size, is due to grain size.

1. At larger peak loads > 300 mN when the indent size is greater than the average grain size the load displacement response is similar.
2. The response of different polycrystalline materials to spherical indentation is almost the same. This might be due to the peak load limitations.
3. All three polycrystalline materials show very little difference in the hardness and modulus at 500 mN peak load. SiC-N has the highest modulus and hardness (530 GPa and 40 GPa respectively) of all polycrystalline ceramics tested using Berkovich indentation.
4. The response to spherical indentation using a 15 μm and 50 μm diameter spheres is similar for all three polycrystalline SiC samples contrary to the results shown by Wereszczak et al. [82]. This is due to the load limitations on the equipment.

CHAPTER 8. Energy Analysis of Berkovich Indentation in SiC

8.1 Energy Analysis of Berkovich indentation in single crystal Cree SiC-6H

Figure 47 shows the plastic energy over total energy (PE/TE) ratios for Berkovich indentation at various peak loads and corresponding peak displacements for Cree SiC-6H <0001>, Cree SiC-6H <01-10>, and fused silica. The plastic energy over total energy ratios for a material during Berkovich indentation experiments should remain constant for a homogeneous material, provided the indenter is infinitely sharp. As seen in Figure 47, SiC-6H <0001> does not show constant PE/TE ratios at varying peak loads and peak displacements whereas the ratios for SiC-6H <01-10> and fused silica stay relatively constant.

This behavior in SiC-6H<0001> can be attributed to several possible factors;

1. Tip Defects – tip shape at low penetration depths.
2. Cracking effects.
3. Pop-ins at low loads.
4. Self similarity.

A systematic study to examine these factors was carried out. As seen in Figure 47, the PE/TE values for fused silica stay constant at penetration depths of 200nm which means that the tip shape is not a factor. A correction for area under the loading curve was applied where the area under the curve for the pop-in portion was subtracted from the area under the loading curve which results in an increase in the PE/TE ratios. However, it can be seen from Figure 48 that the increase in PE/TE ratios is only about 1.8 % at low penetration depths of around 300 nm and after that the values remain relatively unchanged. It can be also seen from Figure 49, which shows the c/a ratios vs peak load for Berkovich indentation experiments in SiC-6H <0001> and

SiC-6H <01-10>, that there is an indentation size effect on the crack lengths in SiC-6H <0001> since the c/a ratio keeps increasing with an increase in indentation load. On the other hand, the c/a ratios for SiC-6H<01-10> do not show a significant increase with an increase in the peak load.

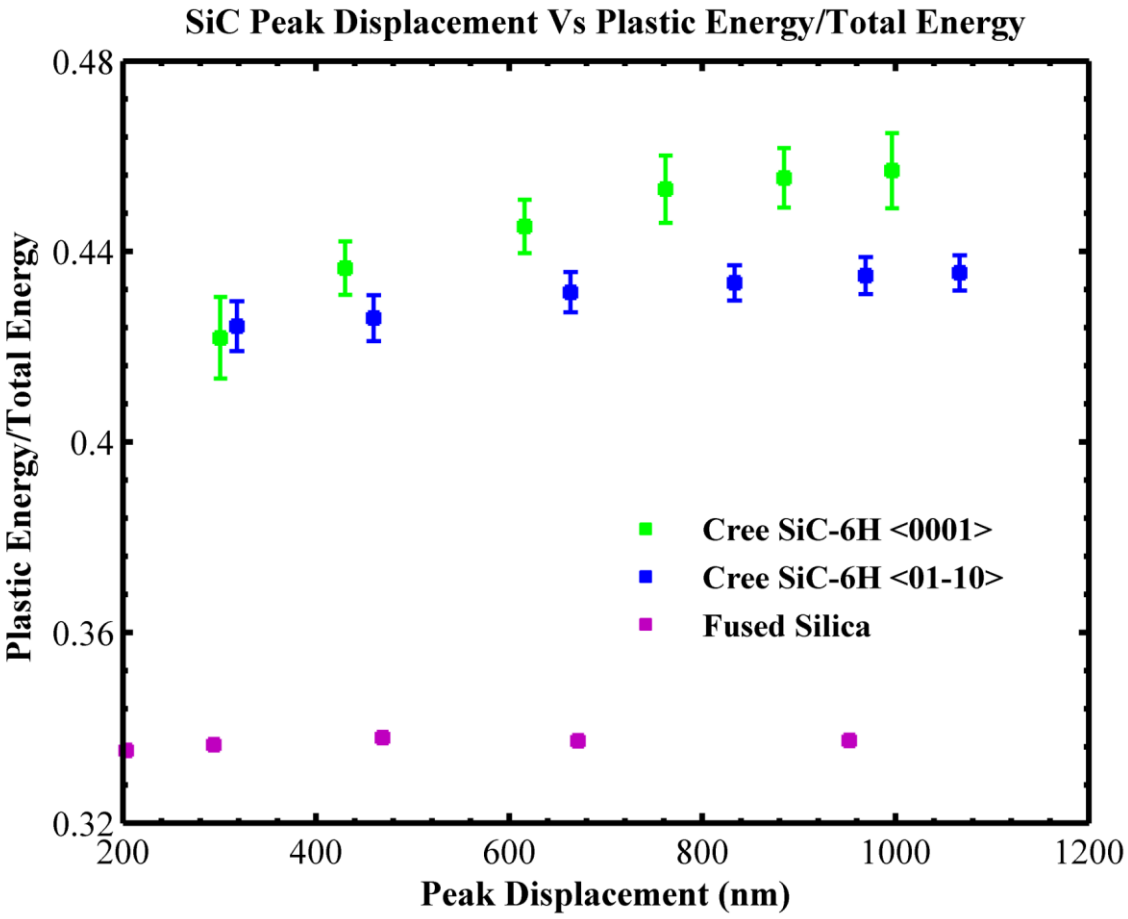

Figure 47: PE/TE vs peak displacements for Berkovich indentation in Cree SiC-6H.

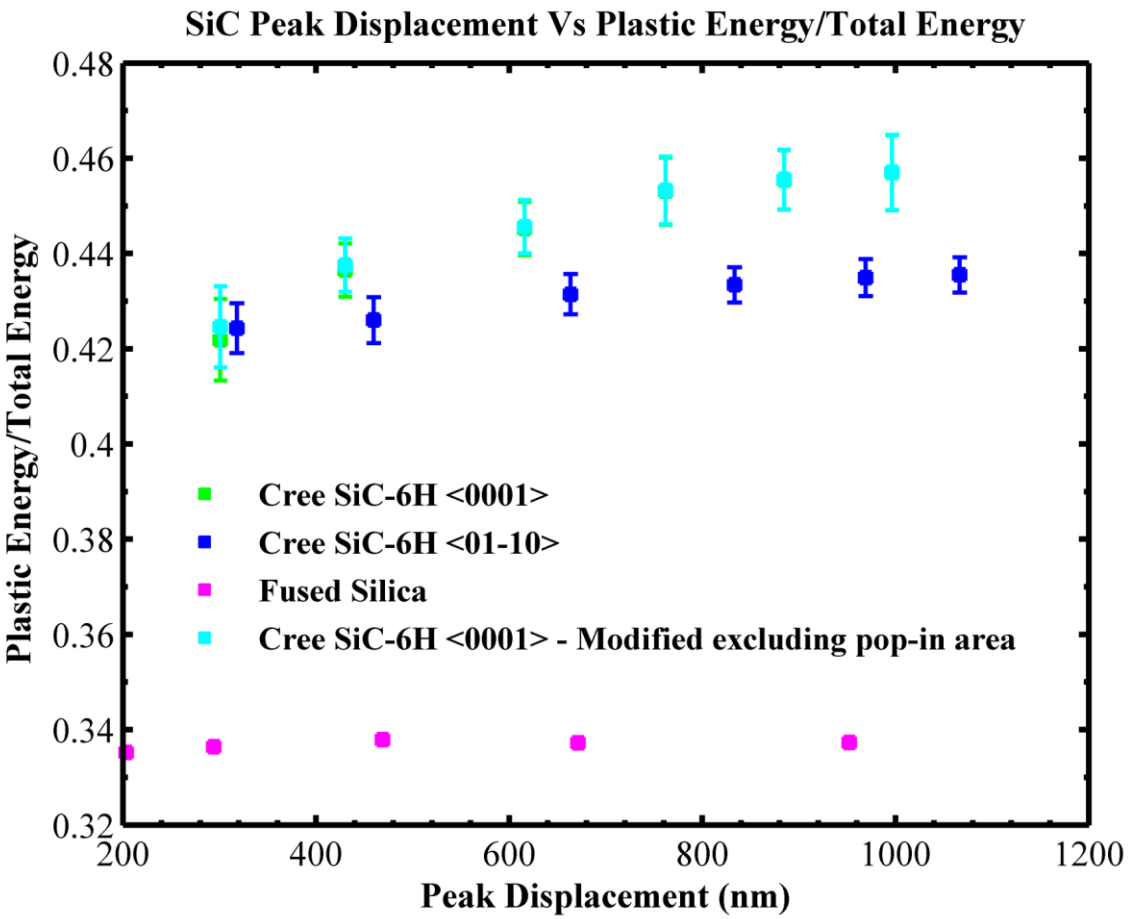

Figure 48: Modified PE/TE ratios excluding pop-in area for Berkovich indentation in Cree SiC-6H.

The results above show that the PE/TE ratios for Berkovich indentation in SiC-6H in the <0001> direction do not remain constant due to cracking effects, self similarity of the indentation and other possible orientation and material effects that are not fully understood. A detailed TEM study on indents prior to crack initiation and post crack initiation would help to reveal the reason for the difference in the ratios at low and high peak loads.

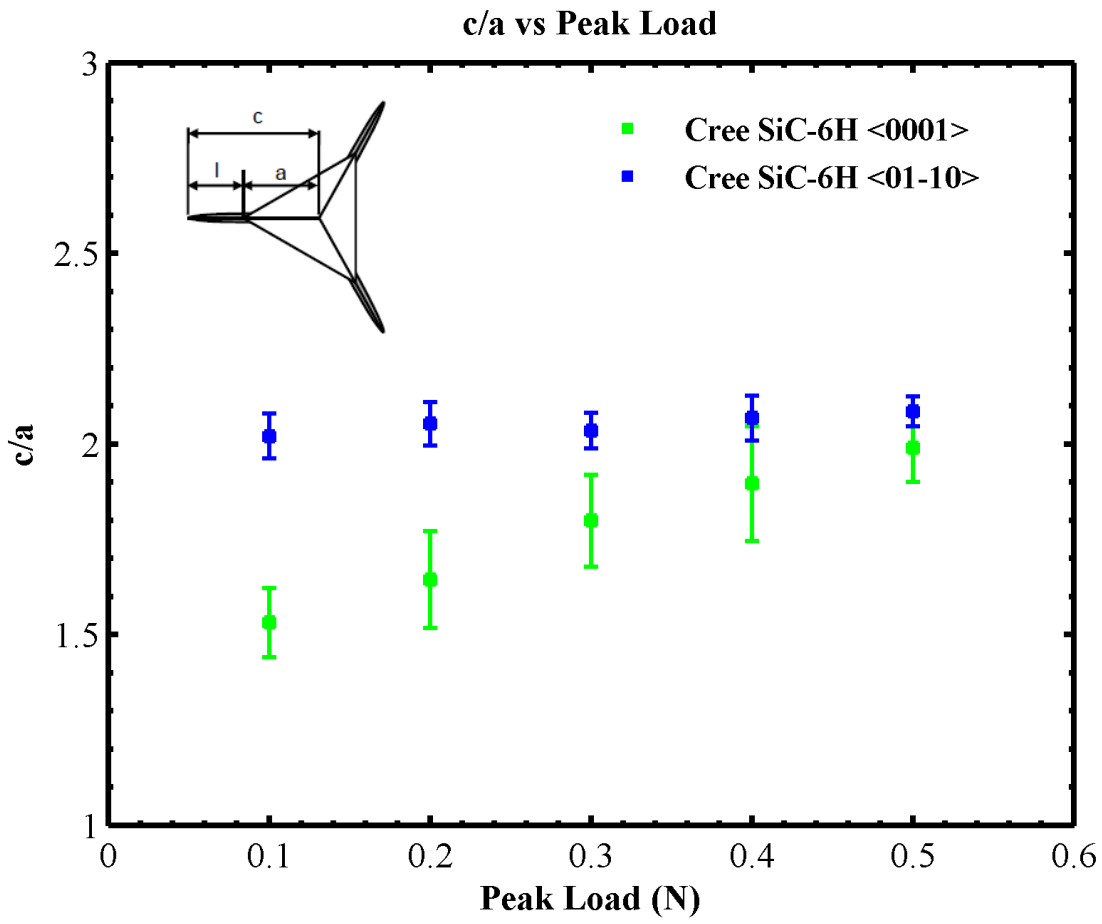

Figure 49: c/a vs P for Berkovich indentation in Cree SiC-6H <0001> and <01-10>.

8.2 Energy analysis of Berkovich Indentation in polycrystalline ceramics

Figure 50 and Figure 51 show the PE/TE ratios at various Peak loads and peak displacements, respectively. The parameter S shown in the Figure 50 is defined as the length of the side of the indent at a particular depth, which is equal to approximately 7.5 times the depth for a Berkovich indenter. The two main differences in the different polycrystalline ceramic samples are the grain size and the secondary phase. Previous research has shown that the variation between the modulus and hardness of the three grades is very small (<10%).

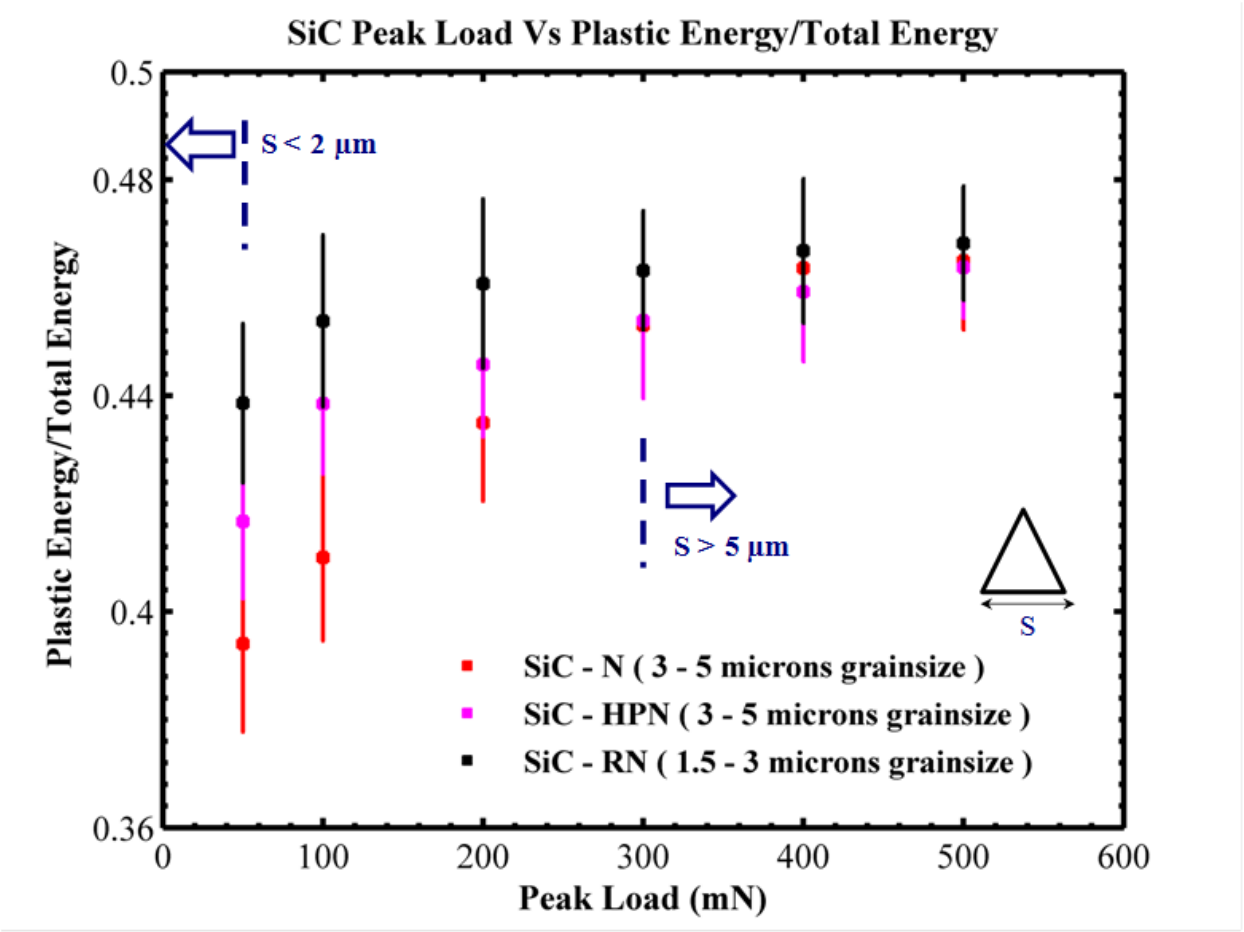

Figure 50: PE/TE vs Peak load for Berkovich indentation of polycrystalline SiC.

The PE/TE ratios for all the three polycrystalline materials increase with an increase in the peak load or peak displacement during Berkovich indentation experiments. It can be seen from the Figure 50 and Figure 51 that, in SiC-N for peak loads of 50 mN, when the size of the indent is less than the average grain size of the material, the average values of PE/TE is about ~ 0.39 and it increases to ~ 0.46 at higher loads indicating that there is possibly a grain size effect and not just due to the unique trend found in SiC-6H <0001>. Interestingly, in Figure 50 and Figure 51 the values of the PE/TE ratios become relatively constant at higher loads (> 300 mN) for all polycrystalline SiC samples. At peak loads greater than 300 mN, when the indent size is

large enough that the stressed volume of the material beneath the indenter incorporates more than one grain, the material response is the same. The PE/TE ratios for SiC-RN at 50 mN are the highest of all three polycrystalline materials. SiC-RN has the smallest grain size and at 50 mN peak loads the indent size is equal to the average grain size indicating that the deformation response is from just a few grains. SiC-N and SiC-HPN have a larger grain size, and at the 50 mN peak load the indent size is small enough that the response is only from one grain or a few grains. SiC-N and SiC-HPN show different PE/TE ratios at low peak loads, even though the average grain size is the same due to different grain boundary phases.

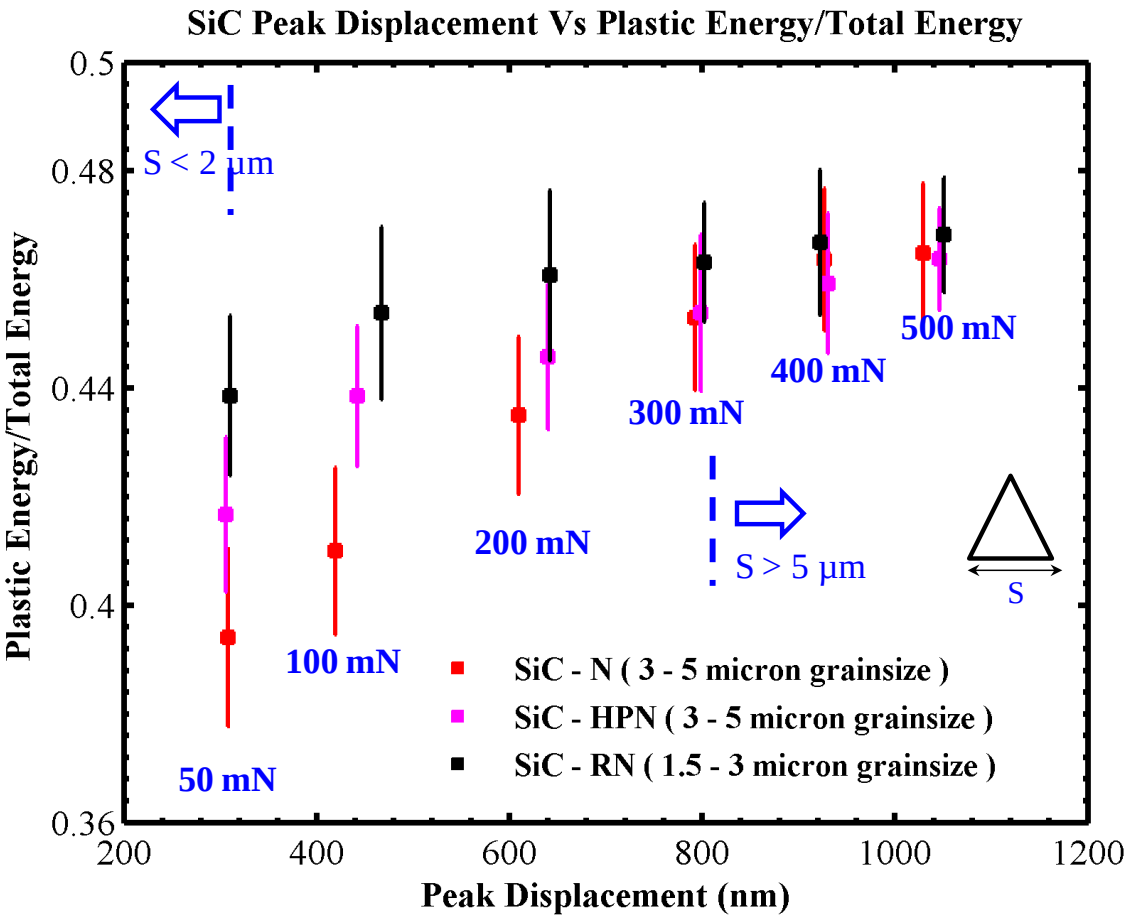

Figure 51: PE/TE vs Peak displacement for Berkovich indentation of polycrystalline SiC.

Berkovich indentation experiments at 25 mN peak load were carried out on SiC-N samples. Figure 52 shows the PE/TE ratios for various indents in SiC-N. SEM images of a few indents are shown in Figure 53 and Figure 54. The results in Figure 52 show that when an indent is near the center of the grain, the PE/TE ratios are similar to the ratios of single crystal SiC-6H.

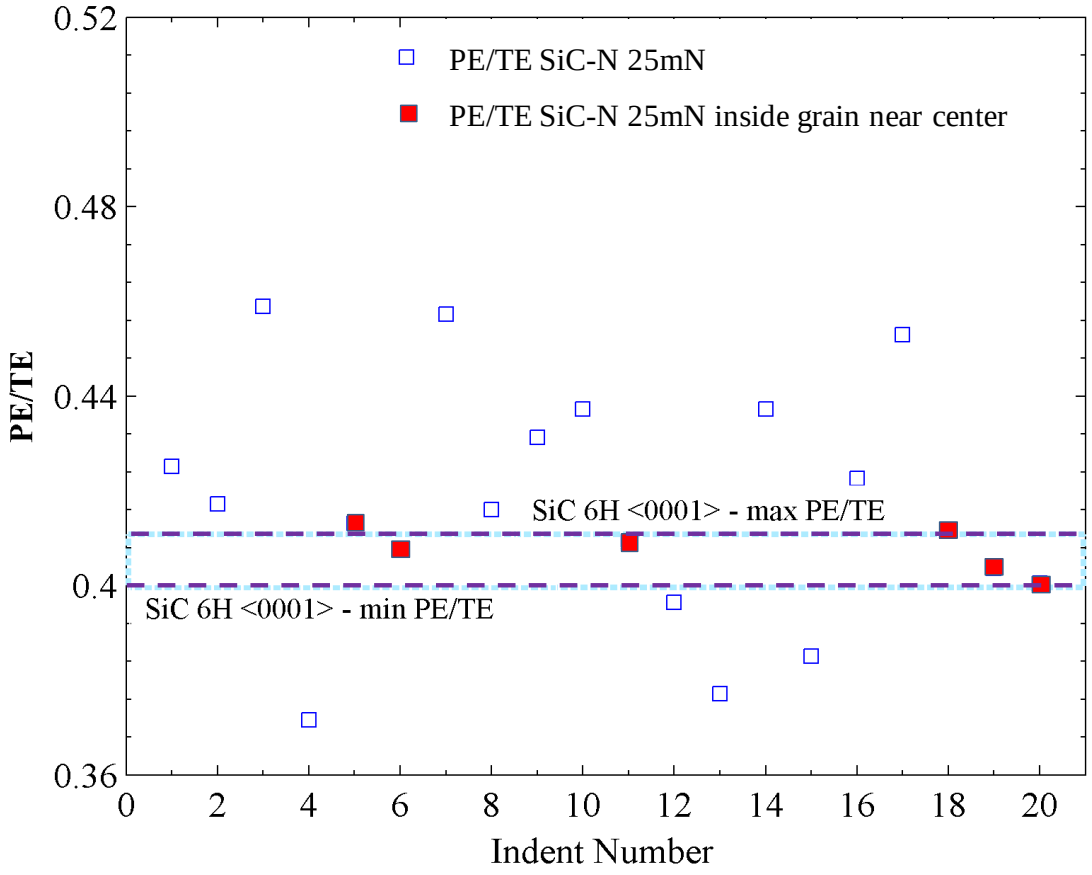

Figure 52: PE/TE ratio for various 25mN Berkovich indents in SiC-N.

The PE/TE ratios for indents close to the grain boundary or on the grain boundary are either higher or lower than single crystal SiC-6H. This indicates that the grain boundary phase might play a major role in the energy dissipation mechanism at low loads and small contacts. At low

loads, when the indent size is less than grain size, if the indent is at or near the grain boundary it is conceivable that a lot of energy is dissipated in grain boundary motion, which would indicate higher PE/TE ratios compared to when the indent is at or near the center of the grain.

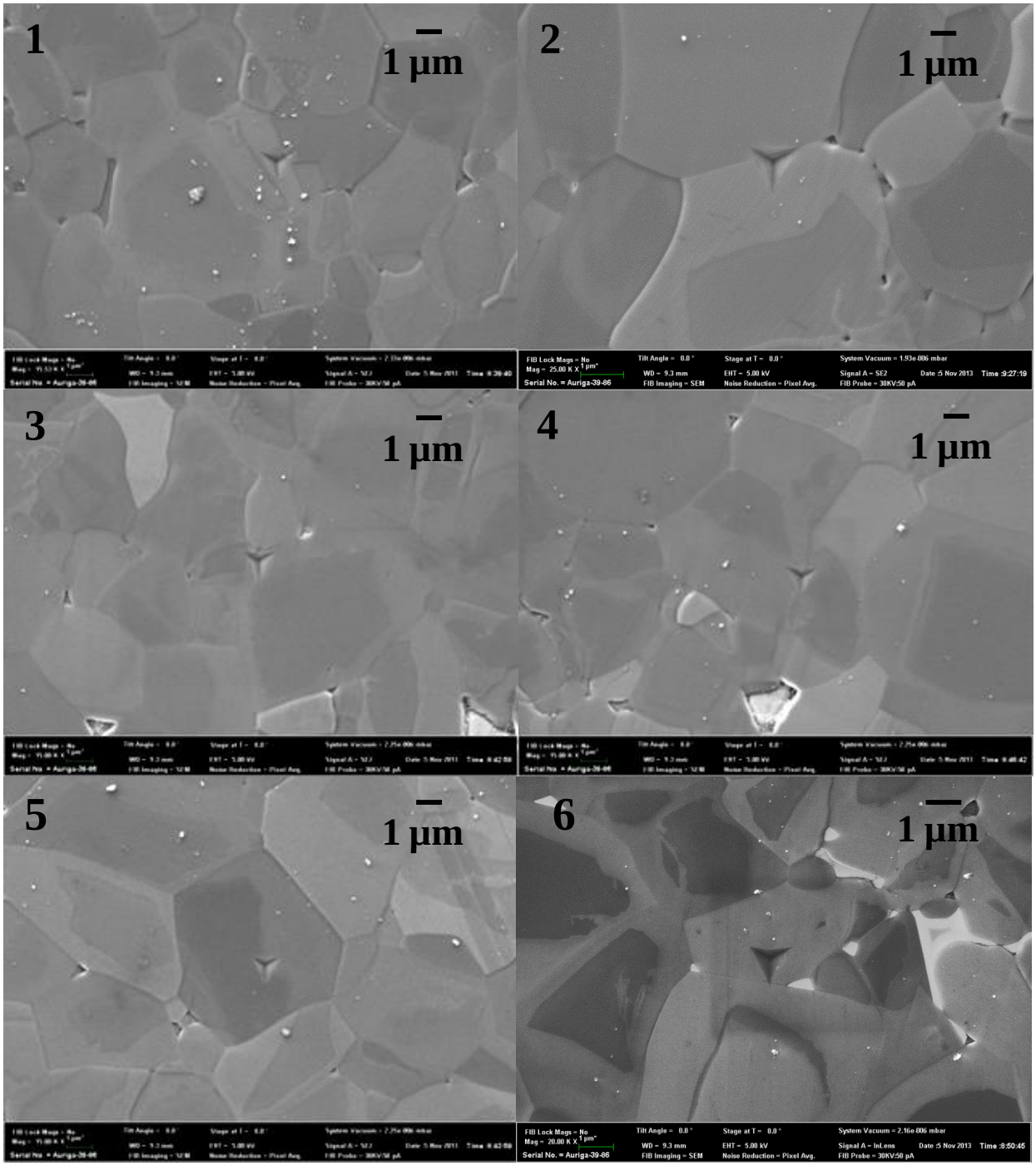

Figure 53: SEM images of Berkovich indentations at 25mN peak load in SiC-N indents (1-6).

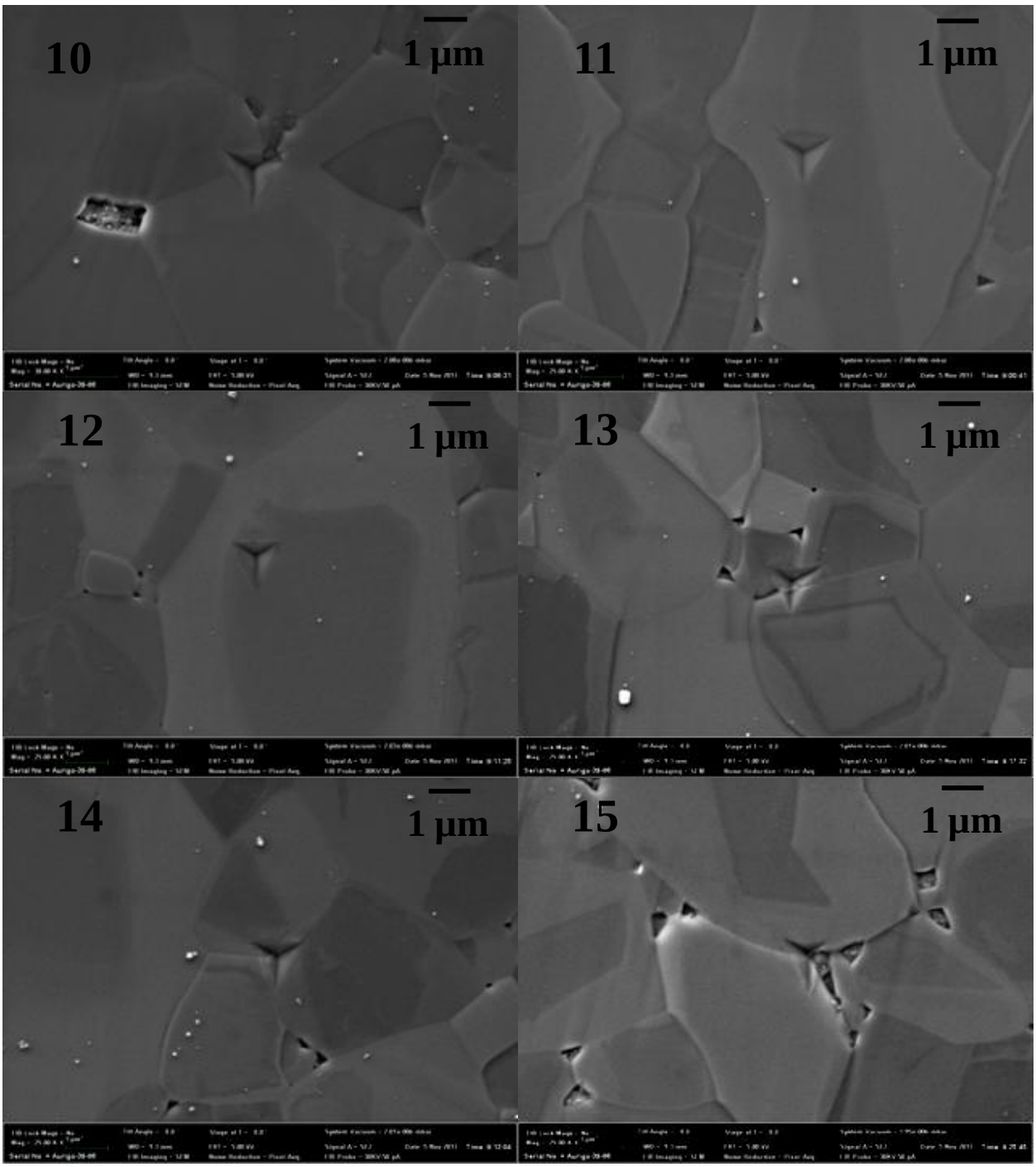

Figure 54: SEM images of Berkovich indentations at 25mN peak load in SiC-N indents (10-15).

Since the material response for an indent at 25 mN peak load, at the center of the grain is from the main phase SiC, it is expected that the PE/TE ratio is similar to single crystal SiC-6H.

CONCLUSIONS

In this chapter, energy methods are used to analyze the load displacement curves obtained during Berkovich indentation experiments on SiC-6H single crystal and polycrystalline samples. The ratio of the plastic energy to total energy is a measure of the amount of energy dissipated during indentation. It is found that, for a given indent size a smaller grain size material SiC-RN will have more grains push out than a larger grain size material (SiC-N and SiC-HPN), which will affect the material response especially the PE/TE ratios. The important conclusions are,

1. The PE/TE ratios for Cree SiC-6H <01-10> and fused silica stay relatively constant over the entire testing range (25 – 500 mN peak load).
2. The PE/TE ratios for Cree SiC-6H <0001> at different peak loads show a unique trend. The PE/TE ratio increases with an increase in the peak loads (depth of penetration) up to a certain value, and then remains relatively constant. Cracking effects and indentation self similarity have been identified as two possible causes, along with unknown material and orientation effects for the unique trend.
3. The plastic to total energy ratio for polycrystalline SiC materials are dependent on grain size and the grain boundary phase. As the stressed volume increases enough to incorporate multiple grains the ratios become almost constant.
4. Indentation at 25 mN peak load in SiC-N showed that if the indent size is smaller than the grain size and the indent is near or at the center of the grain then the PE/TE ratio is similar to the SiC-6H <0001> single crystal ratio.

CHAPTER 9. Extraction of flow properties

Nanoindentation experiments with pyramidal indenters having different centerline-to-face angles were performed on Cree SiC-6H along the <0001> direction. Figure 55 shows the load displacement curves with different pyramidal indenters at peak loads of 200 mN. As expected, the penetration depth decreases with an increase in the centerline to face angle. A larger portion of reversible elastic recovery is also observed with an increasing centerline to face angle.

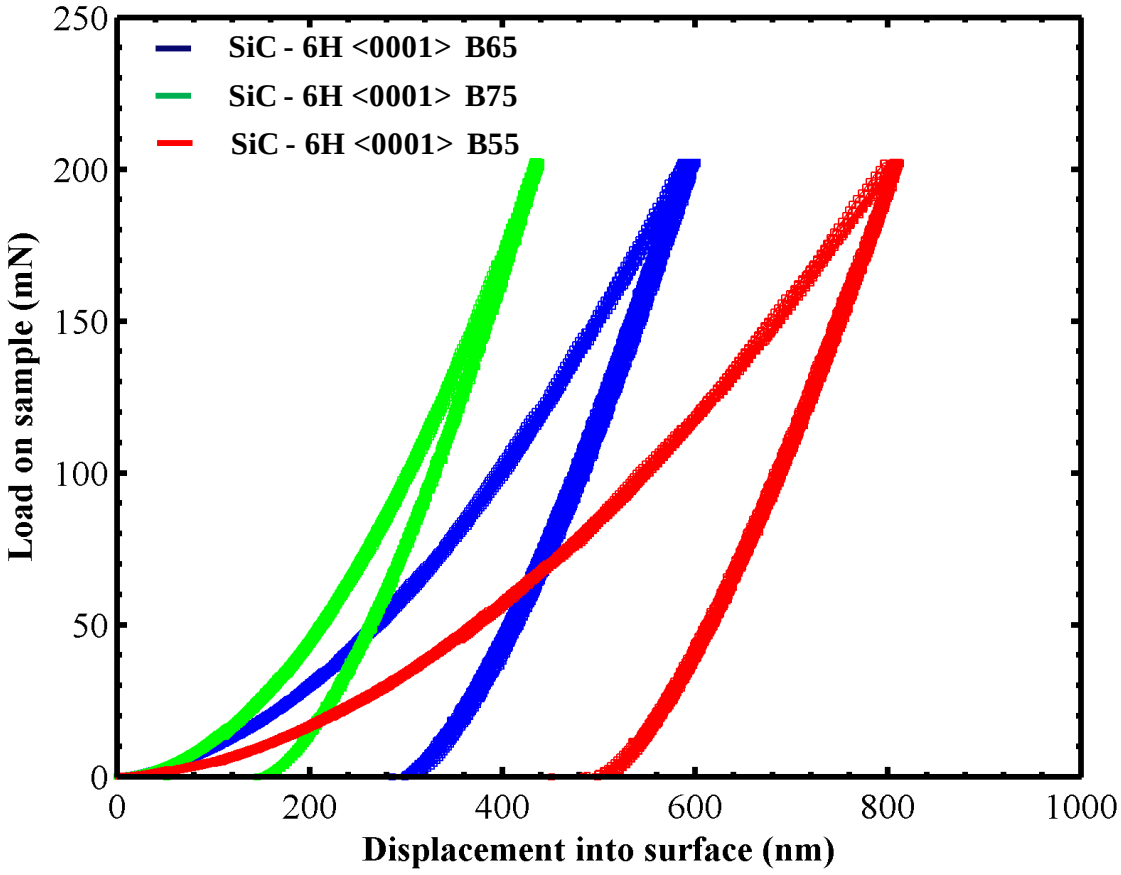

Figure 55: *P-h* curves for indentation of Cree SiC-6H in the <0001> direction with pyramidal indenters of different centerline to face angles.

Since Oliver-Pharr hardness measurements do not account for the pile-up observed during indentation, the values obtained in the nanoindentation experiments are not the best for the FEA analysis. The hardness value obtained by direct measurement of the area using SEM and interference microscope images is used instead in this analysis. Table 12 lists the measured hardness values obtained for the various indenters. Since the FEA analysis requires accurate values of modulus, the values obtained using the elastic contact prediction of 460 GPa for the <0001> direction are used in the analysis. Table 12 summarizes the FEA results for the characteristic strains, constraint factors and flow stresses after 4 iterations for different indenter angles (θ = 45°, 55°, 65°, 75°) and friction coefficients (μ = 0 and 0.2).

Table 12: Characteristic strains, flow stresses and constraint factors obtained for Cree SiC-6H <0001> after the final iteration.

	SiC 6H <0001> E = 460 GPa μ = 0			
Indenter Angle (degrees)	**Constraint factor**	**Characteristic Strain**	**Experimental Hardness (GPa)**	**Flow Stress (GPa)**
45.00	2.31	0.23	51.99	22.47
55.00	2.55	0.13	46.73	18.35
65.30	2.64	0.08	32.26	12.21
75.00	2.48	0.04	27.90	11.25
	SiC 6H <0001> E = 460 GPa μ = 0.2			
45.00	2.97	0.14	51.99	17.51
55.00	2.95	0.09	46.73	15.86
65.30	2.74	0.07	32.26	12.65
75.00	2.44	0.04	27.90	11.43

The hardness values for SiC-6H in the <0001> direction increase with a decrease in the indenter angle. It should be noted that friction plays an important role in calculating the hardness of a

material and in determining the constraint factor and characteristic strains for sharp indenters. According to the literature [64], the normal force exerted by an indenter can increase by up to 20% for a 45° degree indenter with an increase in the friction coefficient from 0 to 0.2. Based on the constraint factors and characteristic strains and the E/Y ratios obtained in the FEA analysis the Holloman fit variables (n and K) are calculated and shown in Table 13.

Table 13: Flow properties of Cree SiC-6H <0001> obtained using FEA.

	SiC 6H <0001> E = 460 GPa ν = 0.18			
Friction coefficient μ	**K**	**n**	**Y (GPa)**	**E/Y**
0	43.939	0.454	6.224	73.904
0.2	37.112	0.379	7.996	57.528

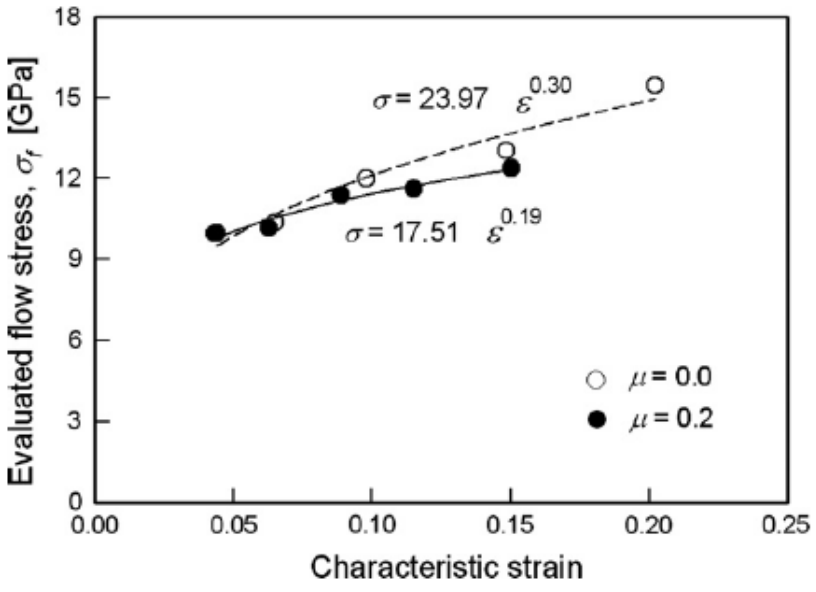

Figure 56: Evaluated flow stress vs characteristic strains obtained by Shim et al. [64].

A similar analysis was performed by Shim et al., and their results are shown in Figure 56. Figure 57 shows the Stress-Strain curves for SiC-6H <0001> extracted using the flow stress and characteristic strain values obtained from a combination of experimental indentation hardness values and FEA simulations using equivalent cones.

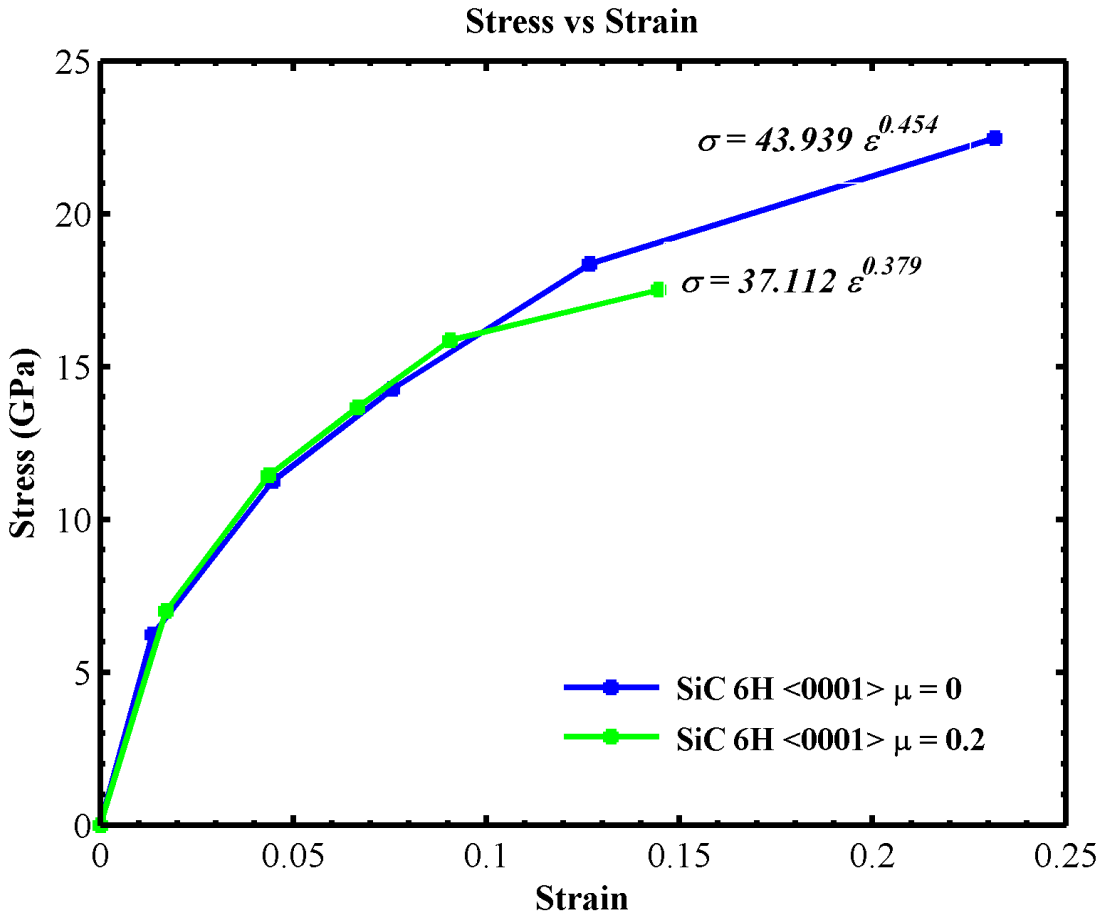

Figure 57: Stress-Strain curves for SiC-6H<0001> using FEA analysis.

The results from the FEA analysis shown in Figure 57, show similar trends to the results obtained by Shim et al. shown in Figure 56. The values of the Holloman fit exponents' n and K and the yield strength are different due to the difference in the values of the modulus and

hardness used by Shim. The SiC-6H<0001> modulus values used in this analysis are 460 GPa compared to those used by Shim et al. which were about 300 GPa. The yield strength is estimated to be 6.2 – 8 GPa which agrees with previous literature [10, 64].

CONCLUSIONS

In this chapter, we have used finite element analysis along with experimental measurements to obtain the stress-strain curves for SiC-6H in the <0001> direction. A sharper indenter produces more strain than a blunt indenter when indented at the same peak load. The measured hardness values for SiC-6H in the <0001> direction increase with a decrease in the center-line to face angle. Finite element analysis using equivalent cones is used to obtain the characteristic strains, flow stresses and constraint factors for two different friction coefficients. The Holloman fit constant and the yield strength is estimated from the finite element analysis results. The results from this chapter can be concluded as,

1. These results show that the indentation hardness values can be used for estimation of yield strength and work hardening exponents for a brittle material like SiC-6H.
2. The flow properties for SiC can be determined provided accurate information about friction coefficients is available. Verification of the stress strain curve is not possible due to the non-availability of room temperature uniaxial stress strain curves.

CHAPTER 10. Summary Conclusions

Nanoindentation experiments using spherical and pyramidal indenters have been carried out on single crystal and polycrystalline SiC to understand the material response to blunt and sharp indenters. Nanoindentation experiments were primarily carried out to study the elastic and plastic anisotropy in SiC-6H single crystals and to experimentally evaluate the fracture and plastic flow of single and polycrystalline SiC for blunt and sharp contacts. The results and the conclusions of the nanoindentation experiments, theoretical elastic plastic contact analysis and finite element simulations were divided into five chapters which build on one another.

Nanoindentation experiments on single crystal SiC-6H samples were used in Chapter 5 to study the elastic and plastic anisotropy in SiC-6H single crystals. Laue diffraction was used to obtain samples with different zenith angles. Berkovich and spherical indenters with different diameters were used in different crystallographic orientations to obtain hardness, modulus and theoretical shear strength estimations. Theoretical analysis using elastic constants and assuming a circular contact were carried out to predict the elastic anisotropy in SiC-6H single crystals. It is found from the experiments that the elastic and plastic anisotropy in single crystal SiC-6H is relatively small. The elastic modulus obtained using Berkovich indenters in different orientations shows good agreement with values obtained using theoretical analysis. It is also found that dopants and other impurities in SiC-6H can vary the hardness and the modulus by up to 10%. It is also found that the cracking pattern in SiC-6H using a Berkovich indenter in the <0001> direction is different than in the <01-10> direction.

Nanoindentation experiments were used in Chapter 6 to study indentation cracking in SiC-6H single crystals in the <0001> direction. Indenter orientation effects in SiC-6H the

<0001> direction were studied using a Berkovich indenter. It is found that there is no indenter orientation dependence when indenting in the <0001> direction, indicating that SiC-6H is a transversely isotropic material. The modulus variation depends only on the angle between the indentation axis and the c-axis. The influence of centerline to face angle on cracking in SiC-6H in the <0001> direction is also studied. It is found as expected that the sharper indenters produce more strains in the material and longer cracks for a given peak load. The surface cracking patterns are similar for all three pyramidal indenters (55°, 65° and 75°) used in this research. This does not take into account any subsurface cracking that might occur due to different pyramidal indenters. Fracture toughness measurements were carried out, and the Lawn and Laugier models were evaluated for different pyramidal indenters. It is found that within the range of our testing loads, the Lawn model for fracture toughness measurement works better for estimating the fracture toughness of SiC-6H in the <0001> direction. It is also found that for a Berkovich indenter the Lawn model which is for medial radial cracking modes gives approximately constant values at low loads (<1N). It is also found that for a Berkovich indentation experiments in SiC-6H in the <0001> direction, at higher loads (>1N), the Laugier model gives constant fracture toughness values. It is conceivable that there is a change in the cracking modes in this range of loads.

Nanoindentation experiments using Berkovich and spherical indenters were used in Chapter 7 to analyze the material response of polycrystalline SiC samples. Berkovich indentation experiments on SiC-RN at various peak loads showed that the material response especially hardness and modulus is relatively insensitive to the amount of indentation damage (cracking, grain push out etc,) when the indent size is larger than the average grain size. It is found that at low peak loads when the indent size is smaller or equal to the average grain size the variance in

the hardness and modulus values is primarily due to the location of the indent and the material anisotropy. From Berkovich indentation experiments, it is found that at low peak loads up to 100 mN the difference in the load displacement curves between the three polycrystalline SiC samples is primarily due to the difference in grain size. At higher peak loads, (500 mN) during Berkovich indentation experiments the material response for all three SiC polycrystalline materials is almost the same. Based on previous literature, spherical indentation with two different diameter indenters was performed on the three polycrystalline SiC samples to check for difference in the material response. It is found that during spherical indentation, within the testing limits of our equipment, there is no difference in the material response between the three polycrystalline SiC ceramics. It is found that at maximum testing loads of 500 mN, the response is elastic-plastic for the 15 μm and completely elastic for the 50 μm diameter sphere for all polycrystalline SiC samples.

Energy analysis of load displacement curves, obtained during Berkovich indentation experiments of single and polycrystalline SiC, was done in Chapter 8. The area under the irreversible part of the load displacement curve, which is a direct measure of the energy dissipated during contact, is used to obtain a relationship between the ratio of plastic to total energy and the microstructure of the material. For an isotopic homogeneous material the plastic to total energy ratio should remain constant. It is found that SiC-6H, when indented in the <0001> direction shows a unique trend, the PE/TE values increase from ~ 0.42 at low loads (< 50 mN) and low indentation depths (< 300 nm) to ~ 0.45 at higher penetration depths (approx. 800 nm penetration depths) and higher loads (> 300 mN peak loads), and then the ratio remain relatively constant. It is found that fused silica and SiC-6H, when indented in the <01-10> direction within the same testing limits as SiC-6H <0001>, show relatively constant PE/TE

values throughout the testing range of loads. It is also found that tip shape effects, and pop-in's at low loads are not responsible for the unique trend in PE/TE values for Berkovich indentation in SiC-6H in the <0001> direction. Cracking and self-similarity of indentation are two factors identified in this chapter, along with other possible unknown orientation and material effects for the unique trend of SiC-6H <0001> PE/TE ratios. It is found that for polycrystalline materials, the PE/TE ratio increases with an increase in the peak load (depth of penetration) before becoming relatively constant. The PE/TE ratios for polycrystalline material remain relatively constant after a load at which the indent size is large enough that the stressed volume of material beneath the indenter incorporates more than one grain. The increase in the PE/TE ratio for polycrystalline ceramics from low to high loads follows a similar trend to SiC-6H when indented in the <0001> direction but the change is much bigger. PE/TE ratios for SiC-N go from ~.0.39 @ 100 mN indentation load to ~ 0.46 @ 500 mN indentation load. This indicates that the change in the ratios is due to the grain size and possibly grain boundary effects. It can be concluded that a material with smaller grain size will have greater energy dissipation at lower peak loads i.e for smaller contact.

Finite element analysis using equivalent cones was used along with measured hardness values to estimate the yield strength, the work hardening exponents and the stress strain curve for single crystal SiC-6H in the <0001> direction. It is found, as expected that the measured hardness values increase with a decrease in the centerline to face angle, i.e the sharper the indenter the higher the hardness. The characteristic strain and the flow stress increase with a decrease in the indenter angle. It is found that it is possible to estimate the stress strain curve, the yield strength of a material and the Holloman fit constants for a brittle material like SiC-6H. The results obtained in this study show good agreement with previous researchers.

REFERENCES

1. Fisher, G.R. and P. Barnes, *Towards a unified view of polytypism in silicon carbide.* Philosophical Magazine Part B, 1990. **61**(2): p. 217-236.
2. Bechstedt, F., et al., *Polytypism and Properties of Silicon Carbide.* physica status solidi (b), 1997. **202**(1): p. 35-62.
3. Willander, M., et al., *High-Temperature Electronic Materials: Silicon Carbide and Diamond*, in *Springer Handbook of Electronic and Photonic Materials*, S. Kasap and P. Capper, Editors. 2007, Springer US. p. 537-563.
4. Shaffer, P., *A review of the structure of silicon carbide.* Acta Crystallographica Section B, 1969. **25**(3): p. 477-488.
5. Li, Z. and R.C. Bradt, *The single crystal elastic constants of hexagonal SiC to 1000°C.* International Journal of High Technology Ceramics, 1988. **4**(1): p. 1-10.
6. Lieberman, D.S. and S. Zirinsky, *A simplified calculation for the elastic constants of arbitrarily oriented single crystals.* Acta Crystallographica, 1956. **9**(5): p. 431-436.
7. Lambrecht, W.R.L., et al., *Calculated elastic constants and deformation potentials of cubic SiC.* Physical Review B, 1991. **44**(8): p. 3685-3694.
8. Arlt, G. and G.R. Schodder, *Some Elastic Constants of Silicon Carbide.* The Journal of the Acoustical Society of America, 1965. **37**(2): p. 384-386.
9. Kamitani, K., et al., *The elastic constants of silicon carbide: A Brillouin-scattering study of 4H and 6H SiC single crystals.* Journal of Applied Physics, 1997. **82**(6): p. 3152-3154.
10. Page, T.F., W.C. Oliver, and C.J. McHargue, *The deformation behavior of ceramic crystals subjected to very low load (nano)indentations.* Journal of Materials Research, 1992. **7**(02): p. 450-473.

11. *Silicon carbide (SiC), lattice parameters, thermal expansion*, in *Group IV Elements, IV-IV and III-V Compounds. Part b - Electronic, Transport, Optical and Other Properties*, O. Madelung, U. Rössler, and M. Schulz, Editors. 2002, Springer Berlin Heidelberg. p. 1-11.

12. Pierson, H.O., *Handbook of Refractory Carbides & Nitrides.* Noyse Publication, 1996.

13. Snead, L.L., et al., *Handbook of SiC properties for fuel performance modeling.* Journal of Nuclear Materials, 2007. **371**(1–3): p. 329-377.

14. Powell, A.R. and L.B. Rowland, *SiC materials-progress, status, and potential roadblocks.* Proceedings of the IEEE, 2002. **90**(6): p. 942-955.

15. Korsunsky, A.M., et al., *On the hardness of coated systems.* Surface and Coatings Technology, 1998. **99**(1–2): p. 171-183.

16. Herbert, E.G., et al., *Mechanical characterization of LiPON films using nanoindentation.* Thin Solid Films, 2011. **520**(1): p. 413-418.

17. Borrero-López, O., et al., *A simple nanoindentation-based methodology to assess the strength of brittle thin films.* Acta Materialia, 2008. **56**(7): p. 1633-1641.

18. Hainsworth, S.V., M.R. McGurk, and T.F. Page, *The effect of coating cracking on the indentation response of thin hard-coated systems.* Surface and Coatings Technology, 1998. **102**(1–2): p. 97-107.

19. Nair, A.K., et al., *Nanoindentation of thin films: Simulations and experiments.* Journal of Materials Research, 2009. **24**(03): p. 1135-1141.

20. Nix, W.D. and H. Gao,f *Indentation size effects in crystalline materials: A law for strain gradient plasticity.* Journal of the Mechanics and Physics of Solids, 1998. **46**(3): p. 411-425.

21. Ma, Q. and D.R. Clarke, *Size dependent hardness of silver single crystals.* Journal of Materials Research, 1995. **10**(04): p. 853-863.

22. Beake, B.D., S.R. Goodes, and J.F. Smith, *Nanoscale materials testing under industrially relevant conditions: high-temperature nanoindentation testing.* Zeitschrift für Metallkunde, 2003. **94**(7): p. 798-801.

23. Constantinides, G., et al., *Quantifying deformation and energy dissipation of polymeric surfaces under localized impact.* Materials Science and Engineering: A, 2008. **489**(1–2): p. 403-412.

24. Wright, W.J. and W.D. Nix, *Storage and loss stiffnesses and moduli as determined by dynamic nanoindentation.* Journal of Materials Research, 2009. **24**(03): p. 863-871.

25. Lucas, B.N. and W.C. Oliver, *Indentation power-law creep of high-purity indium.* Metallurgical and Materials Transactions A, 1999. **30**(3): p. 601-610.

26. Su, C., et al., *Measurement of power-law creep parameters by instrumented indentation methods.* Journal of the Mechanics and Physics of Solids, 2013. **61**(2): p. 517-536.

27. Mann, A.B. and J.B. Pethica, *Nanoindentation Studies in a Liquid Environment†.* Langmuir, 1996. **12**(19): p. 4583-4586.

28. Tabor, D., *The Hardness of Metals*1951, Cambridge, Great Britain.: Oxford University Press.

29. Hertz, *Miscellaneous Papers.* Jones and Schott. Macmillan, London, 1863.

30. Boussinesq, J., *Applications des Potentials a l'Etude de l'Equilibre et du Mouvement des Solides Elastiques.* . Gauthier-Villars, 1885.

31. Sneddon, I.N., *Boussinesq's problem for a rigid cone.* Mathematical Proceedings of the Cambridge Philosophical Society, 1948. **44**(04): p. 492-507.

32. Sneddon, I.N., *The relation between load and penetration in the axisymmetric boussinesq problem for a punch of arbitrary profile.* International Journal of Engineering Science, 1965. **3**(1): p. 47-57.

33. Fischer-Cripps, A.C., *Nanoindentation*. 3rd ed. Mechanical Engineering Series2011: Springer. 288.

34. Bhushan, B. and X. Li, *Nanomechanical characterisation of solid surfaces and thin films.* International Materials Reviews, 2003. **48**(3): p. 125-164.

35. Pethicai, J.B., R. Hutchings, and W.C. Oliver, *Hardness measurement at penetration depths as small as 20 nm.* Philosophical Magazine A, 1983. **48**(4): p. 593-606.

36. Loubet, J.L., et al., *Vickers Indentation Curves of Magnesium Oxide (MgO).* Journal of Tribology, 1984. **106**(1): p. 43-48.

37. Oliver, W.C. and G.M. Pharr, *An improved technique for determining hardness and elastic modulus using load and displacement sensing indentation experiments.* Journal of Materials Research, 1992. **7**(06): p. 1564-1583.

38. Pharr, G.M., W.C. Oliver, and F.R. Brotzen, *On the generality of the relationship among contact stiffness, contact area, and elastic modulus during indentation.* Journal of Materials Research, 1992. **7**(03): p. 613-617.

39. Oliver, W.C. and G.M. Pharr, *Measurement of hardness and elastic modulus by instrumented indentation: Advances in understanding and refinements to methodology.* Journal of Materials Research, 2004. **19**(01): p. 3-20.

40. Bolshakov, A. and G.M. Pharr, *Influences of pileup on the measurement of mechanical properties by load and depth sensing indentation techniques.* Journal of Materials Research, 1998. **13**(04): p. 1049-1058.

41. Field, J.S. and M.V. Swain, *A simple predictive model for spherical indentation.* Journal of Materials Research, 1993. **8**(02): p. 297-306

42. Herbert, E.G., et al., *On the measurement of stress–strain curves by spherical indentation.* Thin Solid Films, 2001. **398–399**(0): p. 331-335.

43. Hutchings, I.M., *The contributions of David Tabor to the science of indentation hardness.* Journal of Materials Research, 2009. **24**(03): p. 581-589.

44. Gane, N. and F.P. Bowden, *Microdeformation of Solids.* Journal of Applied Physics, 1968. **39**(3): p. 1432-1435.

45. Morris, D.J., S.B. Myers, and R.F. Cook, *Sharp probes of varying acuity: Instrumented indentation and fracture behavior.* Journal of Materials Research, 2004. **19**(01): p. 165-175.

46. Bradby, J.E., J.S. Williams, and M.V. Swain, *Pop-in events induced by spherical indentation in compound semiconductors.* Journal of Materials Research, 2004. **19**(01): p. 380-386.

47. Hearth, J.P. and J. Lothe, *Theory of Dislocations*1982: Wiley, New York.

48. Lawn, B.R., *Indentation of Ceramics with Spheres: A Century after Hertz.* Journal of the American Ceramic Society, 1998. **81**(8): p. 1977-1994.

49. Gouldstone, A., K.J. Van Vliet, and S. Suresh, *Nanoindentation: Simulation of defect nucleation in a crystal.* Nature, 2001. **411**(6838): p. 656-656.

50. Berkovich, E.S., *Three-faceted diamond pyramid for micro-hardness testing* Ind. Diamond Rev. , 1951. **11** (127): p. 129–133.

51. Cheng, Y.-T. and C.-M. Cheng, *Relationships between hardness, elastic modulus, and the work of indentation.* Applied Physics Letters, 1998. **73**(5): p. 614-616.

52. Cheng, Y.-T. and C.-M. Cheng, *Scaling, dimensional analysis, and indentation measurements.* Materials Science and Engineering: R: Reports, 2004. **44**(4–5): p. 91-149.

53. Ma, D., et al., *Determination of Young's modulus by nanoindentation.* Science in China Series E: Technological Sciences, 2004. **47**(4): p. 398-408.

54. Malzbender, J., *Energy dissipated during spherical indentation.* Journal of Materials Research, 2004. **19**(06): p. 1605-1607.

55. Malzbender, J. and G. de With, *Elastic modulus, hardness and fracture toughness of SiO2-filled methyltrimethoxysilane coatings on glass substrates.* Journal of Non-Crystalline Solids, 2000. **265**(1–2): p. 51-60.

56. Malzbender, J., G. de With, and J.M.J. den Toonder, *Elastic modulus, indentation pressure and fracture toughness of hybrid coatings on glass.* Thin Solid Films, 2000. **366**(1–2): p. 139-149.

57. Chen, J. and S.J. Bull, *Relation between the ratio of elastic work to the total work of indentation and the ratio of hardness to Young's modulus for a perfect conical tip.* Journal of Materials Research, 2009. **24**(03): p. 590-598.

58. Jang, J.-i. and G.M. Pharr, *Influence of indenter angle on cracking in Si and Ge during nanoindentation.* Acta Materialia, 2008. **56**(16): p. 4458-4469.

59. Lawn, B.R., A.G. Evans, and D.B. Marshall, *Elastic/Plastic Indentation Damage in Ceramics: The Median/Radial Crack System.* Journal of the American Ceramic Society, 1980. **63**(9-10): p. 574-581.

60. Anstis, G.R., et al., *A Critical Evaluation of Indentation Techniques for Measuring Fracture Toughness: I, Direct Crack Measurements.* Journal of the American Ceramic Society, 1981. **64**(9): p. 533-538.

61. Laugier, M.T., *Palmqvist indentation toughness in WC-Co composites.* Journal of Materials Science Letters, 1987. **6**(8): p. 897-900.

62. Gong, J., J. Wang, and Z. Guan, *Indentation toughness of ceramics: A modified approach.* Journal of Materials Science, 2002. **37**(4): p. 865-869.

63. Dukino, R.D. and M.V. Swain, *Comparative Measurement of Indentation Fracture Toughness with Berkovich and Vickers Indenters.* Journal of the American Ceramic Society, 1992. **75**(12): p. 3299-3304.

64. Shim, S., J.-i. Jang, and G.M. Pharr, *Extraction of flow properties of single-crystal silicon carbide by nanoindentation and finite-element simulation.* Acta Materialia, 2008. **56**(15): p. 3824-3832.

65. Chudoba, T. and F. Richter, *Investigation of creep behaviour under load during indentation experiments and its influence on hardness and modulus results.* Surface and Coatings Technology, 2001. **148**(2–3): p. 191-198.

66. Sharpe, W.N., et al., *Fracture Strength of Single-Crystal Silicon Carbide Microspecimens at 24C and 1000 C.* Microelectromechanical Systems, Journal of, 2008. **17**(1): p. 244-254.

67. Sharpe, W.N., Jr., et al., *Fracture strength of silicon carbide microspecimens.* Microelectromechanical Systems, Journal of, 2005. **14**(5): p. 903-913.

68. Nakao, S., et al. *Mechanical characterization of SiC film at high temperatures by tensile test*. in *Micro Electro Mechanical Systems, 2008. MEMS 2008. IEEE 21st International Conference on*. 2008.

69. Henshall, J.L., D.J. Rowcliffe, and J.W. Edington, *Fracture Toughness of Single-Crystal Silicon Carbide.* Journal of the American Ceramic Society, 1977. **60**(7-8): p. 373-375.

70. Liang, K.M., G. Orange, and G. Fantozzi, *Evaluation by indentation of fracture toughness of ceramic materials.* Journal of Materials Science, 1990. **25**(1): p. 207-214.

71. Shaffer, P.T.B., *Effect of Crystal Orientation on Hardness of Silicon Carbide.* Journal of the American Ceramic Society, 1964. **47**(9): p. 466-466.

72. Niihara, K., *Slip systems and plastic deformation of silicon carbide single crystals at high temperatures.* Journal of the Less Common Metals, 1979. **65**(1): p. 155-166.

73. Sawyer, G.R., P.M. Sargent, and T.F. Page, *Microhardness anisotropy of silicon carbide.* Journal of Materials Science, 1980. **15**(4): p. 1001-1013.

74. Umeno, Y., Y. Kinoshita, and T. Kitamura, *Ab initio DFT study of ideal shear strength of polytypes of silicon carbide.* Strength of Materials, 2008. **40**(1): p. 2-6.

75. Miyoshi, K. and D.H. Buckley, *Friction and Deformation Behavior of Single-Crystal Silicon Carbide.* NASA TP, 1977: p. - 1053.

76. Qian, J., L.L. Daemen, and Y. Zhao, *Hardness and fracture toughness of moissanite.* Diamond and Related Materials, 2005. **14**(10): p. 1669-1672.

77. Page, T.F., L. Riester, and S.V. Hainsworth, *The Plasticity Response Of 6H-Sic and Related Isostructural Materials to Nanoindentation: Slip vs Densification.* MRS Online Proceedings Library, 1998. **522**: p. null-null.

78. Kitahara, H., et al., *Mechanical behavior of single crystalline and polycrystalline silicon carbides evaluated by Vickers indentation*. Vol. 109. 2001, Tokyo, Japan: Nippon seramikkusu kyokai.

79. Yan, J., X. Gai, and H. Harada, *Subsurface damage of single crystalline silicon carbide in nanoindentation tests.* J Nanosci Nanotechnol, 2010. **10**(11): p. 7808-11.

80. Guicciardi, S., T. Shimozono, and G. Pezzotti, *Nanoindentation Characterization of Sub-Micrometric Y-TZP Ceramics.* Advanced Engineering Materials, 2006. **8**(10): p. 994-997.

81. Guicciardi, S., et al., *Nanoindentation characterization of SiC-based ceramics.* Journal of the European Ceramic Society, 2007. **27**(2–3): p. 1399-1404.

82. Wereszczak, A.A. and K.E. Johnanns, *Spherical Indentation of SiC* Private Communications.

83. Gao, Y.F. and G.M. Pharr, *Multidimensional contact moduli of elastically anisotropic solids.* Scripta Materialia, 2007. **57**(1): p. 13-16.

84. Li, T.L., et al., *Indentation Schmid factor and orientation dependence of nanoindentation pop-in behavior of NiAl single crystals.* Journal of the Mechanics and Physics of Solids, 2011. **59**(6): p. 1147-1162.

85. Snyder, P.J., et al. *Extracting the Stress-Strain Behavior of Al 6061-T6 and C260 Brass through Indentation and Finite Element Analyses*. Poster presented at the *Gordon Research Conference*. 2012.

86. Minor, A.M., et al., *Direct observations of incipient plasticity during nanoindentation of Al.* Journal of Materials Research, 2004. **19**(01): p. 176-182.

87. Shim, S., et al., *A different type of indentation size effect.* Scripta Materialia, 2008. **59**(10): p. 1095-1098.

APPENDIX

APPENDIX I

Pile-up corrections for a Berkovich indent on a SiC-6H <0001> sample using nanovision.

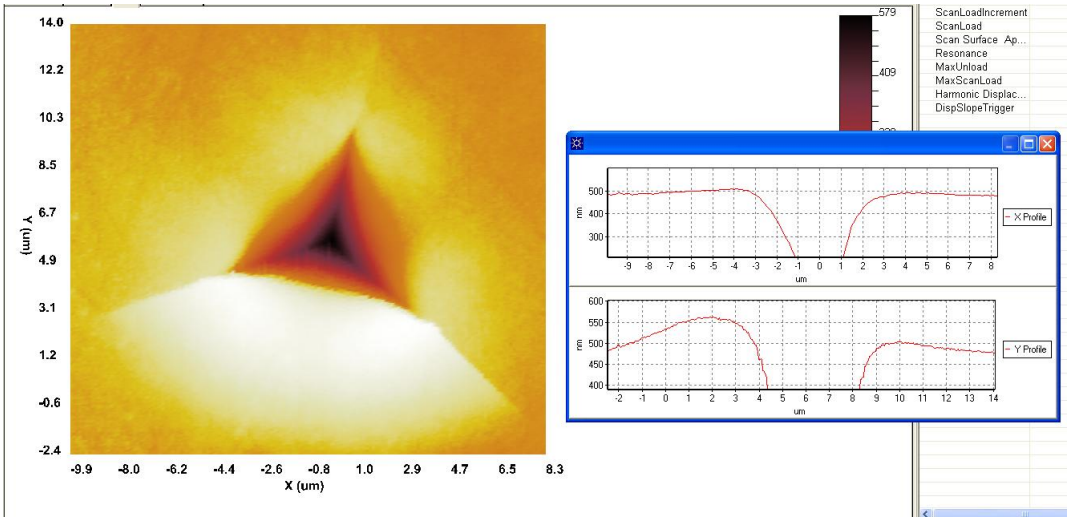

Figure 58: Calculation of pile-up in SiC-6H <0001> using Nanovision.

APPENDIX II

Area function calibration of pyramidal indenters with varying centerline to face angles using fused silica standard sample.

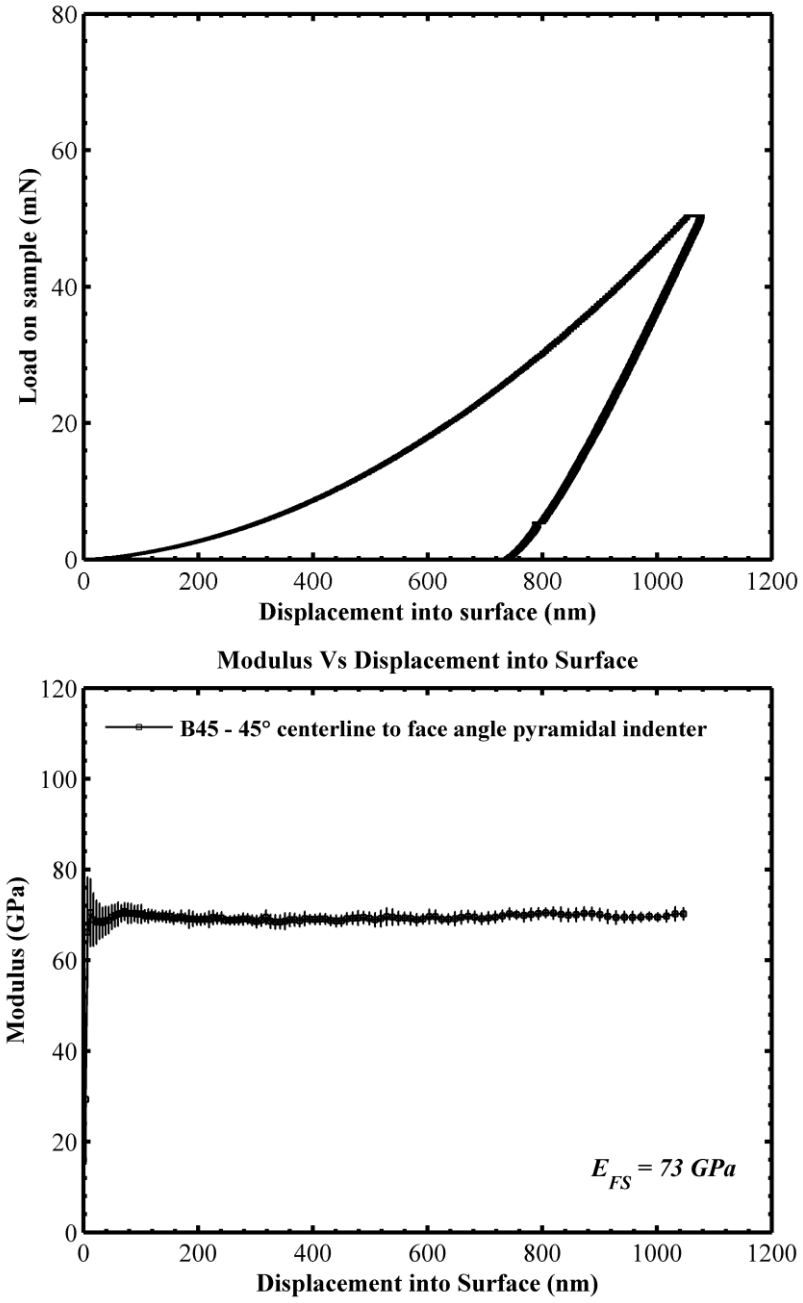

Figure 59: Fused silica *P-h* and *E-h* curves for 45° centerline to face angle tip.

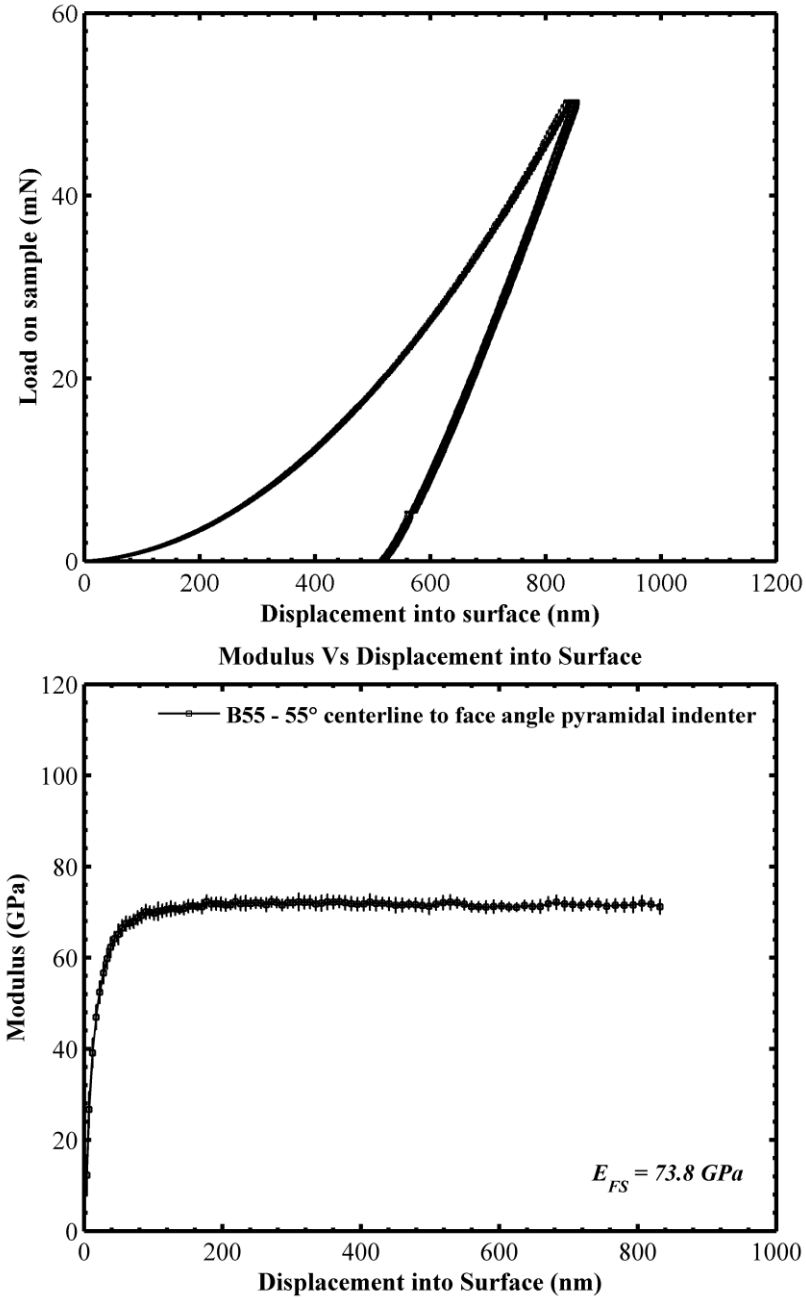

Figure 60: Fused silica *P-h* and *E-h* curves for 55° centerline to face angle tip.

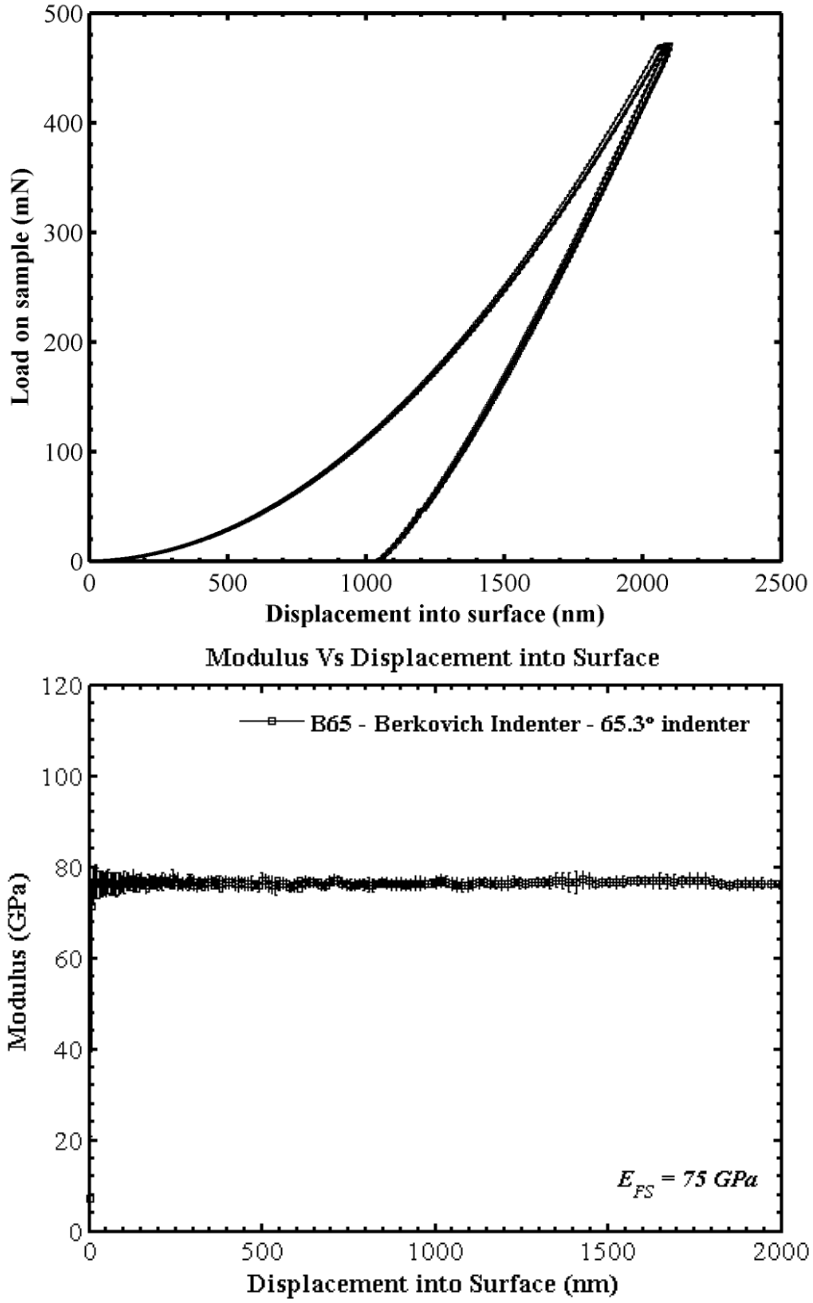

Figure 61: Fused silica *P-h* and *E-h* curves for a Berkovich (65.3°) centerline to face angle tip.

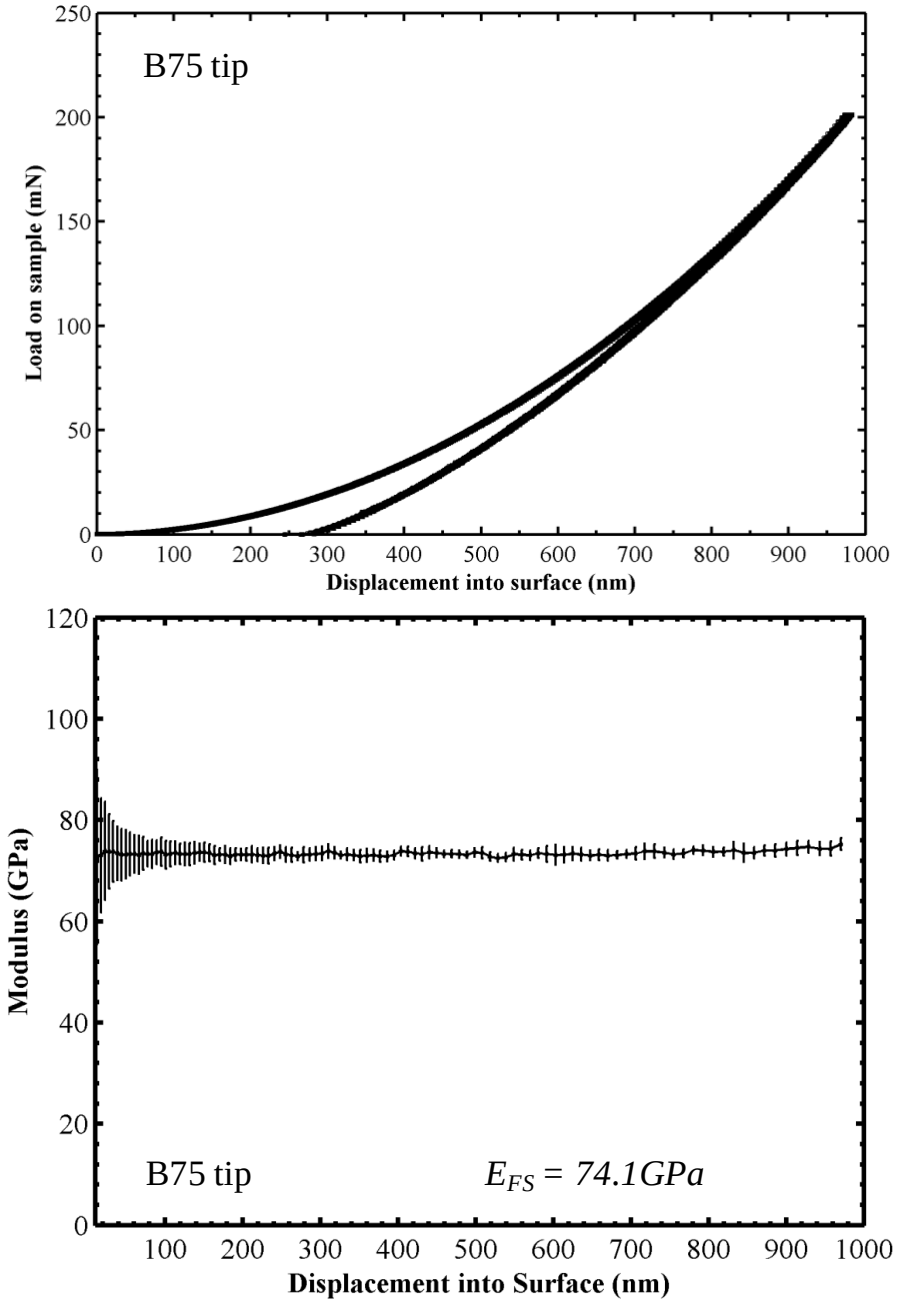

Figure 62: Fused silica *P-h* and *E-h* curves for 75° centerline to face angle tip.

APPENDIX III

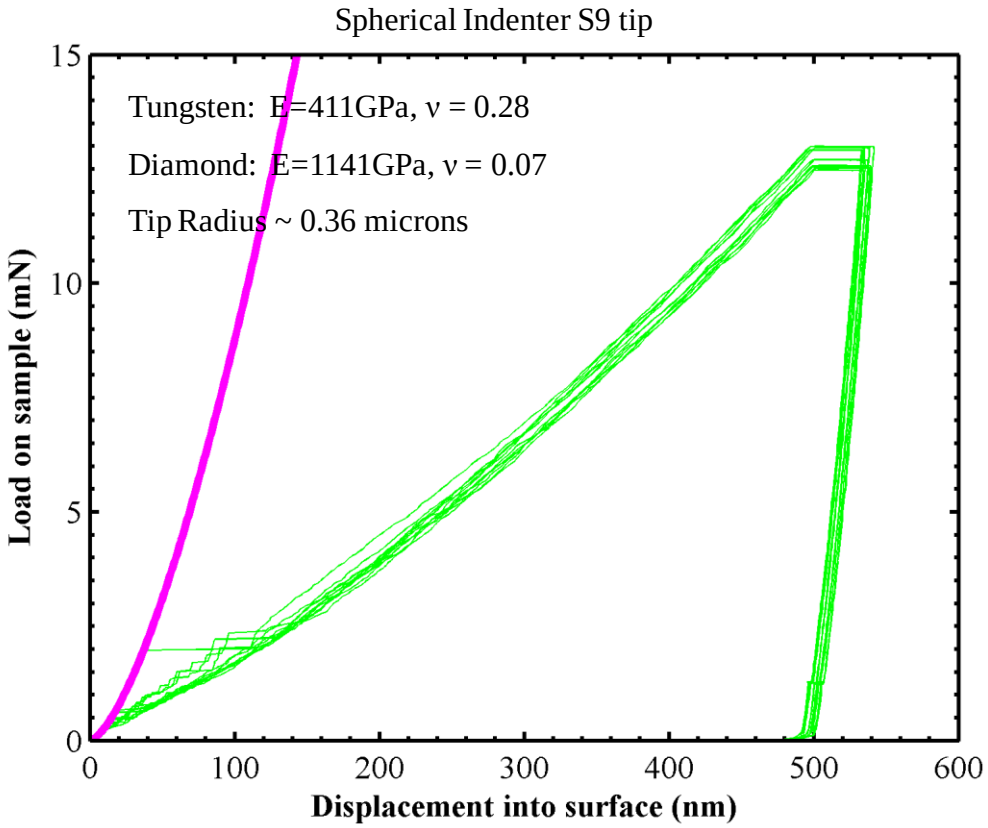

Figure 63: Tungsten calibration for S9 tip.

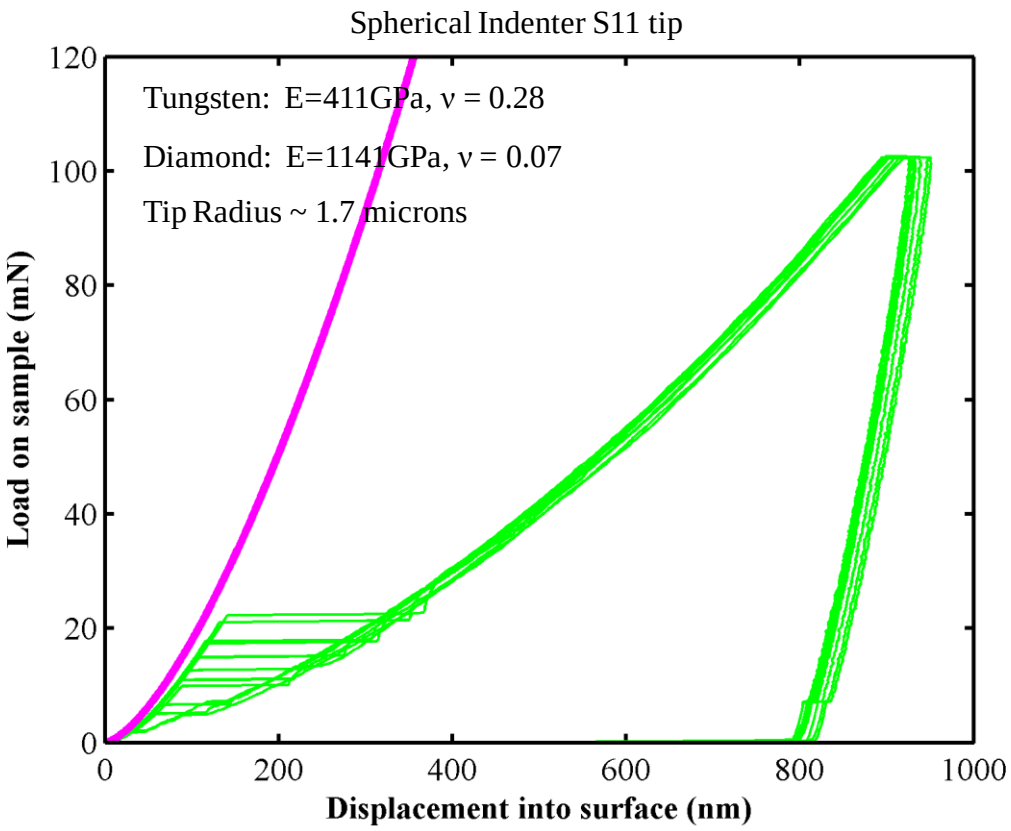

Figure 64: Tungsten calibration for S11 tip.

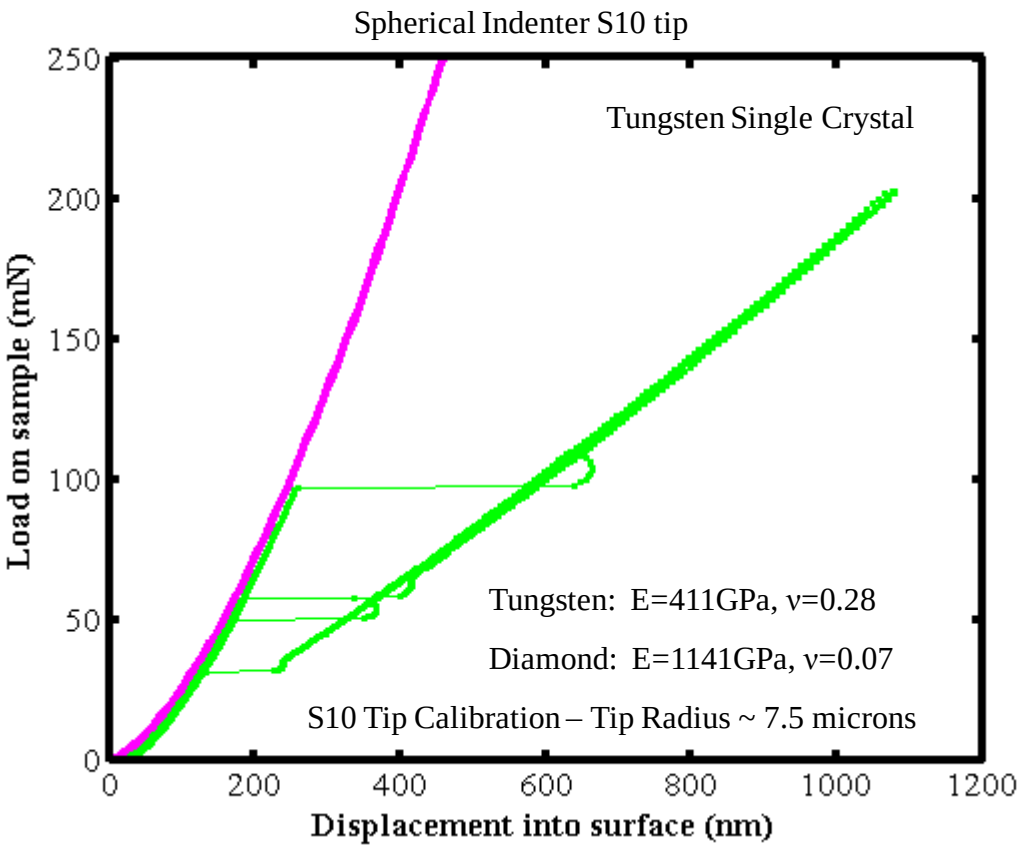

Figure 65: Tungsten calibration for S10 tip.

VITA

Amit Datye was born in Pune, India on March 17, 1979 to Vibhavari and Vijaykumar Datye. Amit, his younger sister Amruta and parents lived in Pune through their entire primary and secondary schooling. Vibhavari and Vijaykumar Datye still live in Pune, India. After attending the University of Pune for his undergraduate degree in Mechanical Engineering, Amit came to the US in 2001 to get his Masters in Mechanical and Materials Engineering at the Florida International University in Miami. Upon completion of the Masters degree in 2003, Amit went to work in the Netherlands for over a year. In 2005, Amit joined Florida International University as a Research Associate in Prof. K. H. Wu's research group. He collaborated with Dr. H.T. Lin at the Oak Ridge National Laboratory and decided to pursue his doctoral education at the University of Tennessee under the guidance of Prof. Pharr. Amit has continuously worked on the mechanical properties of materials for the last 10 years.